

# Coherent control of nuclear and electron spins for quantum information processing

by

Kyungdeock Park

A thesis  
presented to the University of Waterloo  
in fulfillment of the  
thesis requirement for the degree of  
Doctor of Philosophy  
in  
Physics

Waterloo, Ontario, Canada, 2015

© Kyungdeock Park 2015

I hereby declare that I am the sole author of this thesis. This is a true copy of the thesis, including any required final revisions, as accepted by my examiners.

I understand that my thesis may be made electronically available to the public.

K. Park

## Abstract

The ability to perform quantum error correction (QEC) arbitrarily many cycles is a significant challenge for scalable quantum information processing (QIP). Key requirements for multiple-round QEC are a high degree of quantum control, the ability to efficiently characterize both intrinsic and extrinsic noise, and the ability to dynamically and efficiently extract entropy from ancilla qubits. Nuclear Magnetic Resonance (NMR) based quantum devices have demonstrated high control fidelity with up to 12 qubits, and the noise characterizations can be performed using an efficient protocol known as randomized benchmarking. One of the remaining challenges with NMR systems is that qubit initialization is normally only attainable via thermal equilibration. This results in very low polarizations in reasonable experimental conditions. Moving to electron-nuclear coupled spin systems in a single crystal is a promising solution to the ancilla qubit preparation problem. One obvious advantage of incorporating electron spins comes from higher gyromagnetic ratio of the electron which yields about three orders of magnitude larger thermal spin polarization than that of nuclear spins in the same experimental condition. In addition, fast control of nuclear spins is possible provided appropriate level of anisotropic hyperfine interaction strength. The nuclear spins can be polarized even beyond the thermal electron spin temperature using a technique Heat-Bath Algorithmic Cooling (HBAC). With theoretical ideas in hand, the next step is to develop classical instrumentations to control electron-nuclear coupled systems and accomplish high fidelity coherent control. Noise characterizations are also necessary for benchmarking the quality of control over the electron-nuclear spin system.

I first present example applications of NMR QIP with small number of qubits: Testing a foundational question in quantum mechanics and measuring spectral density of noise in a quantum system. Then I report on our home-built X-band electron spin resonance (ESR) spectrometer and progress in achieving high fidelity coherent control of electron and nuclear spins for QIP. We focus on implementing nuclear spin manipulation via anisotropic hyperfine interaction and microwave (mw) control, but discussions also include electron nuclear double resonance (ENDOR) control techniques. We perform realistic algorithmic simulations to show that an experimental cooling of nuclear spins below electron thermal temperature is feasible, and to present the electron-nuclear spin systems as promising testbeds for scalable QIP.

## Acknowledgements

First and foremost, I thank my supervisor Dr. Raymond Laflamme, and it has been an honor to be his student. He is an admirable scientist, leader, and teacher who I highly respect. I am also deeply indebted to my co-supervisor Dr. Jonathan Baugh for his dedicated work, guidance, unending ideas, and showing a life example of an outstanding researcher. I must thank Dr. David Cory for his continuous support in the ESR project, and allowing me to use his facilities and instruments. I am always amazed at and inspired by his wealth of knowledge in magnetic resonance and quantum information. I also thank my advisory committee Dr. Adrian Lupascu for his interest in my research, helpful comments and support, and Dr. Xuedong Hu for agreeing to be the external examiner.

I would like to acknowledge the administrative team at the Institute for Quantum Computing (IQC) and the Department of Physics and Astronomy that made my graduate student life much easier and allowed me to focus on scientific research. I especially thank Wendy Reibel, Carly Turnbull, Matt Cooper, and Judy McDonnell.

I thank Dr. Osama Moussa and Dr. Jingfu Zhang, great mentors, for teaching me NMR QIP, and Dr. Urbasi Sinha for helpful discussions regarding three-paths interference project. I must acknowledge Dr. Troy Borneman for sharing his expertise in ESR quantum computing. His broad and in-depth knowledge in the field has been an invaluable resource for this work. I would like to thank Roberto Romero for his help with building the ESR probe, Ivar Taminiu for his technical support in the laboratory, and Hiruy Haile for help in the student machine shop.

This work would not have been possible without my great colleagues and collaborators. I thank Dr. Robabeh Rahimi Darabad and Dr. Guanru Feng for their hard work, stimulating discussions, sharing their knowledge and ideas to push the project forward, and for friendship. I thank Kyle Willick for his collaboration in the noise spectroscopy project, and being so patient with me as I tried to understand simulation results. I also thank Stéphane Labruyère for his support in the ESR project.

My life at Waterloo is made memorable by friends, and I am truly grateful to have them around in my life. My fantastic roommates at choochoo house, you guys are like my brothers. I also thank my friends at IQC, at the First Korean Presbyterian Church of Waterloo, in the basketball team Maxwells Demons, and friends in Korea.

I would like to thank my parents, my little brother and little sister for their endless love, support, encouragement and prayers.

Lastly, I thank God who has given me everything I have, and who is the shepherd of my life.

Your word is a lamp to guide my feet and a light for my path.  
*-Psalm 119:105*

# Table of Contents

|   |           |
|---|-----------|
| List of Tables  | x         |
| List of Figures   | xi        |
| <b>1 Introduction</b>   | <b>1</b>  |
| <b>2 Backgrounds</b>  | <b>4</b>  |
| 2.1 Introduction to NMR quantum computing . . . . .               | 4         |
| 2.1.1 Liquid state NMR . . . . .                                  | 4         |
| 2.1.2 Solid state NMR . . . . .                                   | 6         |
| 2.1.3 State preparation in ensemble quantum computation . . . . . | 7         |
| 2.2 QEC with mixed ancilla qubits . . . . .                       | 9         |
| <b>3 Example applications of few-qubit NMR QIP</b>                | <b>10</b> |
| 3.1 Introduction . . . . .  | 10        |
| 3.2 Testing Born's rule using liquid state NMR . . . . .          | 11        |
| 3.2.1 Encoding three paths in energy eigenstates . . . . .        | 12        |
| 3.2.2 Experiment . . . . .  | 14        |
| 3.2.3 Analysis of possible sources of error . . . . .             | 17        |
| 3.3 Qubit noise spectroscopy using NMR . . . . .                  | 19        |
| 3.3.1 Generalized Bloch equations . . . . .                       | 24        |

|          |   |           |
|----------|---|-----------|
| 3.3.2    | Overlap integral method . . . . .   | 25        |
| 3.3.3    | Perturbation series . . . . .   | 26        |
| 3.3.4    | Experiment . . . . .  | 29        |
| 3.3.5    | Summary and future work . . . . .   | 36        |
| <b>4</b> | <b>Anisotropically coupled electron-nuclear spins for QIP</b>                 | <b>37</b> |
| 4.1      | Introduction . . . . .  | 37        |
| 4.2      | System model . . . . .  | 38        |
| 4.2.1    | Electron spin resonance: Zeeman interaction . . . . .                         | 38        |
| 4.2.2    | Hyperfine Interaction . . . . .   | 39        |
| 4.2.3    | Spin Hamiltonian for 1 electron coupled to $N$ nuclei . . . . .               | 39        |
| 4.3      | System characterization: Hamiltonian determination . . . . .                  | 41        |
| 4.3.1    | Electron g-tensor and hyperfine interaction tensor characterization . . . . . | 43        |
| 4.3.2    | Hamiltonian determination at a fixed crystal orientation . . . . .            | 45        |
| 4.4      | Closed system control . . . . .   | 48        |
| 4.4.1    | Universal control via anisotropic hyperfine interaction . . . . .             | 49        |
| 4.4.2    | Pulse design . . . . .  | 50        |
| 4.5      | Decoherence model . . . . .   | 52        |
| 4.5.1    | Kraus representation . . . . .  | 52        |
| 4.5.2    | Liouville representation . . . . .  | 53        |
| 4.5.3    | Lindblad equation . . . . .   | 54        |
| 4.5.4    | Relaxations of a spin ensemble . . . . .                                      | 54        |
| 4.5.5    | Electron-nuclear cross relaxation . . . . .                                   | 55        |
| 4.6      | Crystal orientation selection for optimal control . . . . .                   | 56        |
| 4.6.1    | Orientation Criteria for Anisotropic hyperfine control . . . . .              | 56        |
| 4.6.2    | Orientation Criteria for ENDOR control . . . . .                              | 57        |

|          |   |           |
|----------|---|-----------|
| <b>5</b> | <b>Home-built instrumentation for X-band pulsed electron spin resonance</b>                                   | <b>58</b> |
| 5.1      | Introduction . . . . .  | 58        |
| 5.2      | Pulsed ESR spectrometer . . . . .   | 59        |
| 5.3      | Loop-gap resonator . . . . .  | 61        |
| 5.4      | Variable temperature probe . . . . .  | 62        |
| 5.5      | Sample holder . . . . .   | 65        |
| 5.6      | Pulse implementation correction . . . . .   | 65        |
| 5.7      | Future work . . . . .   | 69        |
| <b>6</b> | <b>Randomized benchmarking of quantum gates as a tool for characterizing and improving microwave controll</b> | <b>70</b> |
| 6.1      | Introduction . . . . .  | 70        |
| 6.2      | Single qubit protocol . . . . .   | 72        |
| 6.3      | Experiment . . . . .  | 73        |
| 6.3.1    | Simulations and initial experimental run . . . . .  | 73        |
| 6.3.2    | Hardware configuration optimization for high fidelity control . . . . .                                       | 75        |
| 6.3.3    | Selection sequence to reduce field inhomogeneities . . . . .  | 78        |
| 6.3.4    | Final results and discussions . . . . .   | 80        |
| 6.3.5    | Effect of incoherent error on the fidelity decay . . . . .  | 82        |
| 6.4      | Future work . . . . .   | 85        |
| <b>7</b> | <b>Testing the feasibility of heat bath algorithmic cooling in the electron-nuclear spin system</b>           | <b>86</b> |
| 7.1      | Introduction . . . . .  | 86        |
| 7.2      | Simulating HBAC using five hyperfine spin qubits . . . . .  | 88        |
| 7.2.1    | Sample preparation . . . . .  | 88        |
| 7.2.2    | Five-qubit malonic acid spin Hamiltonian determination . . . . .  | 89        |
| 7.2.3    | Malonic acid orientation selection . . . . .  | 93        |
| 7.2.4    | Simulating 3-qubit HBAC . . . . .   | 97        |
| 7.2.5    | Simulating 5-qubit HBAC . . . . .   | 104       |
| 7.3      | Summary and future work . . . . .   | 107       |



|                           |     |
|---------------------------|-----|
| 8 Conclusions and outlook | 111 |
| References                | 114 |

# List of Tables

|     |  |     |
|-----|--|-----|
| 3.1 | Three paths arrangement table . . . . .  | 13  |
| 6.1 | Gate-dependence of cumulative error due to $T_2^*$ . . . . .                                 | 83  |
| 7.1 | Electronic g-factor and hyperfine tensors of malonic acid from CW ESR measurements . . . . . | 91  |
| 7.2 | Hyperfine tensors for $A^{C_1}$ and $A^{C_2}$ from CW ENDOR measurements . . . . .           | 93  |
| 7.3 | Optimal orientations for AHC experiment with malonyl radical . . . . .                       | 95  |
| 7.4 | Optimal orientations for ENDOR experiment with malonyl radical . . . . .                     | 96  |
| 7.5 | Results of 1 round 5-qubit HBAC . . . . .  | 107 |

# List of Figures

|     |  |    |
|-----|--|----|
| 3.1 | Quantum circuit for the LSNMR three path experiment . . . . .                    | 14 |
| 3.2 | $^{13}\text{C}$ tris(trimethylsilyl)silane-acetylene (TTMSA) . . . . .           | 15 |
|     | (a) Schematic of TTMSA . . . . .   | 15 |
|     | (b) Natural Hamiltonian parameters, $T_1$ and $T_2$ of TTMSA . . . . .           | 15 |
| 3.3 | $^1\text{H}$ spectra in the three path experiment . . . . .                      | 16 |
|     | (a) Thermal state . . . . .  | 16 |
|     | (b) Pseudo-pure state . . . . .  | 16 |
|     | (c) State after $\mathcal{U}_p$ . . . . .  | 16 |
|     | (d) State after $\mathcal{V}^{111}$ . . . . .                                    | 16 |
| 3.4 | Experimental results for $\kappa$ . . . . .                                      | 18 |
| 3.5 | Filter functions . . . . .   | 22 |
|     | (a) Modulation of the system-environment interaction generated by CPMG . . . . . | 22 |
|     | (b) Modulation of the system-environment interaction generated by CW . . . . .   | 22 |
|     | (c) CPMG frequency domain filter function . . . . .                              | 22 |
|     | (d) CW frequency domain filter function . . . . .                                | 22 |
| 3.6 | Input vs extracted noise spectrum . . . . .                                      | 26 |
|     | (a) $S(\omega) = 2\pi \cdot 30/\omega$ . . . . .                                 | 26 |
|     | (b) $S(\omega) = 2\pi \cdot 3000/\omega$ . . . . .                               | 26 |
| 3.7 | Higher order coefficients in the simulated signal decay . . . . .                | 28 |
| 3.8 | Solid state NMR $S(\omega)$ . . . . .  | 31 |

|      |  |    |
|------|--|----|
| (a)  | SSNMR $S(\omega)$ in linear scale . . . . .                | 31 |
| (b)  | SSNMR $S(\omega)$ in log-log scale . . . . .               | 31 |
| 3.9  | CPMG signal decay . . . . .                                | 32 |
| (a)  | CPMG signal decay 0.25 Hz . . . . .                        | 32 |
| (b)  | CPMG signal decay 1.6 kHz . . . . .                        | 32 |
| (c)  | CPMG signal decay 80 Hz . . . . .                          | 32 |
| (d)  | CPMG signal decay 500 Hz . . . . .                         | 32 |
| 3.10 | $T_{1\rho}$ signal decay . . . . .                         | 33 |
| (a)  | $T_{1\rho}$ signal decay 2 Hz . . . . .                    | 33 |
| (b)  | $T_{1\rho}$ signal decay 80 Hz . . . . .                   | 33 |
| 3.11 | Liquid state NMR $S(\omega)$ . . . . .                     | 34 |
| (a)  | LSNMR $S(\omega)$ in linear scale . . . . .                | 34 |
| (b)  | LSNMR $S(\omega)$ in log-log scale . . . . .               | 34 |
| 3.12 | Simulated $T_{1\rho}$ signal decay . . . . .               | 35 |
| 4.1  | 1 electron - 1 nucleus in strong coupling regime . . . . . | 42 |
| (a)  | Energy splittings . . . . .                                | 42 |
| (b)  | Energy level diagram . . . . .                             | 42 |
| (c)  | Schematic ESR spectrum . . . . .                           | 42 |
| 4.2  | Schematic of the crystal mounting . . . . .                | 44 |
| 4.3  | ESEEM pulse sequence . . . . .                             | 46 |
| (a)  | Two-pulse ESEEM . . . . .                                  | 46 |
| (b)  | Three-pulse ESEEM . . . . .                                | 46 |
| 4.4  | Pulsed ENDOR pulse sequence . . . . .                      | 47 |
| 5.1  | Home-built X-band ESR spectrometer design . . . . .        | 59 |
| 5.2  | Schematic of loop-gap resonator . . . . .                  | 61 |
| 5.3  | Home-built low-T probe . . . . .                           | 62 |

|     |   |    |
|-----|---|----|
| 5.4 | Loop-gap resonator measurements . . . . .   | 63 |
|     | (a) LGR S11 measurement . . . . .   | 63 |
|     | (b) Rabi oscillation: irradiated fused quartz . . . . .   | 63 |
| 5.5 | Temperature vs resistance . . . . .   | 64 |
| 5.6 | Schematic of sample holder . . . . .  | 66 |
|     | (a) Sample holder . . . . .   | 66 |
|     | (b) Placement in the LGR . . . . .  | 66 |
| 5.7 | Circuit design for pulse fixing . . . . .   | 67 |
| 5.8 | Example results of pulse implementation correction . . . . .  | 68 |
|     | (a) Measured vs ideal pulse shape before pulse-fixing . . . . .   | 68 |
|     | (b) Measured vs ideal pulse shape after pulse-fixing . . . . .  | 68 |
| 6.1 | Randomized benchmarking pulse sequence . . . . .  | 72 |
| 6.3 | Phase transient error . . . . .   | 76 |
|     | (a) Pulse shape . . . . .   | 76 |
|     | (b) Calibration data . . . . .  | 76 |
| 6.4 | Phase transient correction . . . . .  | 77 |
|     | (a) Pulse shape . . . . .   | 77 |
|     | (b) Calibration data . . . . .  | 77 |
| 6.5 | Effect of TWT blanking delay on the pulse shape . . . . .   | 78 |
|     | (a) 300 ns TWT blanking delay . . . . .   | 78 |
|     | (b) 2 $\mu$ s TWT blanking delay . . . . .  | 78 |
| 6.6 | $T_2^*$ and $B_1$ field distribution of the irradiated quartz measured in the home-built ESR spectrometer . . . . . | 79 |
|     | (a) $T_2^*$ distribution . . . . .  | 79 |
|     | (b) $B_1$ distribution . . . . .  | 79 |
| 6.7 | Summary of randomized benchmarking experimental results . . . . .   | 81 |
| 6.8 | Incoherent error analysis . . . . .   | 83 |

|      |  |     |
|------|--|-----|
| 7.1  | Molecular structure of $\dot{\text{C}}\text{H}(\text{COOH})_2$ . . . . .   | 89  |
| 7.2  | ESR transition frequencies vs crystal orientation of the methylene $^{13}\text{C}$ -labeled malonic acid . . . . . | 92  |
| 7.3  | ESR transition frequencies vs crystal orientation of the per- $^{13}\text{C}$ -labeled malonic acid . . . . .      | 92  |
| 7.4  | ENDOR spectrum of the carboxyl $^{13}\text{C}$ -labeled sample at a fixed orientation                              | 94  |
| 7.5  | ESR spectrum of the carboxyl $^{13}\text{C}$ -labeled sample at a fixed orientation . .                            | 94  |
| 7.6  | Quantum circuit of 3-qubit HBAC using AHC . . . . .  | 98  |
| 7.7  | Simulation results for 3-qubit HBAC using AHC . . . . .  | 99  |
| 7.8  | Quantum circuit of the 3-qubit HBAC using ENDOR . . . . .  | 101 |
| 7.9  | Simulated spectra for $^{13}\text{C}_m$ -labeled malonic acid and microwave cavity transfer function . . . . .     | 102 |
| 7.10 | Simulation results of the 3-qubit HBAC using ENDOR . . . . .   | 103 |
| 7.11 | Quantum circuit for 5-qubit HBAC . . . . .   | 104 |
| 7.12 | Circuit for polarization transfer between the electron and $\text{C}_{1,2}$ . . . . .                              | 105 |
| 7.13 | Theoretical target qubit polarization attainable in 5-qubit HBAC . . . . .   | 106 |
| 7.14 | Estimated target qubit polarization in HBAC vs temperature . . . . .   | 109 |

# Chapter 1

## Introduction

Quantum Information Processing (QIP) has the potential to perform exponentially faster computation and revolutionize current technology by harnessing systems governed by the laws of quantum mechanics. The power of QIP over its classical counterpart has already been demonstrated through several examples such as simulating quantum phenomena [1], factoring of large numbers [2], and increased speed in database searching [3], with more breakthroughs of the quantum revolution yet to come. However, when theoretical ideas are implemented in real physical systems the power of quantum computation can quickly diminish due to both intrinsic and extrinsic error to which the quantum system is exposed. Quantum error correction (QEC) is a theory that aims to protect quantum information against the imperfections of realistic devices, enabling the scaling of quantum processors up to many qubits. Although a well developed theory exists [4–9] and experimental realizations at several qubit level are only recently emerging [10–12], there remain challenges for many potential implementations.

Performing QEC arbitrarily many rounds requires a high degree of quantum control, efficient noise characterization, and the ability to extract entropy from ancilla qubits efficiently. Nuclear Magnetic Resonance (NMR) quantum information processing has demonstrated a high control fidelity [13–15] (see [16, 17] for reviews on recent advances and experiments in NMR QIP) and the ability to efficiently characterize the noise, both intrinsic and extrinsic, that affects the fidelity of a quantum processes [18–20]. These devices are excellent test beds that are available in the lab today for exploring the ideas of quantum control and error correction. A recent solid state NMR experiment has demonstrated sufficient level of control for two rounds of QEC [10]. However, one piece has been missing: the ability to efficiently polarize nuclear spin qubits on demand. The threshold theorem for quantum computation tells us that a quantum circuit can be simulated with a given

precision using a polynomial amount of resources as long as the probability of error per gate  $p$  is below a certain threshold value  $p_{th}$  [5, 6, 21, 22]. The theorem relies on assuming that ancilla qubits are in nearly pure states at the beginning of each cycle of fault-tolerant QEC, and that the state cannot be more mixed than what the accuracy threshold permits. For example, the first layer of concatenation of QEC typically reduces the effective error rate from  $p$  to  $cp^2$ , where  $c$  is a system-dependent constant. However, this theoretical gain is not generally achieved for the impure ancilla qubits characteristic of real implementations [23]. Thus, an efficient and experimentally feasible method for cooling qubits to high purity prior to each QEC cycle is desirable for all circuit implementations, including those based on nuclear spins.

Purifying qubits in NMR can be obtained through Heat Bath Algorithmic Cooling (HBAC) [24–28]. It is an efficient method for extracting entropy from qubits that interact with a heat bath, allowing cooling below the bath temperature (i.e. beyond the closed-system, or Shannon bound). In a nutshell, HBAC recurrently applies two steps: Given  $n$  number of system qubits each with polarization  $\epsilon_0$ , cool  $n - m$  qubits by compressing entropy into  $m$  qubits. The polarization of  $m$  qubits is exchanged with the heat bath polarization  $\epsilon_b$ . By repeating these steps,  $n - m$  qubits can attain a final polarization  $\epsilon_f$  that is greater than  $\epsilon_b$ . There is an asymptotic limit for  $\epsilon_f$  that depends on  $n$  and  $\epsilon_b$ . Solid state NMR experiments have demonstrated a sufficient level of coherent control to iterate few rounds of algorithmic cooling, leading to spin polarizations exceeding the thermal polarization [29, 30]. However, under typical experimental conditions, the nuclear spin polarization at thermal equilibrium is very small and therefore precise control of tens of nuclear spin qubits is required for reaching polarization of order unity on one qubit.

For practical HBAC and QEC, coupled electron-nuclear spin systems are more promising than conventional NMR Quantum Computing (QC). Due to the electron’s much larger gyromagnetic ratio compared to nuclei, the electronic thermal spin polarization is about  $10^3$  times larger, and spin-lattice relaxation rates scale by a similar factor. Exploiting the electronic spin-lattice relaxation as a reset operation, the electron can connect a set of nuclear spins to heat bath with an effective temperature much lower than the initial nuclear spin temperature. Moreover, when the hyperfine interaction between the electron and a nucleus is larger than nuclear Zeeman interaction, fast manipulation of the nuclear spin can be achieved via irradiating only the electron with microwave pulses and using the anisotropic part of the interaction [31–33].

This thesis is focused on addressing two problems. First is to achieve high fidelity quantum control of the electron spin. The progress towards achieving high fidelity coherent control of the electron spin in the solid state using home-built electron spin resonance spectrometer operating at X-band frequency is reported. The ESR spectrometer and a



customized variable temperature probe are built and used for exploring and benchmarking the coherent control of the electron spin. Second is to see whether the experimental cooling of a nuclear spin below electron thermal equilibrium temperature can be realized using HBAC with available electron-nuclear spin systems. We provide detailed studies on the feasibility of HBAC in the physical system by determining the full spin Hamiltonian of a five-qubit hyperfine coupled spin system and performing realistic simulations. The primary aim is to achieve sufficient level of quantum control for cooling of nuclear spins below electron thermal equilibrium temperature, but the instrumentation and control techniques presented in the thesis can be adapted for implementing other quantum algorithms requiring similar size of Hilbert space.

The rest of the thesis is organized as follows. Ch. 2 provides background information relevant to the main theme of the thesis, such as a brief introduction to NMR QIP and QEC with mixed ancilla qubits. The author contributed in writing reviews on the NMR QIP that appeared in [16, 34]. Ch. 3 reports two NMR projects that serve as examples of useful applications of NMR QIP. The first NMR project exploits high degree of control available in the liquid state NMR QIP and tests the validity of the Born rule, one of the fundamental postulates of quantum mechanics. This work is published in [35]. The second project is the on-going study of  $T_{1\rho}$  noise spectroscopy, a useful technique for designing a protocol for reducing system-environment interaction. Ch. 4 explains details of electron-nuclear coupled spin systems and the electron spin resonance spectroscopy that are relevant for QIP. Ch 5 describes the design of an X-band ESR spectrometer, a loop-gap resonator, and a variable temperature probe custom-built for controlling electron-nuclear spin systems. In Ch. 6, the randomized benchmarking is used as a tool to characterize and improve the microwave control of the electron using the home-built instrumentation. The benchmarking is performed on irradiated fused quartz, a single-qubit paramagnetic sample in powder form. Lastly, realistic simulations of heat-bath algorithmic cooling using a five-qubit electron-nuclear hyperfine coupled spin system is presented in Ch. 7. This work is published in [36].

# Chapter 2

## Backgrounds

### 2.1 Introduction to NMR quantum computing

In the presence of a static magnetic field, the ground state of a nuclear spin-1/2 undergoes energy splitting into two spin levels, and quantum information can be encoded in this well-defined two level system. Nuclear spin-1/2 particles in the presence of a strong magnetic field are an excellent candidate for quantum information processors for several reasons: the form of the Hamiltonian of the system is well known, fairly easy to characterize, and the coherence times are reasonably long. Moreover, NMR benefits from years of development by scientists who used the technology to characterize molecules and proteins, or for medical imaging. Fundamentals of NMR QIP can be expanded to other spin and magnetic resonance based implementations, such as the electron-nuclear coupled system which is the main focus of this work. In this section, we briefly introduce the basics of NMR quantum computing. For further information on NMR QIP, there are excellent references [16, 37, 38].

#### 2.1.1 Liquid state NMR

##### The natural spin Hamiltonian

Nuclear magnetic resonance arises from the interaction between the nuclear magnetic dipole moment and an applied magnetic field. The magnetic moment of a nuclear spin whose observable is described by a spin-1/2 operator  $\mathcal{I}$  is given as

$$\boldsymbol{\mu} = g \frac{q}{2m} \mathcal{I} = \gamma \mathcal{I}, \quad (2.1)$$

where  $g$  is the g-factor,  $q$  is the charge, and  $m$  is the mass of the nucleus. In quantum information science convention, Pauli matrices are often used and the spin-1/2 operator  $\mathcal{I}$  can be defined using Pauli matrices as  $\mathcal{I}_i = \sigma_i/2$ , where  $i \in \{x, y, z\}$ . The external magnetic field  $\mathbf{B}_0$  induces currents in the electron clouds, which in turn induces a secondary magnetic field at the nucleus site, shielding the nuclear spin from the external magnetic field. Hence the local magnetic field can be written as the sum of the external field and a shift term  $\delta$  known as the chemical shift:  $\mathbf{B}_n = (1 + \delta)\mathbf{B}_0$ . Then the magnetic energy of the interaction, known as Zeeman interaction of the spin under the magnetic field  $\mathbf{B}_0$  is

$$\mathcal{H}_{nz} = -\boldsymbol{\mu} \cdot (1 + \delta)\mathbf{B}_0. \quad (2.2)$$

We set  $\hbar = 1$  so that all Hamiltonians will appear in angular frequency unit. We define our coordinate system such that the static magnetic field is applied along the z-axis, and the spin is quantized along  $\mathbf{B}_0 = B_0\hat{z}$ . In this frame, the Zeeman Hamiltonian for a nuclear spin can be written as  $\mathcal{H}_{nz} = -\omega_n\mathcal{I}_z$ , where  $\omega_n = (1 + \delta)\gamma B_0$  is the nuclear Larmor frequency.

For  $N$  spin-1/2 nuclei, the relevant internal spin Hamiltonian is given by:

$$\mathcal{H}_0 = \sum_{k=1}^N \mathcal{H}_{nz}^k + 2\pi \sum_{i < j} J_{ij} \mathcal{I}^i \cdot \mathcal{I}^j, \quad (2.3)$$

where  $J_{ij}$  is known as J-coupling that induces magnetic interactions between nuclei mediated by electrons that form chemical bonds. The dipole-dipole interactions in the liquid state average to zero due to fast molecular tumbling. When the difference in chemical shifts between coupled nuclei are much greater than their respective J-coupling strength, the weak coupling approximation can be applied and the coupling term between nuclei  $i$  and  $j$  becomes  $2\pi J_{ij} \mathcal{I}_z^i \mathcal{I}_z^j$ .

## Universal control

A single nuclear spin rotation about a transverse axis, that is perpendicular to the quantization axis, can be realized by applying a radio frequency (RF) control field resonant with the nuclear Larmor frequency. In the frame that is rotating at nuclear Larmor frequency (rotating frame), the RF field appears to be static and can be described as

$$\mathcal{H}_c(t) = \omega_R(t) (\cos(\phi(t))\mathcal{I}_x + \sin(\phi(t))\mathcal{I}_y), \quad (2.4)$$

where  $\omega_R$  is the nutation or Rabi frequency and  $\phi$  is the phase that dictates the axis of rotation in the transverse plane. The internal Hamiltonian in the weak coupling limit enables

single qubit rotations about the quantization axis and two qubit controlled-Z gates. Combining the internal Hamiltonian with the control field, universal control can be achieved as long as the chemical shift and J-coupling parameters allow selective control over all spins in the system of interest.

## Readout process

With today’s NMR technology, it is impossible to detect the magnetic moment of a single nuclear spin directly. However, a sample with many copies of identical molecules dissolved in a liquid solvent ideally experience the same field and hence undergo identical quantum evolution. This is an example of the ensemble quantum computation model in which the only measurable quantities are expectation values of certain observables. This means that projective measurement is not available. Since nuclei have magnetic moments, a nuclear spin that is Larmor precessing around the z-axis creates a magnetic field along the xy-plane. Time-varying magnetic field in turn induces an oscillating current in the coil that is positioned perpendicular to the static magnetic field. The detectable transverse magnetizations can be expressed as:

$$M_x(t) = \text{Tr}(\rho(t)\sigma_x), \quad (2.5)$$

$$M_y(t) = \text{Tr}(\rho(t)\sigma_y), \quad (2.6)$$

where  $\rho(t)$  is the density matrix describing the spin and  $\sigma_i$  represents a Pauli operator. This signal is called the free-induction decay (FID), and a Fourier transform of the FID produces an NMR spectrum for further data analysis. The signal decays due to inhomogeneities in the magnetic field and intrinsic relaxation processes.

### 2.1.2 Solid state NMR

Solid state NMR (SSNMR) QIP makes use of the techniques developed in LSNMR QIP, and offers several advantages: the decoherence rates can be made slow using refocusing techniques, while spin-spin couplings much larger than in LSNMR can be exploited to realize faster quantum gates. Furthermore, SSNMR can be performed at cryogenic temperatures for providing higher spin polarizations than that is available in the room-temperature liquid state NMR. Features of the internal Hamiltonian of SSNMR that differ from LSNMR are the anisotropic chemical shift and dipole-dipole couplings between nuclei. The anisotropic chemical shift should be described by a second-rank tensor  $\Delta$  with 6 independent elements that represent the magnitude and direction of the chemical shielding. In the secular

approximation (at large static magnetic field), the form of the dipole-dipole interaction Hamiltonian depends on whether the interacting spins belong to the same isotopic species or not, and can be written as follows:

$$\text{Homonuclear: } \mathcal{H}_D^{ij} = d_{ij} \left( 3\mathcal{I}_z^i \mathcal{I}_z^j - \mathcal{I}^i \cdot \mathcal{I}^j \right), \quad (2.7)$$

$$\text{Heteronuclear: } \mathcal{H}_D^{ij} = d_{ij} \left( 2\mathcal{I}_z^i \mathcal{I}_z^j \right), \quad (2.8)$$

$$d_{ij} = -\hbar \frac{\mu_0}{4\pi} \frac{\gamma_i \gamma_j}{r_{ij}^3} \frac{3 \cos^2 \theta_{ij} - 1}{2}, \quad (2.9)$$

where  $\mu_0$  is the permeability of free space,  $\gamma_i$  is the gyromagnetic ratio of spin  $i$ ,  $r_{ij}$  is the distance between interacting spins, and  $\theta_{ij}$  is the angle between the vector connecting the two spins and the external magnetic field. There are also J-couplings in SSNMR, which are usually an order of magnitude smaller than the dipole-dipole couplings, and for which the isotropic component cannot be distinguished from dipolar couplings. Nuclei with  $S > 1/2$  interact with external electric field gradients, a phenomenon known as quadrupolar interaction. We limit our discussions to spin-1/2 systems, and hence quadrupolar interactions do not appear in the internal Hamiltonian.

### 2.1.3 State preparation in ensemble quantum computation

As mentioned in the previous section, NMR QIP is one example of ensemble quantum computation models, where a set of identical quantum systems is manipulated in parallel. In this section, we review concepts related to spin polarization and present the challenge in preparing nearly pure spin qubits.

#### Spin polarization

For a spin at temperature  $T$ , the occupancy of a state with energy  $E$  is calculated by the Gibbs distribution  $n(E) = \exp(-E/k_B T) / Z$ , where  $k_B$  is the Boltzmann constant and  $Z$  is the partition function. The polarization  $\epsilon$  is defined as the population difference between two energy levels normalized by the total number of spins. When the Zeeman energy dominates the energy splitting, the polarization of a spin-1/2 system can be expressed as

$$\epsilon = n(E_0) - n(E_1) = \tanh \left( \frac{\Delta E}{2k_B T} \right) = \tanh \left( \frac{\hbar \gamma B_0}{2k_B T} \right), \quad (2.10)$$

where  $\Delta E$  is the energy difference between the two levels,  $\gamma$  is the gyromagnetic ratio, and  $B_0$  is the strength of the external magnetic field. The equation 2.10 establishes the

relationship between polarization and gyromagnetic ratio, magnetic field strength, and temperature.

When the direction of the applied static magnetic field is defined as z-axis, the density matrix describing a spin ensemble at thermal equilibrium can be written in the eigenbasis of  $\sigma_z$  as

$$\rho = \frac{1}{2} \begin{pmatrix} 1 + \epsilon & 0 \\ 0 & 1 - \epsilon \end{pmatrix} = \frac{1}{2} (\mathbb{1} + \epsilon \sigma_z), \quad (2.11)$$

where  $\mathbb{1}$  is the unit matrix.

The entropy of any single qubit density matrix that can be expressed in the form of Eq. 2.11 is

$$S(\rho(\epsilon)) = -\frac{1 + \epsilon}{2} \log_2 \left( \frac{1 + \epsilon}{2} \right) - \frac{1 - \epsilon}{2} \log_2 \left( \frac{1 - \epsilon}{2} \right). \quad (2.12)$$

This is monotonically decreasing function in  $|\epsilon|$ . Therefore, increasing polarization of a single qubit is equivalent to decreasing the entropy of the single qubit system.

Moreover, the purity of a single qubit state is given by

$$\text{Tr}(\rho^2(\epsilon)) = \frac{1}{2} (1 + \epsilon^2). \quad (2.13)$$

This is monotonically increasing function in  $|\epsilon|$ . Therefore, increasing polarization of a single qubit is equivalent to increasing the purity of the single qubit system.

## Pseudo-pure state

For  $n$  spin qubits, the thermal equilibrium state can be transformed to a pseudo-pure state through non-unitary processes using standard NMR techniques of temporal or spatial averaging [39, 40]:

$$\rho_{pps}^n = (1 - \alpha) \mathbb{1}_n + \alpha |\psi\rangle\langle\psi|, \quad (2.14)$$

$$\alpha = \frac{(1 + \epsilon)^n - 1}{2^n - 1}, \quad (2.15)$$

where  $|\psi\rangle\langle\psi|$  is a pure state,  $\mathbb{1}_n$  is  $2^n \times 2^n$  normalized unit matrix, and  $\alpha$  quantifies the purity of the state. A typical NMR experiment operates at  $B_0 \approx 7$  T and room-temperature in which nuclear spin polarizations are extremely small ( $\epsilon \approx 10^{-5}$  for proton). Moreover, preparation of a pseudo-pure state without methods like algorithmic cooling that can compress entropy suffer from an exponential decrease of signal in the number of

qubits. For example, the partner pairing algorithm [28] can boost the polarization of a target spin to  $\epsilon_b 2^{n-2}$ , given  $n$  number of system qubits and the spin bath with polarization  $\epsilon_b < 2^{-n}$  [41]. Thus, the algorithmic cooling can compensate for the exponential signal loss in the number of qubits.

## 2.2 QEC with mixed ancilla qubits

In [23], augmented error correction is introduced which partially compensates for the error in ancilla qubits (i.e. in the presence of mixed ancilla qubits). The performance of QEC is improved so long as the ancilla qubit polarizations are above certain values which depend on the error correction code. For example, in the conventional 3-qubit QEC code for phase flip error [22], one can imagine that two ancilla qubits in the NMR experiment are in mixed states with polarizations  $\epsilon_1$  and  $\epsilon_2$ , respectively. In this case, the probability amplitude of the lowest energy state of the two qubit has to be greater than 0.5, i.e.  $(1 + \epsilon_1)(1 + \epsilon_2)/4 > 0.5$ , in order for QEC to suppress the error rate and improve the fidelity of a state exposed to the noisy channel. If  $\epsilon_1 = \epsilon_2 = \epsilon$ , then  $\epsilon > \sqrt{2} - 1 \approx 0.41$  must be satisfied. This is far above what can be achieved in a usual NMR setup. One can imagine having a solid state NMR setup in which the experiment can be carried out at low temperature. However, in order to meet the polarization requirement given above, the temperature must be below 17 mK for  $^1\text{H}$  at a field of 7 T. As the temperature is lowered, the nuclear  $T_1$  relaxation time is increased and therefore the wait time for thermal state initialization can become impractically long.

# Chapter 3

## Example applications of few-qubit NMR QIP

### 3.1 Introduction

Despite the difficulties in pure state preparation, NMR is one of the most successful QIP platform for controlling few-qubit systems allowing developments of new ideas and methods for understanding and controlling quantum systems. This chapter reports two interesting and useful applications of NMR QIP. The first section presents a liquid state NMR (LSNMR) experiment designed to test Born's rule, one of the foundational postulates of quantum mechanics using three-qubit quantum register. This work demonstrates the capability of LSNMR QIP for testing fundamental laws of quantum theory. In the second section, we investigate the strategies to design reliable  $T_{1\rho}$  noise spectroscopy [42, 43]. In the implementation of QIP, probing spectral density of noise is useful for the design and optimization of protocols for suppressing unwanted qubit-bath interaction. When the noise is reduced to below the threshold value for QEC, the quantum computation can be carried out fault tolerantly.  $T_{1\rho}$  noise spectroscopy has been studied and used by others [42, 43] based on the filter function [42, 44–60] and generalized Bloch equation [61] formalism. These approaches uses weak-coupling assumption between the system and the environment, and provide correct analysis only upto first order in the spectral density of noise. Moreover, previous approaches does not include rigorous analysis on the effect of finite probe bandwidth and inhomogeneous line broadening ( $T_2^*$ ). In our work, we use numerical simulations and perturbation series [62, 63] to study higher order effects and the finite probe bandwidth effect to provide more detailed picture that aids one to design reliable  $T_{1\rho}$



noise spectroscopy experiment. In addition, we examine the effect of the inhomogeneous line broadening in the experiment.

### 3.2 Testing Born's rule using liquid state NMR

Born's rule is one of the fundamental postulates of quantum mechanics which states that if a quantum mechanical state is described by a wavefunction  $\psi(\mathbf{r}, t)$ , then the probability of finding a particle at  $\mathbf{r}$  in the volume element  $d^3r$  at time  $t$  is [64]

$$p(\mathbf{r}, t)d^3r = \psi^*(\mathbf{r}, t)\psi(\mathbf{r}, t)d^3r = |\psi(\mathbf{r}, t)|^2d^3r. \quad (3.1)$$

Although many experimental results have been implicitly shown to be consistent with Born's rule, there have been no experimental efforts to test directly the validity of the theory until the recent optical experiment by Sinha *et al.* [65, 66]. Thus, a deviation from the theory, if there is any, might not have been evident. Therefore, it is very important to take steps towards direct experimental verification of the Born rule. Here we utilize liquid state NMR QIP techniques to test the Born rule. This work also shows that we have the ability to control small number of qubits using LSNMR with high accuracy to directly test fundamental laws of physics.

As a direct consequence of the Born rule, an interference pattern is produced when even a single particle travels through two slits. Quantum interference can be stated as a deviation from the classical interpretation of probability for mutually exclusive events (e.g. paths, slits, eigenstates and etc.) [65, 66]. For instance, quantum interference of two paths 1 and 2 is  $I_{12} = P_{12} - (P_1 + P_2)$ , where  $P_i$  is the probability for a path configuration  $i$ . Similarly, quantum interference of three paths 1, 2 and 3 can be written as  $I_{123} = P_{123} - (P_{12} + P_{13} + P_{23} - P_1 - P_2 - P_3)$ . According to Born's rule, three paths probability is

$$\begin{aligned} P_{123} &= |\psi_1 + \psi_2 + \psi_3|^2 \\ &= P_1 + P_2 + P_3 + I_{12} + I_{13} + I_{23} \\ &= P_{12} + P_{23} + P_{13} - P_1 - P_2 - P_3. \end{aligned} \quad (3.2)$$

Therefore, the Born rule predicts that  $I_{123} = 0$  [67]. Here we introduce  $P_0$  to denote the probability of detecting particles when all paths are blocked (ideally zero). Non-zero value of  $P_0$  may arise in the actual implementation due to experimental errors such as detector noise. Thus, the measured quantity in the experiment is

$$I_{123} = P_{123} - P_{12} - P_{13} - P_{23} + P_1 + P_2 + P_3 - P_0. \quad (3.3)$$

The three path experiment tests whether Eq. 3.3 is zero by observing the probabilities resulting from all possible combinations of independent paths being blocked and unblocked, and hence validate the Born rule.

### 3.2.1 Encoding three paths in energy eigenstates

Here we describe how to translate the triple-slit experiment [65, 66] into a form that can be implemented with NMR. When a photon travels through one of the eight possible slit configurations, the initial single path (of the photon before arriving at the slits) state evolves into another state which is determined by the slit configuration. Some photons are lost (not detected) by arriving at a path that is blocked, and a superposition of the unblocked paths is created. Due to this loss of photons, the overall transformation can be described as a non-trace preserving map. We encode this non-trace preserving map by an implementable unitary transformation on a larger Hilbert space.

Consider a four level system with energy eigenstates  $|0\rangle, |1\rangle, |2\rangle, |3\rangle$ . One can imagine the basis states  $|1\rangle, |2\rangle, |3\rangle$  as encoding the path taken by a photon in the triple-slit experiment [65, 66] as it travels through slit 1, 2 and 3, respectively. We can construct a superposition,  $|\psi^\gamma\rangle$ , of these four states to represent a particular slit pattern  $\gamma$ , as follows

$$|\psi^\gamma\rangle = \beta|0\rangle + \sum_{k=1}^3 \frac{\gamma_k}{\sqrt{3}}|k\rangle, \quad (3.4)$$

and  $\gamma$  is defined as

$$\gamma = \gamma_1\gamma_2\gamma_3 \in \{000, 001, 010, 100, 110, 101, 001, 111\},$$

where

$$\gamma_k = \begin{cases} 0 & \text{if path } k \text{ is blocked} \\ 1 & \text{if path } k \text{ is unblocked} \end{cases} ,$$

and  $\beta$  is determined from the normalization condition. The amplitude,  $\beta$ , of the state  $|0\rangle$  captures the probability that a photon does not arrive at the detector due to any blocked paths. For example, when all three paths are open,  $\beta = 0$  and all photons reach the detector. On the other hand, for  $\beta = 1$ , the state encoding the slit information is  $|0\rangle$ . This state represents that all three slits are closed and is used for calculating the background probability  $P_0$  which can be non-zero due to experimental imperfections. Tab. 3.1 illustrates all possible slit patterns that match with the path configuration label  $\gamma$ , and the corresponding superposition states  $|\psi^\gamma\rangle$ .









| $\gamma$ | Slit Pattern  | $ \psi^\gamma\rangle$                                   |
|----------|---|---|
| 000      |  | $ 0\rangle$   |
| 001      |  | $\frac{1}{\sqrt{3}}(\sqrt{2} 0\rangle +  3\rangle)$     |
| 010      |  | $\frac{1}{\sqrt{3}}(\sqrt{2} 0\rangle +  2\rangle)$     |
| 100      |  | $\frac{1}{\sqrt{3}}(\sqrt{2} 0\rangle +  1\rangle)$     |
| 011      |  | $\frac{1}{\sqrt{3}}( 0\rangle +  2\rangle +  3\rangle)$ |
| 101      |  | $\frac{1}{\sqrt{3}}( 0\rangle +  1\rangle +  3\rangle)$ |
| 110      |  | $\frac{1}{\sqrt{3}}( 0\rangle +  1\rangle +  2\rangle)$ |
| 111      |  | $\frac{1}{\sqrt{3}}( 1\rangle +  2\rangle +  3\rangle)$ |

Table 3.1: Table of all possible path arrangements that can be formed from three independent paths and superposition states that encode each configuration. We first form the equal superposition state  $|\psi^{111}\rangle$  to encode three slits, and then write other superposition states for the rest of slit configurations according to Eq. 3.4 such that the amplitudes for each states  $|j\rangle$  with  $j \in \{1, 2, 3\}$  are either 0 (when the path is blocked) or  $1/\sqrt{3}$  (when the path is open) for all  $|\psi^\gamma\rangle$ , and the amplitude,  $\beta$ , of the state  $|0\rangle$  is chosen to satisfy the normalization condition.

Moreover, we introduce  $\tau$  to parameterize the evolution between the coherence creation and detecting interference.  $\tau$  is directly related to the position of the detector with respect to some central position in the triple-slit experiment [65, 66]. Suppose the state  $|\psi^{111}\rangle\langle\psi^{111}|$  evolves under the Hamiltonian  $\mathcal{H}_0 = E_0|0\rangle\langle 0| + E_1|1\rangle\langle 1| + E_2|2\rangle\langle 2| + E_3|3\rangle\langle 3|$  for  $\tau$ . Then the evolved state would have the following form:

$$|\psi^{111}(\tau)\rangle = \sum_{j=1}^3 \frac{e^{-i\Delta_j\tau}}{\sqrt{3}}|j\rangle, \quad (3.5)$$

where  $\Delta_j = E_j - E_0$ . Born's rule for probability dictates that

$$P_\gamma(\tau) = |\langle\psi^\gamma|\psi^{111}(\tau)\rangle|^2, \quad (3.6)$$

where the subscript  $\gamma$  indicates the path configuration of which the probability is measured. We can analytically calculate  $P_\gamma(\tau)$  for all  $\gamma$  and confirm that Eq. 3.3 vanishes for all  $\tau$ ,

$E_0$ ,  $E_1$ ,  $E_2$  and  $E_3$  if the Born rule holds:

$$\begin{aligned}
I(\tau) &= P_{111}(\tau) - P_{110}(\tau) - P_{101}(\tau) - P_{011}(\tau) + P_{100}(\tau) + P_{010}(\tau) + P_{001}(\tau) - P_{000}(\tau) \\
&= \frac{1}{3} + \frac{2}{9}[(\cos(\Delta_2 - \Delta_1) + \cos(\Delta_3 - \Delta_1) + \cos(\Delta_3 - \Delta_2))\tau] - \frac{2}{9}[1 + \cos(\Delta_2 - \Delta_1)\tau] \\
&\quad - \frac{2}{9}[1 + \cos(\Delta_2 - \Delta_1)\tau] - \frac{2}{9}[1 + \cos(\Delta_2 - \Delta_1)\tau] + \frac{1}{9} + \frac{1}{9} + \frac{1}{9} - 0 = 0. \tag{3.7}
\end{aligned}$$

### 3.2.2 Experiment

The three path experiment with LSNMR can be illustrated as a quantum circuit in Fig. 3.1. Two qubits are used for encoding three paths, and a third (probe) qubit is added for read

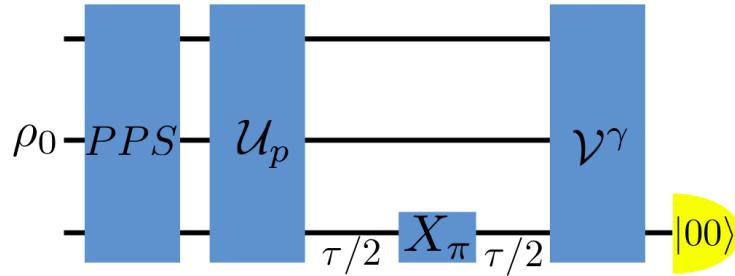


Figure 3.1: Quantum circuit for the three path experiment: The third (probe) qubit is used to read out the information encoded in the first two qubits. PPS denotes the pseudo-pure state [68] preparation procedure. A  $\pi$  pulse along x-axis ( $X_\pi$ ) applied to the third qubit at  $\frac{\tau}{2}$  turns off unwanted interactions between the third read-out qubit and the two computation qubits. The unitary gate  $\mathcal{U}_p$  prepares  $|\psi^{111}\rangle$ , and the state evolves for  $\tau$  into  $|\psi^{111}(\tau)\rangle$ . Applying unitary  $\mathcal{V}^\gamma$  and measuring the magnetization of the probe qubit conditional on the first two qubits being in the  $|00\rangle$  basis give the probability  $P_\gamma(\tau)$ .

out. As a part of the initial state preparation, we perform RF selection [37, 69, 70] in order to reduce the inhomogeneity of the RF field strength experienced by our liquid sample. Then a pseudo-pure state (PPS) [68] is prepared by an algorithm proposed in [71]. We use magnetic gradient pulses along the z-axis (the direction of static magnetic field) for labelling the coherence and decoding it to a pseudo-pure state. The output pseudo-pure state is  $\alpha(|00\rangle\langle 00| \otimes X)$  where  $\alpha$  is the initial reference spin polarization. The unitary gate  $\mathcal{U}_p$  prepares  $|\psi^{111}\rangle$ , then the state undergoes free evolution for a time  $\tau$ . We apply a refocusing  $\pi$  pulse along x-axis (denoted as  $X_\pi$  in Fig. 3.1) at time  $\tau/2$  after  $\mathcal{U}_p$  in order to average out unwanted interactions between the third qubit and the two computation

qubits.  $\mathcal{V}^\gamma$  transforms the amplitude of the interference from configuration  $\gamma$  to the state  $|00\rangle$  and yields the final state whose deviation (traceless) part [68] is  $\rho_f^\gamma = \alpha'_\gamma(|00\rangle\langle 00| \otimes X)$ , where  $\alpha'_\gamma = \alpha P_\gamma(\tau)$ . Then we measure the magnetization of the third qubit conditional on the first two qubits being in the  $|00\rangle$  state. In other words, the signal is the overlap of the final state with the PPS,  $|00\rangle\langle 00| \otimes X$ :

$$\begin{aligned} M_f &= \text{Tr} \left( \rho_f^\gamma (|00\rangle\langle 00| \otimes X) \right) \\ &= \alpha'_\gamma \text{Tr} \left( (|00\rangle\langle 00| \otimes X) (|00\rangle\langle 00| \otimes X) \right) = \alpha'_\gamma. \end{aligned} \quad (3.8)$$

The final state magnetization is normalized by the PPS magnetization to calculate  $P_\gamma(\tau)$ .

The three path experiment was performed in LSNMR on a 700 MHz Bruker Avance spectrometer at 293 K. A three qubit molecule was prepared from a sample of selectively labelled  $^{13}\text{C}$  tris(trimethylsilyl)silane-acetylene (TTMSA) dissolved in deuterated chloroform (Fig. 3.2a). Natural Hamiltonian parameters that are relevant for the experiment are shown in Fig. 3.2b. Two  $^{13}\text{C}$ 's are used to carry out the computation while the spectrum of  $^1\text{H}$  is measured. In the experiment, we used the Gradient Ascent Pulse Engineering

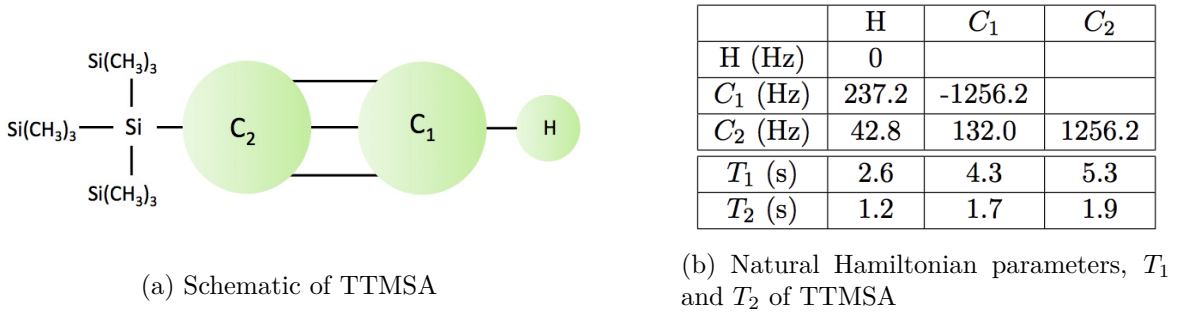


Figure 3.2: (a) Schematic of a three qubit molecule used for the experiment (not in scale): A proton ( $^1\text{H}$ ) and two carbons ( $^{13}\text{C}$ ) are used for realizing qubits. (b) A table of natural Hamiltonian parameters (Hz),  $T_1$  and  $T_2$  (s): The diagonal elements give the chemical shifts with respect to the transmitter frequencies. The off-diagonal elements are the J-coupling constants.

(GRAPE) [72] numerical optimization technique (see Sec. 4.4.2) to find RF pulse shapes that implement  $\mathcal{U}_p$ ,  $\mathcal{V}^\gamma$ , and the unitary gates involved in the PPS preparation with above 99.95% Hilbert-Schmidt (HS) fidelity.

Fig. 3.3 illustrates an example of LSNMR spectra of  $^1\text{H}$  attained from an experiment for measuring  $P_\gamma(\tau)$ . For this particular example,  $\gamma = 111$  and  $\tau = 0$ .

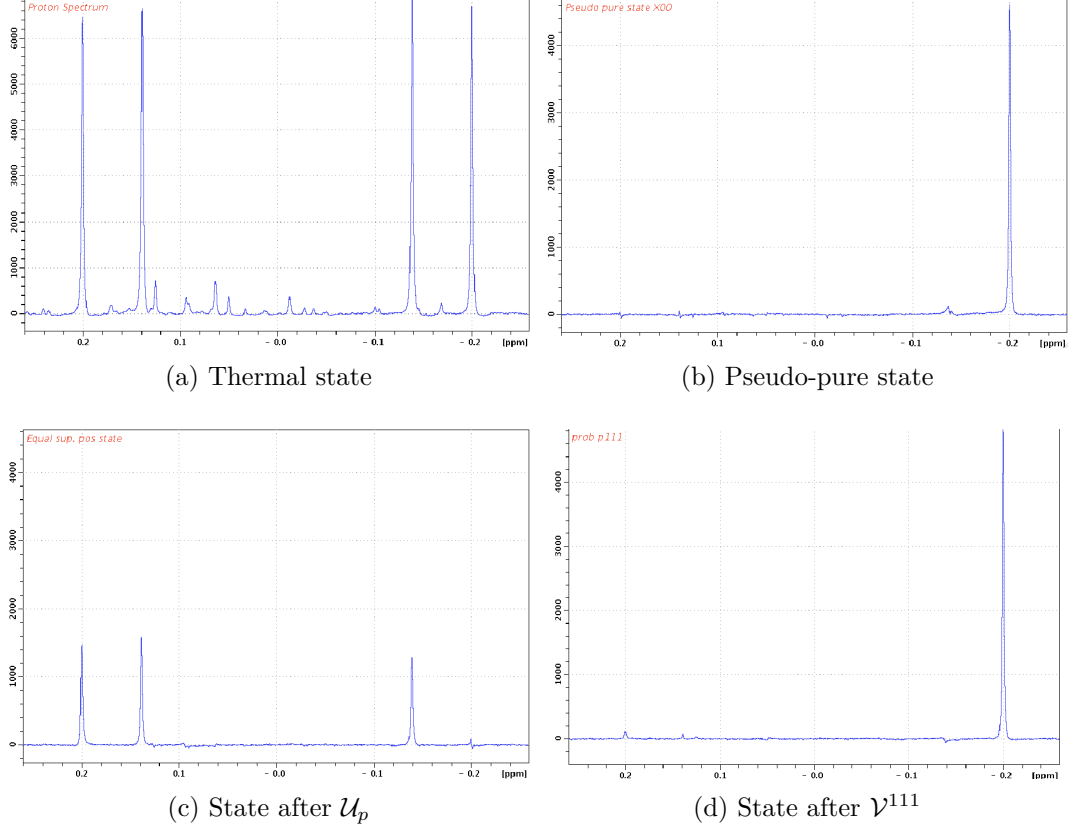


Figure 3.3:  $^1\text{H}$  spectrum is used to gain information about the state of two  $^{13}\text{C}$ 's. Vertical axis corresponds to magnetization amplitude and horizontal axis is frequency of spin precession. (a) is the initial thermal state spectrum of  $^1\text{H}$ , and the four peaks are due to four possible states of other two qubits. After applying PPS (Fig. 3.1), we obtain a three qubits pseudo-pure state (b). (c) shows the equal superposition state  $|\psi^{111}\rangle\langle\psi^{111}|$  of the two carbons. Finally, (d) is the spectrum we obtain after applying  $\mathcal{V}^{111}$ .

In the experiment, we evaluate the quantity

$$\kappa = \frac{I(\tau)}{|I_{110}(\tau)| + |I_{101}(\tau)| + |I_{011}(\tau)|}, \quad (3.9)$$

where  $I(\tau)$  is the three paths interference, and the denominator is the sum of magnitudes of two paths interferences (e.g.  $I_{110}(\tau) = P_{110}(\tau) - P_{100}(\tau) - P_{010}(\tau) + P_{000}(\tau)$ ). In this way, one can assure that the experiment is dealing with a quantum phenomenon inasmuch

as the denominator should vanish in the classical case [65, 66]. Moreover, the calculation of such quantity is straight-forward in our experimental set-up. As mentioned in the previous section,  $P_\gamma(\tau)$  is obtained by normalizing the magnetization of the final state measured after unitary gate  $\mathcal{V}^\gamma$  with that of the initial pseudo-pure state. Thus we run two experiments consecutively, first to measure the magnetization of the initial pseudo-pure state and second to measure the magnetization of the state acquired from the full quantum circuit (Fig. 3.1). These two measurements are separated by 25 s (about five times larger than  $T_1$ ) in order for spins to re-thermalize.

We sample  $\kappa$  for various  $\tau$  from 0  $\mu\text{s}$  to 1900  $\mu\text{s}$  with discretization  $\delta\tau = 100 \mu\text{s}$ . For each  $\tau$ , we repeat the experiment ten times providing 200 data in total. We obtained the weighted sample mean (WSM)  $\bar{\kappa} = 0.007 \pm 0.003$ . WSM is appropriate for the data analysis since the size of standard deviation varies for different  $\tau$ . The random error is the standard error of the WSM of  $\kappa$ . The results are shown in Fig. 3.4. The red dots are the average of ten repetitions of the experiment and the size of the error bars indicate standard deviations of the average. The black circles represent simulation results. The simulation assumes that the GRAPE and hard pulses designed for the experiment are implemented with no error under the effect of  $T_2$  and uses Born’s rule to extract magnetization signal of the final state.

### 3.2.3 Analysis of possible sources of error

As shown in Fig. 3.2b, the difference between Larmor frequencies of  $C_1$  and  $C_2$  is an order of magnitude larger than the J-coupling and thus we are well into the weak coupling approximation. A simulation of the neglected strong coupling terms shows that on our time scale for  $\tau$ , their contribution is negligible. Next, there are distortions in the implementation of shaped RF pulses [37, 38, 73]; the GRAPE pulses seen by the molecule in the LSNMR spectrometer do not exactly match to what we desire. There are two components to this deviation; random errors and a systematic portion that is primarily caused by limitations of the probe circuit design. The systematic imperfection can be rectified by placing a pickup coil at the sample’s place and closing a feedback loop to iteratively correct the RF pulse shapes [37, 38, 73]. This method improves (yet, still not perfect) the closeness of the actual pulse to the desired pulse. Random fluctuations of the RF field are inevitable in the experiment. The RF variations for the  $^1\text{H}$  channel and the  $^{13}\text{C}$  channel are found to be 0.7% and 0.2%, respectively. The RF selection process mentioned in Sec. 3.2.2 is very sensitive to this RF field variations since it is designed to select a subset of the ensemble of spins at a specific nutation frequency [37, 38, 74]. Thus the RF selection sequence in the presence of random RF fluctuations can introduce large fluctuations in

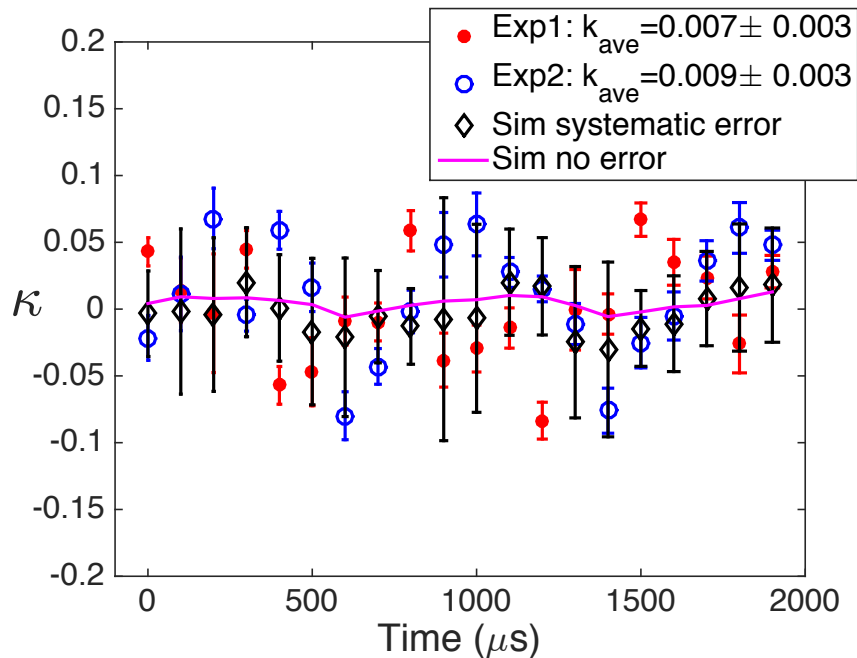


Figure 3.4: Experimentally determined  $\kappa$ : The experiment is repeated ten times for each  $\tau$ , giving 200 data points in total. The red indicates the experimental outcomes and the size of the error bars represents standard deviation. We acquired from the experiment the weighted sample mean  $\bar{\kappa} = 0.007 \pm 0.003$ . The blue circles and error bars are obtained by repeating the experiment (again, 200 data in total) with the different measurement method explained in the following section. The results from the second method are  $\bar{\kappa} = 0.009 \pm 0.003$ . The black squares are obtained from the simulation which assumes the Born rule holds and perfect implementations of the GRAPE and hard pulses under the effect of  $T_2$ . Here  $\bar{\kappa} = 0.004 \pm 0.001$ , and its deviation from zero is due to the fidelity of GRAPE pulses and  $T_2$ . The green is the outcome of the simulation that takes systematic errors such as distortions in the implementation of GRAPE pulses and RF field fluctuations into account. This simulation gives  $\bar{\kappa} = -0.002 \pm 0.001$ . The systematic errors well explain the small deviation of experimentally determined  $\kappa$  from zero; red and blue (experiment) overlap with green (systematic errors simulation) for most of the  $\tau$ 's, with less than one standard deviation away when there is no overlap.

the signal generated by pseudo-pure states. In other words,  $M_i$  obtained from a reference pseudo-pure state deviates from  $M_i$  of the following experiment in which the spin state goes through the full quantum circuit (Fig. 3.1) and only  $M_f$  is accessible. This leads



to error in the probability calculation. We prepared 100 pseudo-pure states following the RF selection consecutively and observed 0.95% fluctuation in the integrated spin signal on average with the worst case being about 2%. This kind of fluctuation translates to  $\bar{\kappa} \sim 10^{-3} \pm 10^{-4}$ . The green rhombi and error bars in Fig. 3.4 show the systematic errors due to distortions in the implementation of GRAPE pulses and the random fluctuation of RF field. We performed another set of experiments with a different measurement method. Instead of taking two experiments to find the probabilities as described earlier, we opened the receiver at the end of the pseudo-pure state preparation for a short time, and opened the receiver again after  $\mathcal{V}^\gamma$  so that the reference magnetization and the final magnetization are obtained from a single experiment. We hoped to see some improvement in this method by removing slow RF fluctuations between two experiments. Nevertheless, there was no significant improvement; we obtained  $\bar{\kappa} = 0.009 \pm 0.003$ . The results from this method is indicated as blue in Fig. 3.4. There are other possible sources of error such as transient effect from refocusing pulses due to their fast varying amplitude profile and disturbance of static field due to gradient pulses used for pseudo-pure state preparation. Furthermore, for the three qubit molecule TTMSA in LSNMR, the average error per gate is found to be  $\sim 10^{-3}$  from randomized benchmarking in [74]. Such a gate error contributes to  $\bar{\kappa} \sim 10^{-4}$ .

Finally, we conclude that our experiment bounded the deviation of the Born rule to  $\bar{\kappa} \sim 10^{-3} \pm 10^{-3}$ . Furthermore, we have demonstrated the capability of LSNMR QIP techniques for testing a fundamental postulate of quantum mechanics [75–79].

### 3.3 Qubit noise spectroscopy using NMR

The problem of a qubit interacting with a noisy environment is of fundamental importance in the field of quantum information processing. For many solid-state qubits, single-axis (phase) noise is dominant, and treating the noisy environment in a stochastic semi-classical approximation suffices to describe the qubit dephasing process. For example, a system-environment Hamiltonian of the form  $\mathcal{H}_{\mathcal{S}\mathcal{E}} = \mathcal{S}_z \sum_m \lambda_m \mathcal{E}_z^m$ , where  $\mathcal{S}$  and  $\mathcal{E}$  are spin-1/2 operators for the system and the environment, respectively, and  $\lambda_m$  are the coupling strengths, is approximated as  $\mathcal{H}_{\mathcal{S}}(t) = f(t)\mathcal{S}_z$  by tracing over the environmental degrees of freedom [49, 61]. In the limit of many environment qubits forming a spin bath, with intra-bath couplings strong compared to  $\lambda_m$ ,  $f(t)$  can be treated as a random, Gaussian-distributed function with zero mean.

In such a context, knowledge of the spectral density function  $S(\omega)$ , the Fourier transform of the two-point correlation function for  $f(t)$ , is useful for the design and optimization of dynamical decoupling and error correction schemes. Recently, interest has developed

in using dynamical decoupling to probe  $S(\omega)$  [42, 43, 49, 51, 56, 57, 60, 80–82]. This can be understood intuitively using the overlap integral approach [42, 44–60]. For example, a series of equally spaced  $\pi$  pulses produces a time domain filter function that alternates between  $+1$  and  $-1$  values at a period corresponding to the pulse spacing  $\tau$  (Fig. 3.5a), so that in the frequency domain the filter function is peaked at the corresponding probing frequency  $\omega_p = 1/(2\tau)$  (Fig. 3.5c). Under such a pulse sequence, the qubit is most sensitive to the spectral density of the noise at this probe frequency,  $S(\omega_p)$ , hence the qubit decay rate measured as a function of  $\omega_p$  can approximate  $S(\omega)$ .

An exponential decay of qubit coherence is predicted [46–48],

$$\langle \mathcal{S}_x(T) \rangle = \langle \mathcal{S}_x(0) \rangle \exp(-\chi(T)), \quad (3.10)$$

where

$$\chi(T) = \sqrt{\frac{\pi}{2}} \int_{-\infty}^{\infty} d\omega S(\omega) |F(\omega, T)|^2, \quad (3.11)$$

is determined by the overlap of the noise spectral density with the frequency domain filter function,  $|F(\omega, T)|^2$ , for a sequence of duration  $T$ . Note that  $F(\omega, T)$  is the Fourier transform of the time domain filter. Also note that if the Hamiltonian does not commute with itself at all times, Eq. 3.11 is an approximation taking only the first order component of the filter function into account [44]. Here,  $\chi(T) = RT$  where  $R$  is the coherence decay rate that in general depends on  $T$ , however will be constant in the cases of interest to us. Eq. 3.11 can be rewritten in matrix form,

$$\vec{\chi} = \mathbf{F} \cdot \vec{S}, \quad (3.12)$$

where  $\vec{\chi}$  and  $\vec{S}$  are the vectorized decay function and spectral density corresponding to discrete measurements in an experiment. The matrix  $\mathbf{F}$  is a discretized version of  $|F(\omega, T)|^2$ . Determining the noise spectrum amounts to inverting  $\mathbf{F}$ , however strictly speaking  $\mathbf{F}$  is not invertible because it has at least one zero eigenvalue. This can be seen from the fact that  $|F(\omega, T)|^2 = 0$  for  $T = 0$  regardless of the construction of the pulse sequence. The non-invertibility of  $\mathbf{F}$  implies that the problem is ill-posed: there does not in general exist a unique solution  $\vec{S}$  to a dataset  $\vec{\chi}$ . Intuitively, if the function  $|F(\omega, T)|^2$  is spectrally broad or peaked at many frequencies, extracting  $S(\omega)$  with high accuracy becomes very difficult, particularly if the functional form of  $S(\omega)$  is not known a priori, which we will assume throughout this work. In particular,  $|F(\omega, T)|^2$  will be spectrally broad unless there are a sufficient number of decoupling cycles, i.e.  $T \gg 2\tau$  where  $2\tau$  is the decoupling period. Under the latter condition, the filter function approaches a delta function at the probing frequency  $\omega_p$ , and at its higher harmonic frequencies (Fig. 3.5c) by the fact that the time

domain filter is a square wave (Fig. 3.5a). As already mentioned, for the first order approximation with the higher harmonics neglected, Eq. 3.11 predicts an exponential signal decay at a rate proportional to  $S(\omega_p)$ . A method for taking these harmonics into account in the extraction of  $S(\omega)$  was developed and demonstrated experimentally by Gonzalez et al [51]. The method requires that the number of decoupling cycle is large enough to justify the approximation that the peaks in the frequency domain filter function are delta-functions. The pulsed method becomes disadvantageous at high probing frequencies, when finite pulse width effects cannot be ignored and limit the minimum practical pulse spacing. Moreover, the experimental implementation of pulsed method can be cumbersome in some cases owing to the harmonics of the frequency domain filter function. For example, even for obtaining the noise strength at one particular frequency, the pulsed method requires the noise information at the harmonic frequencies, and hence probing the noise spectrum over the large range of frequency.

An alternate approach using continuous wave (CW) decoupling was first proposed, to our knowledge, by Geva *et al.* in their seminal paper deriving the generalized Bloch equations (GBE) [61]. Note that spin-locking, or  $T_{1\rho}$  experiments, using CW irradiation have been used for decades in NMR to probe relaxation processes at frequencies intermediate between  $T_2$  processes, dominated by  $S(0)$ , and  $T_1$  processes, dominated by  $S(\omega_L)$  where  $\omega_L$  is the Larmor frequency. For example,  $T_{1\rho}$  experiments have probed slow atomic motions that give rise to fluctuations in the dipolar field [83–86]. These studies link a mean hopping time of nuclear spins between lattice sites with the magnetization decay rate. The NMR literature, however, has not directly addressed the problem of quantitatively extracting an unknown and arbitrary  $S(\omega)$  from a series of  $T_{1\rho}$  measurements. This was first addressed in the context of the GBE formalism [61, 80]. It was later suggested in the context of the overlap integral method as a possible means for noise spectroscopy [87], but the details were not explicitly worked out. At first glance, a treatment based on filter functions would appear difficult, since in the interaction frame of a CW field along  $S_x$  in the rotating frame, the semi-classical noise Hamiltonian transforms with time  $t$  as

$$\begin{aligned}\tilde{\mathcal{H}}(t) &= \exp(i\omega_p \mathcal{S}_x t) (f(t) \mathcal{S}_z + \omega_R \mathcal{S}_x) \exp(-i\omega_p \mathcal{S}_x t) \\ &= f(t) (\cos(\omega_p t) \mathcal{S}_z + \sin(\omega_p t) \mathcal{S}_y).\end{aligned}\tag{3.13}$$

and it is not obvious how to correctly take into account the non-commuting Hamiltonian. Nevertheless, qualitatively correct fidelity decay can be recovered from the overlap integral method, correct to second order in the coupling  $f(t)$  [42], and hence to first order in the spectral density  $S(\omega)$ . As expected, the first order filter function corresponding to a driving field with many periods,  $n = \omega_p T / (2\pi) \gg 1$ , is narrowly peaked around  $\omega_p$ , with no harmonics (Fig. 3.5d). The result of the overlap integral method presented in [42] is

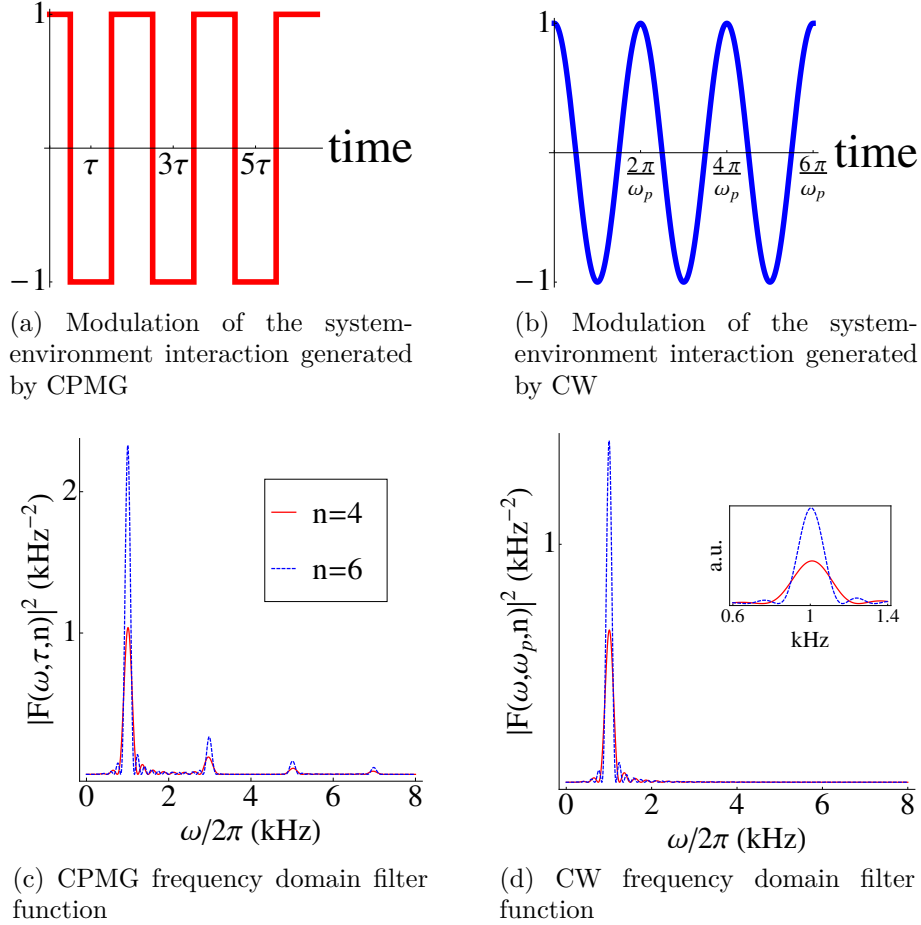


Figure 3.5: Modulation of the system-environment interaction in the interaction frame generated by (a) CPMG, and (b) continuous wave (CW) decoupling if one fictitiously considers only the  $\mathcal{S}_z$  component. The switches between  $\pm 1$  in (a) correspond to application of a  $\pi$ -pulse. Frequency domain filter functions (c) and (d) correspond to the modulation functions in (a) and (b), respectively. The CPMG frequency domain filter function consists of sinc functions centered at  $k\pi/\tau$ , where  $k$  is an odd integer. The fictitious CW filter function is a sinc-like function centered at  $\omega_p$ . In these examples,  $\omega_p/2\pi = 1$  kHz,  $\tau = \pi/\omega_p$ , and  $n = \{4, 6\}$ , where  $2n$  is the number of  $\pi$  pulses in CPMG and  $n = \omega_p T/2\pi$  is the number of Rabi cycles for CW irradiation.

qualitatively consistent with the GBE prediction; in the case of a  $T_{1\rho}$  (spin-locking) type experiment, these predict an exponential decay of coherence  $\langle \mathcal{S}_x \rangle$  with a decay rate directly

proportional to  $S(\omega_p)$ . This idea was demonstrated experimentally in optically-trapped ultracold atoms coupled to a collisional bath [42], and in the context of superconducting qubit decoherence [43]. In the latter case, the analysis was based on the GBE and included more general noise (relaxation) than considered here.

The  $T_{1\rho}$  noise spectroscopy can be much simpler to implement compared to the pulsed method, because the first order filter function in the frequency domain does not have harmonics (Fig. 3.5d) and hence the noise spectrum at a particular frequency can be approximated using a CW decoupling pulse only at the target probing frequency. Despite the experimental simplicity, the  $T_{1\rho}$  noise spectroscopy is more difficult to analyze owing to non-trivial spin dynamics during the irradiation of the CW pulse. As mentioned above, the GBE provides only the second order in  $f(t)$  (thus first order in  $S(\omega)$ ) description of the spin dynamics under the application of the CW pulse, and the description is valid only in the limit of large number of driving field periods,  $n \gg 1$ . The  $T_{1\rho}$  method additionally suffers from a low excitation bandwidth at long probing times  $T$ . If the qubit linewidth is broadened inhomogeneously, a spectrally narrow CW excitation will only be on resonance for the central ‘spin packet’ and this will complicate analysis of the signal decay.

In this work, we present our on-going study on the effect of three issues mentioned above to the problem of  $T_{1\rho}$  noise spectroscopy of pure dephasing noise: (1) terms beyond first order in  $S(\omega)$  that may become significant in the strong system-bath coupling regime, (2) violation of the delta function approximation, and (3) inhomogeneous line broadening. Numerical simulations and perturbation series are the main tools for investigating the aforementioned problems. Combining the results we have so far, we present a more detailed picture of  $T_{1\rho}$  noise spectroscopy than has been previously discussed [42, 43]. The final goal of this analysis is to enable experimentalists to design a protocol, which may involve both pulsed and  $T_{1\rho}$  experiment, to reliably construct the spectral density of noise over as wide frequency range as possible. Finally, we perform  $T_{1\rho}$  and the pulsed noise spectroscopy in both liquid and solid state NMR systems. The purpose of the liquid state NMR experiment is for testing and developing ideas of the noise spectroscopy exploiting a well-known single qubit system, while the solid state experiment is designed to estimate the effective spectral density of noise on a  $^{13}\text{C}$  probe qubit due to a bath of dipolar coupled proton spins. Excellent agreement between  $T_{1\rho}$  and the pulsed methods is observed in both liquid and solid state experiments. The agreement between the two noise spectroscopy methods suggests that the pulsed and  $T_{1\rho}$  methods can complement each other to extend the frequency range of the noise spectral density.

### 3.3.1 Generalized Bloch equations

The generalized Bloch equations were derived in [61] to describe the relaxation dynamics of a system simultaneously interacting with a heat bath and a driving field of arbitrary intensity. The derivation uses the Dyson expansion for solving the evolution of the time-dependant Hamiltonian [62], and it is based on the following assumptions: (1) the system and the bath are weakly coupled, and are initially in a product state. The weak coupling assumption allows the GBE to neglect terms beyond second order in  $f(t)$ , which is equivalent to the first order in  $S(\omega)$ ; (2) the time scale of the relaxation of the system is much slower than that associated with the decay of the bath correlation functions (Markov approximation) and the period of the driving field  $2\pi/\omega_p$ ; (3) the bath-induced coherent system dynamics are negligible compared to that induced by the system Hamiltonian. The GBE show that the bath terms become dependent on the frequency and amplitude of the driving field.

The GBE are easily applied to analyze the coherence decay in a  $T_{1\rho}$  type experiment, where the CW field is on resonance with amplitude  $\omega_p$  and the high temperature limit  $k_B T \gg \hbar\omega_p$  applies. The transverse spin magnetization is then governed by

$$\frac{d}{dt}\mathcal{S}_x = -\frac{1}{2}\tilde{C}_{\Delta\Delta}(\omega_p)\mathcal{S}_x, \quad (3.14)$$

where  $\tilde{C}_{\Delta\Delta}$  is the Fourier transform of the bath correlation function

$$C_{\Delta\Delta}(\tau) = \text{Tr}_E (\Delta(\tau)\Delta\rho_E). \quad (3.15)$$

The notation  $\Delta$  in [61] is equivalent to the effective environment operator

$$\sum_m \lambda_m \mathcal{E}_z^m / \sqrt{\sum_m \lambda_m^2} \quad (3.16)$$

in our notation, and  $\Delta(\tau) = \exp(i\mathcal{H}_b\tau)\Delta\exp(-i\mathcal{H}_b\tau)$  with the bath Hamiltonian  $\mathcal{H}_b$ , and  $\rho_E$  is the density matrix describing the environment. If  $f(t)$  is Markovian,  $S(\omega_p) = \tilde{C}_{\Delta\Delta}(\omega_p)$ , and the GBE predict a signal decay

$$\langle \mathcal{S}_x(t) \rangle = \langle \mathcal{S}_x(0) \rangle \exp\left(-\frac{1}{2}S(\omega_p)t\right). \quad (3.17)$$

To measure a decay requires  $S(\omega_p)T \sim 1$ , and to be in the delta-function approximation regime requires  $n = \omega_p T / 2\pi \gg 1$ . These together imply  $\omega_p / 2\pi \gg S(\omega_p)$ . Using the definition of the spectral density of noise:

$$S(\omega) = \int_{-\infty}^{\infty} \langle f(t)f^*(t-\tau) \rangle \exp(-i\omega\tau) d\tau, \quad (3.18)$$

where the brackets represent a time average over  $t$  in the limit of large  $T$ , it is easy to see that the mean-square amplitude of the noise is  $\langle |f(t)|^2 \rangle = \frac{1}{2\pi} \int_{-\infty}^{\infty} S(\omega) d\omega$ . Therefore  $S(\omega_p)\Delta\omega = S(\omega_p)2\pi/T \leq 2\pi\langle |f(t)|^2 \rangle$ . Reliable noise spectroscopy is guaranteed if the smallest driving field amplitude satisfies  $\omega_p^{min}/(2\pi T) \gg \langle |f(t)|^2 \rangle$ , although this is not a strictly necessary condition.

### 3.3.2 Overlap integral method

Almog *et al.* [42] derive a master equation for the density matrix evolution in the interaction frame of Eq. 3.13 to second order in the noise function  $f(t)$ . The assumptions made are a weak coupling to the bath and that the noise function has zero mean. The fidelity of the evolved state with respect to the initial state is written in terms of a spectral overlap integral in order to derive a relationship between the signal decay and a filter function describing the control field. For a CW on-resonance field and many decoupling periods,  $n \gg 1$ , the filter function consists of sinc functions centered at  $\pm\omega_p$ . Integrating the filter function yields  $\int_{-\infty}^{\infty} |F(\omega, T)|^2 d\omega = T/2$ , so that in the limit  $T \rightarrow \infty$  the filter function becomes a delta function at  $\pm\omega_p$  and  $\chi = RT = S(\omega_p)T/4$ . This result qualitatively matches the GBE prediction, but curiously differs by a factor of two. We suspect that the difference is due to not taking the higher order filter function effects into account properly.

In order to test the validity of the conventional  $T_{1\rho}$  noise spectroscopy, we numerically simulate the spin signal decay under the full spin Hamiltonian in the form Eq. 3.13 with an input noise function and use Eq. 3.17 to extract the noise spectrum to see if the input noise function can be accurately reconstructed. The input noise functions are chosen to be in  $S(\omega) = 2\pi c/\omega$ , where  $c$  parametrizes the strength of the noise. Fig. 3.6 shows the simulation results for  $c = 300$  and  $c = 3000$ . The extracted noise spectrum matches the input acceptably well in the regime  $\omega_p/(2\pi S(\omega_p)) \geq 2$ . On the other hand, when  $\omega_p/(2\pi S(\omega_p)) < 2$ , the extracted one underestimates the true noise spectrum. Hence from the simulation results, we deduce that for  $1/\omega$  type of noise,  $\omega_p/(2\pi S(\omega_p)) \geq 2$  is the necessary condition for the reliable  $T_{1\rho}$  noise spectroscopy, which is consistent with the intuitively guessed sufficient condition  $\omega_p/2\pi \gg S(\omega_p)$ .

At this point, it is not clear what is the role of higher order terms in  $f(t)$ , (or  $S(\omega)$ ) and violation of the delta-function approximation in explaining the deviation shown in Fig. 3.6. Moreover, we do not know whether the qualitative form of the deviation is true for general noise or is only applicable to the example noise form we chose. Answering these questions will be useful for designing a protocol which can correct the error in the extracted noise spectrum to provide more accurate  $S(\omega)$ .

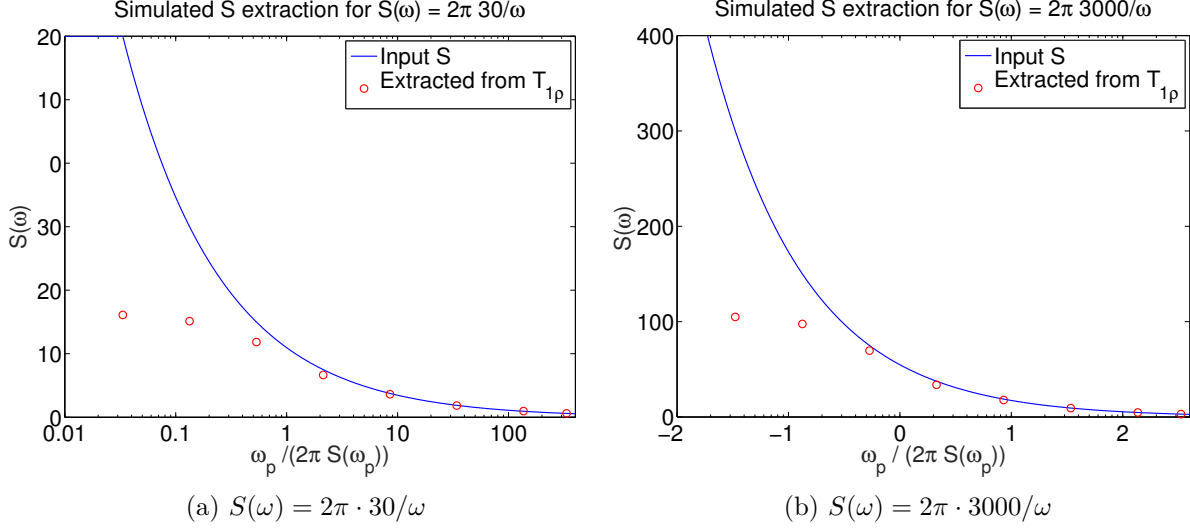


Figure 3.6: Blue curve is an input noise spectrum in the numerical simulation. The simulation uses the input  $S(\omega) = 2\pi c/\omega$  for (a)  $c = 30$  and (b)  $c = 3000$ , and the full spin Hamiltonian to generate signal decay curves. As in the  $T_{1\rho}$  noise spectroscopy, the signal decay rate is used to reconstruct the noise spectrum shown in red. Substantial deviation between the two is observed in the regime  $\omega_p/(2\pi S(\omega_p)) < 2$ .

### 3.3.3 Perturbation series

The system qubit in the interaction frame subject to the CW irradiation of length  $t$  can be described using a density matrix in the integral form as

$$\tilde{\rho}(t) = \tilde{\rho}(0) - i \int_0^t dt_1 [\tilde{\mathcal{H}}(t_1), \tilde{\rho}(t_1)], \quad (3.19)$$

where we set  $\hbar = 1$  for convenience. By iterating, the perturbative series can be obtained:

$$\begin{aligned} \tilde{\rho}(t) = & \tilde{\rho}(0) - i \int_0^t dt_1 [\tilde{\mathcal{H}}(t_1), \tilde{\rho}(0)] \\ & - \int_0^t dt_1 \int_0^{t_1} dt_2 [\tilde{\mathcal{H}}(t_1), [\tilde{\mathcal{H}}_s(t_2), \tilde{\rho}(0)]] \\ & + i \int_0^t dt_1 \int_0^{t_1} dt_2 \int_0^{t_2} dt_3 [\tilde{\mathcal{H}}(t_1), [\tilde{\mathcal{H}}(t_2), [\tilde{\mathcal{H}}_s(t_3), \tilde{\rho}(0)]]] \dots, \end{aligned} \quad (3.20)$$

where  $\tilde{\rho}(0) = \mathcal{S}_x$  in the  $T_{1\rho}$  experiment. By imposing the condition that  $f(t)$  is Gaussian distributed random variable and  $\langle f(t) \rangle = 0$ , only even order terms in  $f(t)$  contribute to



the signal decay (Isserlis' Gaussian moment theorem). After calculating the commutators using the initial condition and the form of Hamiltonian in Eq. 3.13, the signal decay can be expressed as:

$$\begin{aligned}
& \langle \text{Tr}(\tilde{\rho}(t)\sigma_x) \rangle \\
&= 1 + \sum_{n=1} (-1)^n \int_0^T dt_1 \dots \int_0^{t_{2n-1}} dt_{2n} \langle f(t_1) \dots f(t_{2n}) \rangle \prod_{k=1}^n \cos(\omega_p(t_{2k} - t_{2k-1})) \\
&= 1 + \sum_{n=1} (-1)^n \Omega_n
\end{aligned} \tag{3.21}$$

Above equation can be rewritten by using the Fourier transform of  $f(t)$ . For example, the first order ( $n = 1$ ) term can be written as:

$$\Omega_1 = \int_{-\infty}^{\infty} d\omega_1 \int_{-\infty}^{\infty} d\omega_2 \langle \mathcal{F}(\omega_1)\mathcal{F}(\omega_2) \rangle \int_0^t dt_1 \int_0^{t_1} dt_2 \exp(-i(\omega_1 t_1 + \omega_2 t_2)) \cos(\omega_p(t_2 - t_1)), \tag{3.22}$$

where  $\mathcal{F}$  is the Fourier transform of  $f(t)$  and  $S(\omega)T = \pi\langle |\mathcal{F}(\omega)|^2 \rangle/2$ . Although analytical evaluations are challenging, qualitative analysis shows that the time integral peaks symmetrically or anti-symmetrically around  $\omega_{1,2} = \pm\omega_p$ , and behaves like delta-functions in the  $t \rightarrow \infty$  limit. In the delta-limit where the slope of  $\mathcal{F}(\omega)$  is assumed to be constant over the width of the peaks, only the real components with  $\pm\omega_1 = \mp\omega_2 = \omega_p$  contribute to the signal decay. We studied qualitative behaviour of the time integral for the second order term as well, and observed that in the delta-limit, only the real components with  $\pm\omega_{1,3} = \mp\omega_{2,4} = \omega_p$  and  $\pm\omega_{1,4} = \mp\omega_{2,3} = \omega_p$  contribute to the signal decay. Thus by induction, we can approximate the  $n^{\text{th}}$  order term in the delta-limit as:

$$\Omega_n \approx \alpha_n \langle |\mathcal{F}(\omega_p)|^2 \rangle^n \propto (S(\omega_p)T)^n, \tag{3.23}$$

where  $\alpha_n$  is the normalization constant for the delta-like functions. Using Eq. 3.21 and Eq. 3.23, we deduce that the signal decay in the delta-limit can be expressed as:

$$\langle \mathcal{S}_x(t) \rangle = \langle \mathcal{S}_x(0) \rangle \exp\left(-\sum_{k=0} h_k (S(\omega_p)T)^{k+1}\right), \tag{3.24}$$

To get the feel of how the higher order terms in  $S(\omega)T$  contribute to the signal decay, we again simulate the spin evolution under the full spin Hamiltonian with the input noise function  $S(\omega) = 2\pi c/\omega$ , and fit the signal decay curve to Eq. 3.24 upto  $k = 2$  term, and compare the higher order coefficients  $h_1$  and  $h_2$  to the zeroth order value  $h_0$ . The simulation results are shown in Fig. 3.7. The red and blue colors in the figure represent

$h_1$  and  $h_2$  terms normalized by  $h_0$ , respectively, and the squares and crosses are used to label different noise amplitudes  $c = 30$  and  $c = 3000$ , respectively. The simulation shows that the relative magnitudes of  $h_1$  and  $h_2$  compared to  $h_0$  is consistently smaller than 0.5 over the range of simulated values of  $\omega_p$  and  $S(\omega)$ , except at one outlier point where  $h_1$  is comparable to  $h_0$ . However, at this point, it is not clear how the form of Eq. 3.24 will break down in the violation of  $n \gg 1$  limit.

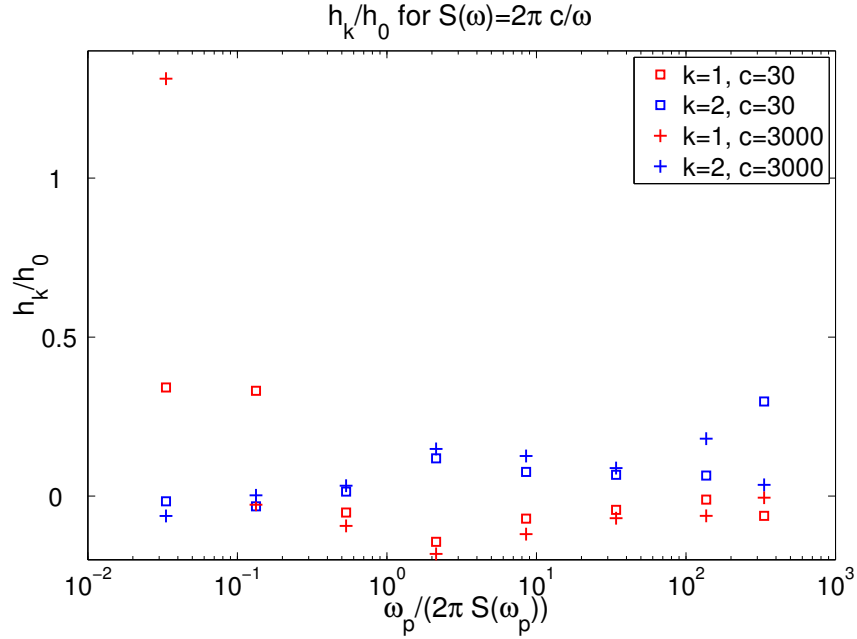


Figure 3.7: Simulated signal decay curve fitting coefficients for higher order terms in  $S(\omega)T$ . The signal decay is simulated using an input noise function  $S(\omega) = 2\pi c/\omega$  where  $c$  is chosen to be 30 (square) and 3000 (cross). The simulated signal decay is fitted to  $\exp(-\sum_{k=0}^2 h_k (S(\omega_p)T)^{k+1})$ , and the plot shows  $h_1/h_0$  (red) and  $h_2/h_0$  (blue).

Another useful perturbation approach is Average Hamiltonian theory (AHT) [63, 88–90]. The system qubit evolves in the interaction frame by the unitary operator

$$\tilde{U}(T) = \mathcal{T} \exp \left( -i \int_0^T \tilde{\mathcal{H}}(t) dt \right), \quad (3.25)$$

where  $\mathcal{T}$  is the Dyson time ordering operator. The Magnus expansion [63, 91] is used to

construct a time-independent effective Hamiltonian [92] such that

$$\tilde{U}(T) = \exp\left(-iT \sum_{k=0}^{\infty} \bar{\mathcal{H}}_k\right). \quad (3.26)$$

The commutators generally do not vanish,  $[\tilde{\mathcal{H}}(t_1), \tilde{\mathcal{H}}(t_2)] \neq 0$ , and thus the higher order Magnus terms will generally be non-zero. The first three AHT terms are given as follows:

$$\bar{\mathcal{H}}_0 T = \int_0^T dt \tilde{\mathcal{H}}(t) \quad (3.27)$$

$$\bar{\mathcal{H}}_1 T = \frac{-i}{2!} \int_0^T dt_1 \int_0^{t_1} dt_2 [\tilde{\mathcal{H}}(t_1), \tilde{\mathcal{H}}(t_2)] \quad (3.28)$$

$$\bar{\mathcal{H}}_2 T = \frac{-1}{3!} \int_0^T dt_1 \int_0^{t_1} dt_2 \int_0^{t_2} dt_3 \left( [\tilde{\mathcal{H}}(t_1), [\tilde{\mathcal{H}}(t_2), \tilde{\mathcal{H}}(t_3)]] + [\tilde{\mathcal{H}}(t_3), [\tilde{\mathcal{H}}(t_2), \tilde{\mathcal{H}}(t_1)]] \right). \quad (3.29)$$

Similar to the perturbation series discussed previously, analytical evaluations of the AHT terms beyond 0<sup>th</sup> order are difficult. In order to make use of the perturbation approaches in the study of  $T_{1\rho}$  noise spectroscopy, we plan to run numerical simulations and compare the spin evolution predicted by the GBE and the higher order perturbation series (both Eq. 3.20 and Eq. 3.26) to examine under what conditions higher order perturbation terms provide more accurate description. We also plan to use the numerical simulations to search for ways to correctly take the higher order terms into account in the construction of  $S(\omega)$ .

### 3.3.4 Experiment

In this section, we describe two NMR noise spectroscopy experiments, one in the solid state and another in the liquid state aimed to answer two different questions. The solid state NMR experiment is designed to probe the spectral density of noise that is due to weak interaction of the environment formed by dipolar-coupled nuclei. In the liquid state NMR, there is no dipolar-coupled spin bath that acts as a source of noise. Also, the single spin Hamiltonian in the liquid state NMR is very simple, and the single qubit control can be done in high precision. Thus the single spin dynamic in the liquid state NMR can be simulated with high accuracy, and makes it an excellent system for testing and developing ideas of the noise spectroscopy to build more robust noise probing protocol.

Both experiments demonstrate good agreement between the  $T_{1\rho}$  and pulsed noise spectroscopy methods, suggesting that the two methods can be combined to provide more complete noise spectrum.

## Solid state experiment

The low frequency noise spectrum is probed for a natural abundance  $^{13}\text{C}$  nucleus corresponding to one of two carboxylic acid groups in single crystal malonic acid. The carboxylic  $^{13}\text{C}$  signal of interest is spectrally distinct from the other two  $^{13}\text{C}$  signals in the chosen crystalline orientation [93]. The fraction of molecules having more than one  $^{13}\text{C}$  is negligible due to low natural abundance. The surrounding protons coupled to the  $^{13}\text{C}$  of interest via the dipolar interaction act as the source of low frequency magnetic noise. We choose one of the  $^{13}\text{COOH}$  nuclei since they experience weaker nearest-neighbor proton couplings than the  $\text{CH}_2$  carbon, better approximating a qubit coupled weakly to a bath. The NMR experiment was carried out at a  $^{13}\text{C}$  Larmor frequency of 75.4678 MHz, with the two off-resonance carbon nuclei at offsets of +3.047 kHz and  $-5.977$  kHz in the chosen crystalline orientation. The on-resonance  $^{13}\text{C}$  had a linewidth  $\pi/T_2^* \approx 175$  Hz with strong proton decoupling on. All experiments began with  $^1\text{H}$ - $^{13}\text{C}$  cross-polarization to initialize the  $^{13}\text{C}$  polarization; the proton  $T_1$  and recycle delay between scans were 30 s and 150 s, respectively. For the noise spectroscopy experiments, a weak proton decoupling field was applied in order to reduce the qubit-bath coupling, but not remove it entirely. The Rabi frequency of the proton decoupling field was  $\approx 20$  kHz, whereas noise spectroscopy measurements were carried out in the range 0.15-10 kHz, so that a peak in the noise spectrum due to proton decoupling would not be present [51]. We first applied the CPMG sequence to perform pulsed noise spectroscopy, choosing the pulse delays as  $\tau_k = k^{-1} \cdot 1280 \mu\text{s}$ , where integer  $1 \leq k \leq 10$  and the number of  $\pi$  pulses in the  $k^{\text{th}}$  sequence is  $8k$ . This gives a noise sampling frequency of  $\omega_k = \pi/\tau_k$ . We used three additional  $\tau = \{3200, 2134, 1600\} \mu\text{s}$  to extend the low frequency end of the noise spectrum. The NMR signal decay rates  $R_k$  are measured and the noise spectrum, shown in blue in 3.8, is obtained by the method given in [51]. The error bars result from the uncertainties in determining decay rates  $R_k$ , primarily due to the experimental signal-to-noise ratio (with signal averaging) of only  $\sim 10 - 20$ . Next, we turn to the  $T_{1\rho}$  method. A CW field of amplitude  $0.15 \text{ kHz} \leq \omega_p/(2\pi) \leq 10$  kHz is applied along the rotating frame x-axis. The NMR signal is acquired after a  $T = 6$  ms irradiation time for all amplitudes and is normalized by a reference signal obtained at  $T = 0$ . The 6 ms pulse length corresponds to a filter function peak width of 0.17 Hz, about 1.6 times broader than the filter function peak width for the CPMG data. The noise spectrum obtained using CW method is shown in red in Fig. 3.8.  $S(\omega)$  follows a roughly a  $\omega^{-1}$  power law in both cases, with fits to the data giving an exponent of  $-0.9 \pm 0.1$  for CPMG and  $-0.8 \pm 0.1$  for CW. A scaling factor 1.6 was applied to the CPMG result to properly account for the fact that  $\int |F(\omega, T)|^2 d\omega$  was 1.6 times larger for the CPMG filter function used here compared to the effective CW filter function. Since the CW decays were only measured at a fixed time  $T$ , the total number of CW experiments was much less than

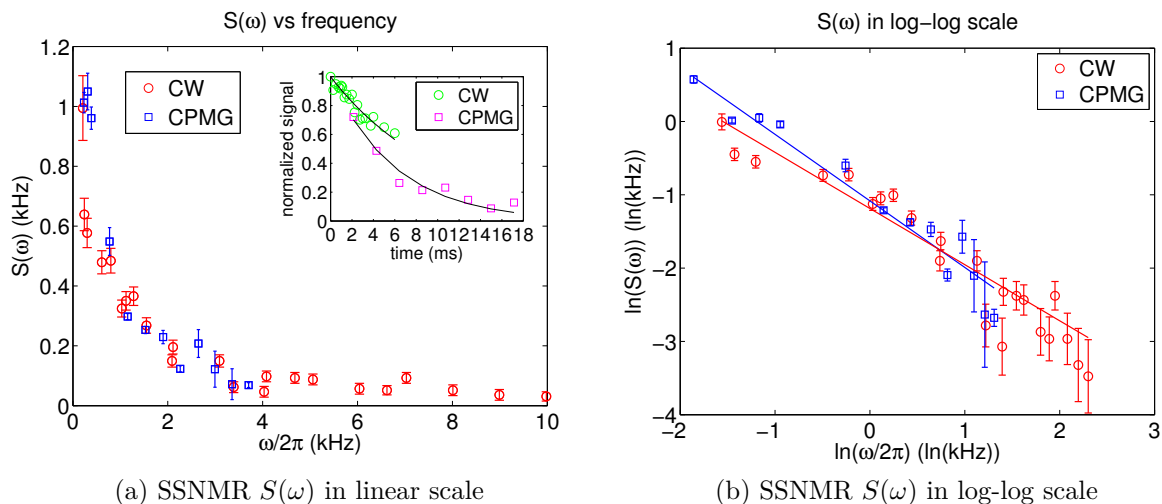


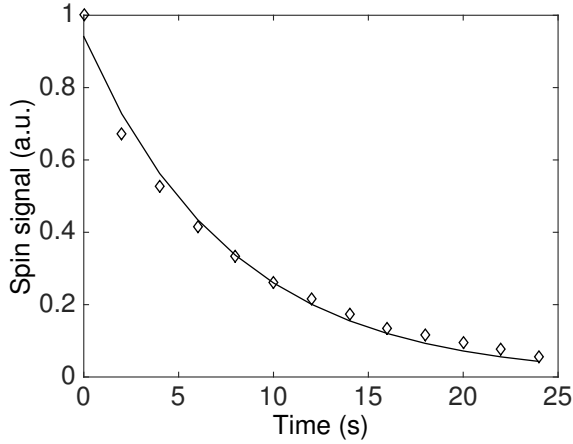
Figure 3.8: (a) Spectral density of low frequency noise  $S(\omega)$  obtained by the CPMG and  $T_{1\rho}$  methods for an ensemble  $^{13}\text{C}$  qubit in single crystal malonic acid. The CW and CPMG results are shown by open circles (red) and open squares (blue), respectively. The inset shows an example of the NMR signal decay versus time for both methods at a noise sampling frequency 1.5 kHz. (b) Log-log plot of the same data shows that  $S(\omega)$  follows a power law decay, with fits yielding  $\omega^{-0.9\pm 0.1}$  and  $\omega^{-0.8\pm 0.1}$  for the CPMG and  $T_{1\rho}$  methods, respectively.

the number of pulsed experiments, yielding larger error bars in the CW data of Fig. 3.8.

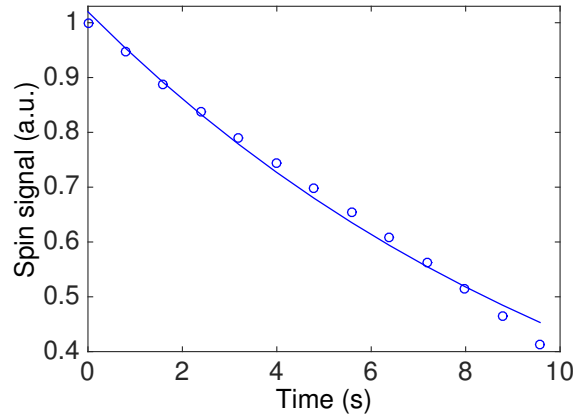
### Liquid state experiment

The single qubit system used in the liquid state NMR is a proton in chloroform ( $\text{CHCl}_3$ ) dissolved in acetone- $\text{d}_6$ .  $T_2$  and  $T_1$  measured for this spin qubit are 9 s and 198 s, respectively. A typical line width obtained after shimming is about 0.7 Hz. Long  $T_1$  compared to  $T_2$ , sharp line width, excellent signal to noise ratio and the ability to generate control pulses with high precision makes this system an excellent test-bed for the ideas of noise spectroscopy for dephasing noise. The liquid state NMR experiment was performed at a proton Larmor frequency of 300.13 MHz.

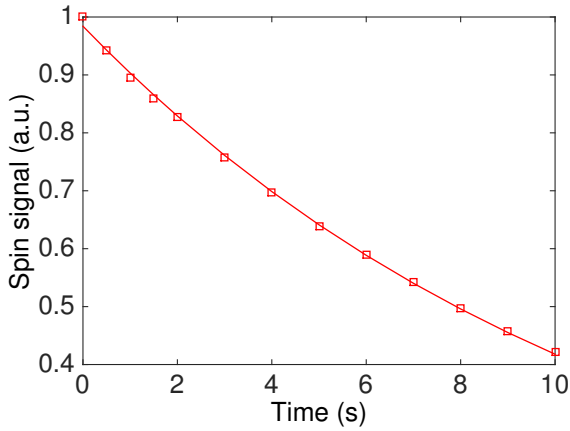
For the pulsed method, we again used CPMG sequence. In both CPMG and  $T_{1\rho}$  noise spectroscopy, we attempted to extend the probing frequency range as broad as possible. For the CPMG experiment, we intuitively guess that the decoupling period  $2\tau$  where  $\tau$  is the



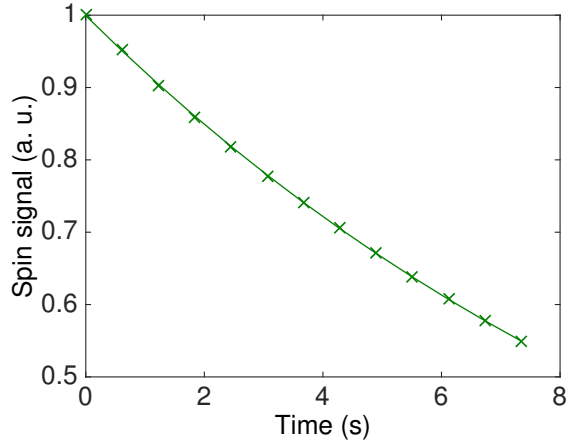
(a) CPMG signal decay 0.25 Hz



(b) CPMG signal decay 1.6 kHz



(c) CPMG signal decay 80 Hz



(d) CPMG signal decay 500 Hz

Figure 3.9: Signal decay curve in the CPMG noise spectroscopy experiment obtained at probing frequency (a) 0.25 Hz (b) 1.6 kHz (c) 80 kHz (d) 500 Hz. The probing frequency  $\omega_p$  is adjusted by choosing the pulse spacing  $\tau$  between  $\pi$  pulses using the relation  $\omega_p = \pi/\tau$ .

time spacing between  $\pi$  pulses should be less than or comparable to  $T_2$ . Since  $\omega_p = \pi/\tau$ , we expect that  $\omega_p$  should be larger than  $2\pi/T_2$ . For the  $T_{1\rho}$  experiment, the condition  $\omega_p T/(2\pi) > 1$  must be satisfied as discussed before, and the CW pulse duration  $T$  should be less than or comparable to  $T_2$ . Hence we impose the condition  $T_2 > T > 2\pi/\omega_p$ , which is equivalent to the condition imposed to the CPMG experiment for the lower end of the

probing frequency. The high-end frequency for the CPMG experiment is limited by the length of  $\pi$  pulses as the CPMG sequence requires the pulse spacing to be much larger than the pulse length. The  $\pi$  pulse length was  $20 \mu\text{s}$ , and we expect the highest probing frequency for reliable noise spectroscopy is about 5 KHz which corresponds to the pulse spacing of an order of magnitude larger than the pulse length.

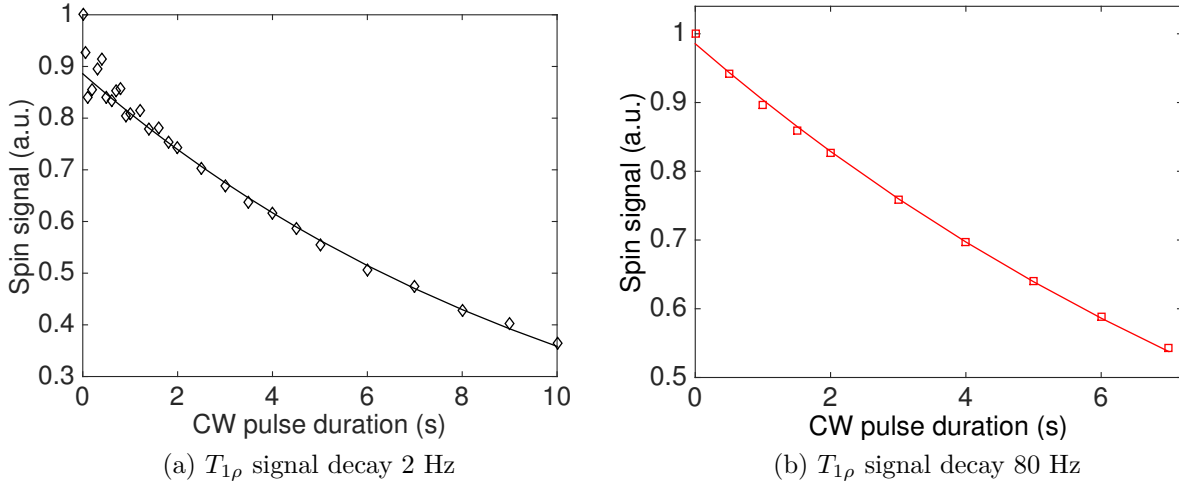


Figure 3.10: Signal decay curve in the  $T_{1\rho}$  noise spectroscopy experiment obtained at probing frequency (a) 2 Hz and (b) 80 Hz. The probing frequency  $\omega_p$  is adjusted by choosing the nutation frequency of the CW pulse.

In the CPMG experiment, the signal decay fits very well to a simple exponential curve in the frequency range between 0.5 Hz to 1 kHz, as the examples in Figs. 3.9c and 3.9d demonstrate. At outside of that frequency window, the decay curve starts to deviate from the exponential fitting. Figs. 3.9a and 3.9b demonstrate such deviations at the frequencies of 0.25 Hz and 1.6 kHz. The results shown in Figs. 3.9a and 3.9b are not too surprising because 0.25 Hz probing frequency corresponds to 2 s pulse spacing which is comparable to  $T_2$ , and finite pulse lengths can start to contribute for 1.6 kHz probing frequency. The spectral density of noise extracted from CPMG decoupling method in the range of 0.25 Hz to 1 kHz is shown in red in Fig. 3.11.  $S(\omega)$  follows roughly a power law decay, with fits to the data giving an exponent of  $-0.044 \pm 0.008$ .

In the  $T_{1\rho}$  experiment, instead of taking the spin signal amplitude at a fixed  $T$  as was in the case for the solid state experiment, we measure the full decay curve using at least 10 time points and fit it to an exponential function in order to extract the decay rate  $R$ .

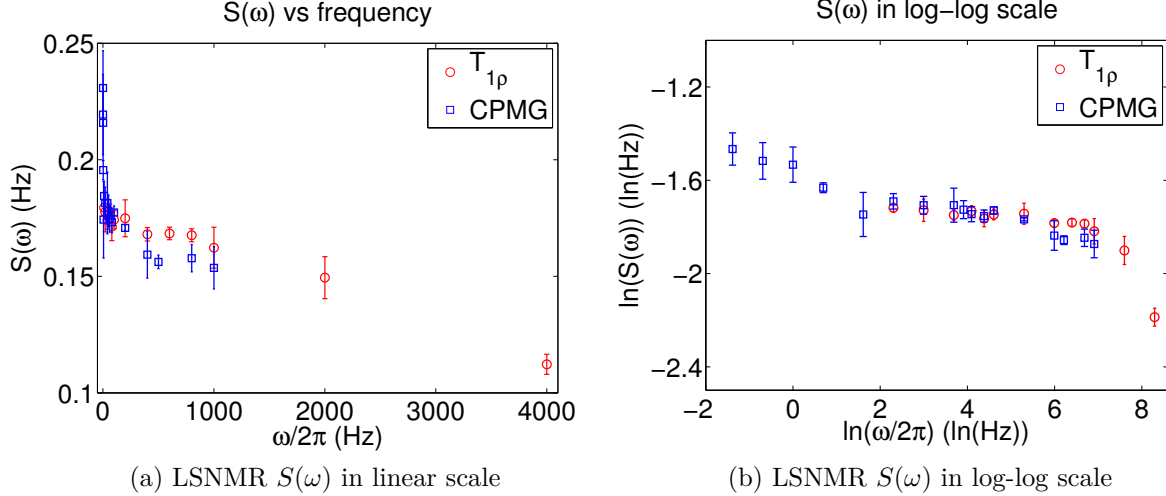


Figure 3.11: (a) Spectral density of low frequency noise  $S(\omega)$  obtained by the CPMG and  $T_{1\rho}$  methods for an ensemble  $^1\text{H}$  qubit in chloroform dissolved in acetone- $\text{d}_6$ . The  $T_{1\rho}$  and CPMG results are shown by open circles (red) and open squares (blue), respectively. (b) Log-log plot of the same data shows that  $S(\omega)$  from the CPMG follows a power law decay, with fits yielding  $\omega^{-0.044 \pm 0.008}$ . For CW data, the power law decay is observed upto roughly 1 kHz, then decay rate increases in the 2-4 kHz range. Fitting the data upto 1 kHz gives  $\omega^{-0.03 \pm 0.01}$ .

Then  $S(\omega_p)$  is simply obtained by  $S(\omega_p) = 2R$  using Eq. 3.17. At low pulse frequency and short pulse duration regime, we observe oscillations in the signal decay as shown in the example case of  $\omega_p = 2$  Hz in Fig. 3.10a. In the frequency window between 10 Hz to 4 kHz, spin signal decay curves fit very well to an exponential function. An example of the decay function in the range demonstrating good fit to the exponential decay is shown in Fig. 3.10b. In principle, the high-end frequency can be extended further. However, we stopped at 4 kHz in order to prevent the sample heating and damaging the probe from high-power CW irradiation. The spectral density of noise extracted from  $T_{1\rho}$  decoupling method in the range of 10 Hz to 4 kHz is shown in red in Fig. 3.11. The log-log plot in Fig. 3.11b shows that  $S(\omega)$  data in  $T_{1\rho}$  experiment matches very well to the data obtained in the CPMG experiment within the error bar upto 1 kHz. Fitting the  $T_{1\rho}$  data upto 1 kHz gives an exponent of  $-0.03 \pm 0.01$ .



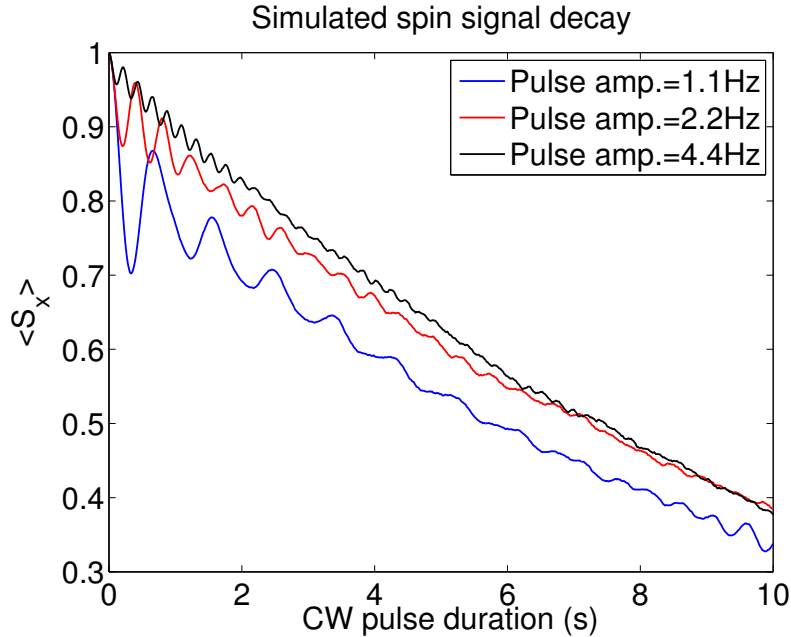


Figure 3.12: Numerical simulation of the spin signal decay to study the effect of inhomogeneous line broadening. The full spin Hamiltonian is simulated with an input noise function that is obtained from the  $T_{1\rho}$  noise spectroscopy experiment. The NMR line width of 0.7 Hz is added in the simulation by averaging the Larmor frequency over the Lorentzian distribution. The simulation reproduces oscillations in the signal decay curve at short pulse durations as observed in the experiment. The oscillation period in the simulation for the 1.1, 2.2 and 4.4 Hz pulse amplitude matches very well to 1, 2, and 4 Hz pulse amplitude experimental data. The small difference in the pulse amplitude can be explained by the uncertainty in the pulse calibration in the experiment.

Numerical simulations of the full spin Hamiltonian including the inhomogeneous line-broadening characterized by  $T_2^*$  is carried out to examine the oscillatory behaviour of the signal decay curve at low frequency regime in the  $T_{1\rho}$  experiment. We used the noise spectrum obtained in the  $T_{1\rho}$  experiment shown in Fig. 3.11 as the input noise in the simulation. In the simulation without  $T_2^*$  noise, the signal decays as a smooth exponential function without noticeable oscillation. However, the oscillation is reproduced as shown in Fig. 3.12 when the Larmor frequency distribution is incorporated in the simulation. The period of the oscillation in the simulated decay curve for the 1.1, 2.2 and 4.4 Hz pulse amplitude matches very closely to the experimental result at 1, 2, and 4 Hz pulse amplitude. The small error in the pulse amplitude can be caused by the uncertainty in the

pulse calibration in the experiment. Therefore, the oscillations at short pulse durations in the low frequency regime can be explained by the effect of  $T_2^*$ .

### 3.3.5 Summary and future work

In this section, we addressed the problem of designing a reliable noise spectroscopy protocol over as wide frequency range as possible. The goal is to be able to quantitatively relate the error in estimating an arbitrary spectral density of dephasing noise  $S(\omega)$  to experimental parameters such as CW pulse amplitude  $\omega_p$  and pulse duration  $T$ , and correct the error as much as possible in order to provide more accurate noise spectrum. For the detailed study, we wish to answer three specific questions: (1) when is delta-approximation valid and what happens when it breaks down; (2) the violation of weak-coupling approximation (effect of the higher order terms in  $S(\omega_p)$ ); and (3) role of inhomogeneous line broadening due to Larmor frequency distribution across the spin ensemble ( $T_2^*$  effect). Our preliminary results from simulations show that given  $1/\omega$  type of noise, the  $T_{1\rho}$  noise spectroscopy underestimates the spectral density of noise when  $\omega_p/(2\pi S(\omega_p)) < 2$ . We have not fully understood how (1) and (2) from above contribute to the underestimation of the noise spectrum. We discussed about our on-going efforts on using perturbation series and numerical simulations as tools to study the effect of higher order terms and the violation of the delta-approximation. By understanding what causes the deviation, one may be able to devise a method to correct and estimate the noise spectrum with better accuracy. The  $T_2^*$  effect produces oscillations in the signal decay function both in the experiment and the simulation in the low CW amplitude regime. Finally, by running the pulsed (CPMG) and  $T_{1\rho}$  noise spectroscopy, we verified that these two methods agree within the experimental error suggesting that the two techniques can be combined to provide noise spectrum over wider frequency range.

# Chapter 4

## Anisotropically coupled electron-nuclear spins for QIP

### 4.1 Introduction

As introduced in 2, nuclear spin qubits in the liquid state are excellent candidates for exploring the ideas of quantum information processing owing to their long coherence times and long history of NMR technology. However, it has lacked the ability to prepare high purity ancilla qubits that are essential for QEC, a crucial step towards scalable quantum information processor. Nuclear spins in the solid state can attain higher polarization at cryogenic temperatures, but then nuclear  $T_1$  relaxation time become undesirably long at these temperatures, making desired quantum state preparation in a timely manner nearly impossible. This naturally leads to incorporating electron spin ensemble since the electron gyromagnetic ratio is much higher than that of nuclei which results in higher thermal equilibrium polarization and faster  $T_1$  relaxation.

In this work, we focus on a solid state spin ensemble system in which a single localized electron interacts with a few nuclear spins at nearby lattice sites. The fundamentals of electron spin resonance (ESR) quantum computing (QC) are analogous to NMR QC, and many of the techniques used for manipulating nuclear spins can also be applied to control unpaired electrons. Coupled electron-nuclear spin systems are more attractive than NMR systems for quantum information processing. As already mentioned, one obvious advantage is that higher gyromagnetic ratio of an electron  $\gamma_e$  (about 660 times greater than that of proton) leads to higher polarization. Also, the anisotropic hyperfine coupling allows indirect control of nuclear spins by irradiating at electron spin transitions, and nuclear

spin gates that are faster than conventional NMR can be realized in certain conditions. Although electron spin-lattice ( $T_1$ ) and spin-spin ( $T_2$ ) relaxation times are much shorter than that of nuclei, the information can be transferred to and stored in the nuclear spin states while computations are done solely through electron spin manipulation and hyperfine interactions [94]. The faster spin-lattice relaxation of the electron can be advantageous in some situations, for example, in heat bath algorithmic cooling (HBAC). HBAC is an efficient method for extracting entropy from a set of system qubits, allowing qubits to be cooled below the bath temperature (i.e. beyond the closed-system, or Shannon, bound). In practice, HBAC requires at least one reset qubit that thermalizes to the bath polarization  $\epsilon_b$  much faster than the relaxation rate of the system qubits. Exploiting the electronic spin-lattice relaxation as a reset operation, the electron can connect a set of nuclear spins to heat bath with an effective temperature much lower than the equilibrium nuclear spin temperature. Another challenge in the ESR QIP is the complexity of microwave control due to more severe bandwidth effects and the difficulty of engineering the ideal propagation of microwave signals, and fast decoherence timescales of the electron spin. In the later chapter, we present our efforts on improving the microwave control that allowed us to manipulate a single-qubit system with above 99% accuracy. However, experimental demonstration of high fidelity coherence control of more complex multi-qubit systems remains challenging.

## 4.2 System model

### 4.2.1 Electron spin resonance: Zeeman interaction

Electron spin resonance arises from the interaction between the electron magnetic dipole moment and an applied magnetic field. Similar to the NMR convention,  $z$ -axis denotes the direction of the static magnetic field, and the electron spin is quantized along  $\mathbf{B}_0 = B_0 \hat{z}$ . The Zeeman Hamiltonian for a free electron spin can be written as  $\mathcal{H}_{ez} = \mu_B \beta_e B_0 \mathcal{S}_z = \mu_B B_0 \mathcal{S}_z$ , where  $g_e$  is the  $g$ -factor of the free electron and  $\mu_B$  is the Bohr magneton.  $\mathcal{S}_i$  is spin-1/2 operator for the electron (recall that the symbol  $\mathcal{I}$  denoted the spin-1/2 operator for nuclei). Note the sign convention for the gyromagnetic ratio of different spin species:  $\gamma_e > 0$  and  $\gamma_n > 0$  except for  $^{15}\text{N}$ .

For the unpaired electron in a single crystal molecule, there is an internal orbital contribution to the magnetic field experienced by the electron. In this case, the electron  $g$ -factor depends on the direction of the applied field. The Zeeman interaction of the unpaired electron in the single crystal is

$$\mathcal{H}_{ez} = \mu_B \mathbf{g}_{\mu\nu} \mathcal{S}_\mu B_\nu, \quad (4.1)$$

where  $\mathbf{g}$  is the second-rank tensor representing the electron g-factor,  $B_\nu$  is an element of the external magnetic field. Here  $\mu, \nu \in \{x, y, z\}$ , and the repeated index implies summation over all the values of the index (similar to the Einstein summation convention, except all indices appear as lower indices). This summation convention will be used only for the terms involving tensor elements. For general summation notation such as summation over the number of nuclei, the symbol  $\sum$  will be used instead.

## 4.2.2 Hyperfine Interaction

The hyperfine interaction between an electron and a nuclear spin is described by the Hamiltonian

$$\mathcal{H}_{hf} = 2\pi\mathbf{A}_{\mu\nu}\mathcal{S}_\mu\mathcal{I}_\nu. \quad (4.2)$$

$\mathbf{A}$  is a second-rank tensor representing the hyperfine interaction. The hyperfine coupling term can be written as the sum of the isotropic (Fermi contact) part:

$$\mathcal{H}_{\text{iso}} = a_{\text{iso}}\mathcal{S}_\mu\mathcal{I}_\mu, \quad (4.3)$$

where  $a_{\text{iso}} \propto \gamma_e\gamma_n|\psi(0)|^2$  and  $|\psi(0)|^2$  is the electron spin density at the nucleus, and anisotropic (dipolar) part:

$$\mathcal{H}_{\text{aniso}} = \mathbf{D}_{\mu\nu}\mathcal{S}_\mu\mathcal{I}_\nu, \quad (4.4)$$

where  $\mathbf{D}_{\mu\nu} \propto \gamma_e\gamma_n \left\langle \psi \left| \frac{3r_\mu r_\nu - \delta_{\mu\nu} r^2}{r^3} \right| \psi \right\rangle$  is the tensor describing the dipolar interaction, and  $|\psi\rangle$  is the ground state wavefunction of the electron, and  $\mathbf{r}$  is the vector connecting the electron and the nuclear spin.

## 4.2.3 Spin Hamiltonian for 1 electron coupled to $N$ nuclei

In 1 electron- $N$  nuclear spin system, the nuclear dipole-dipole interaction is typically two orders of magnitude weaker than the hyperfine coupling strength and can be neglected. Then when the magnetic field  $\mathbf{B}_0$  is applied, the spin Hamiltonian of an unpaired electron spin and  $N$  nuclear spins can be written as

$$\mathcal{H} = \mu_B\mathbf{g}_{\mu\nu}\mathcal{S}_\mu B_\nu + \sum_{k=1}^N -\gamma_n^k(1 + \Delta_{\mu\nu}^k)\mathcal{I}_\mu^k B_\nu + 2\pi\mathbf{A}_{\mu\nu}^k\mathcal{S}_\mu\mathcal{I}_\nu^k, \quad (4.5)$$

where  $\Delta^k$  represents the nuclear chemical shift tensor. Similar summation notation as the one shown before is also used here.  $\mu$  and  $\nu$  run over the tensor elements ( $x, y, z$ ), while  $k$  in the superscript is summed over the number of nuclei.

When the nuclear Zeeman energy and the hyperfine interaction strength are comparable in magnitude and much smaller than the electron Zeeman energy, the spin Hamiltonian can be approximated as [95]:

$$\mathcal{H} \approx \omega_S \mathcal{S}_z + \sum_{k=1}^N -\omega_I^k \mathcal{I}_z^k + 2\pi \left( \mathbf{A}_{zz}^k \mathcal{S}_z \mathcal{I}_z^k + \mathbf{A}_{zx}^k \mathcal{S}_z \mathcal{I}_x^k + \mathbf{A}_{zy}^k \mathcal{S}_z \mathcal{I}_y^k \right). \quad (4.6)$$

Here,  $\omega_S = \mu_B \|\mathbf{g}\| B_0$  is the electron Larmor frequency, and  $\omega_I^k = \gamma_n^k \|(1 + \Delta)\| B_0$  is the Larmor frequency of the  $k^{\text{th}}$  nuclear spin. Without loss of generality, we can define a new x-axis of the nuclear spin subspace by applying a transformation around z-axis by an angle  $\phi = \tan^{-1}(\mathbf{A}_{zy}/\mathbf{A}_{zx})$  such that the nuclear spin lies in the xz-plane of the laboratory frame. In this frame, the Hamiltonian has the form

$$\mathcal{H} = \omega_S \mathcal{S}_z + \sum_{k=1}^N \left( -\omega_I^k \mathcal{I}_z^k + a^k \mathcal{S}_z \mathcal{I}_z^k + b^k \mathcal{S}_z \mathcal{I}_x^k \right), \quad (4.7)$$

where  $a^k = 2\pi \mathbf{A}_{zz}^k$  and  $b^k = 2\pi \sqrt{(\mathbf{A}_{zx}^k)^2 + (\mathbf{A}_{zy}^k)^2}$ .  $\mathcal{H}$  is diagonalized by the unitary transformation  $\mathcal{H}_d = U_d \mathcal{H} U_d^\dagger$ , with the operator

$$U_d = \prod_{k=1}^N \exp(-i(\eta_\uparrow^k \mathcal{S}^\uparrow \mathcal{I}_y^k + \eta_\downarrow^k \mathcal{S}^\downarrow \mathcal{I}_y^k)). \quad (4.8)$$

where  $\eta_\uparrow^k = \arctan\left(\frac{-b^k}{a^k + 2\omega_I^k}\right)$  and  $\eta_\downarrow^k = \arctan\left(\frac{-b^k}{a^k - 2\omega_I^k}\right)$ , and  $\mathbb{1}$  is the unit matrix.  $\mathcal{S}^\uparrow = \mathbb{1}/2 + \mathcal{S}_z$  and  $\mathcal{S}^\downarrow = \mathbb{1}/2 - \mathcal{S}_z$  are projections in the spin-up and spin-down state of the electron, respectively. The nuclear spin is quantized along the direction of an effective field

$$\mathbf{B}_n^k = \left( B_0 \pm \frac{a^k}{2\gamma_n^k} \right) \hat{z} \pm \left( \frac{b^k}{2\gamma_n^k} \right) \hat{x} \quad (4.9)$$

and the  $\pm$  sign depends on whether the electron spin is parallel (spin up) or antiparallel (spin down) to the external field. As a consequence, when  $b \neq 0$ , the direction of the nuclear spin quantization axis is dictated by the electron spin state.  $\eta_\uparrow^k$  and  $\eta_\downarrow^k$  define the directions of the nuclear quantization axes with respect to  $\mathbf{B}_0$  in the electron spin-up and spin-down manifolds, respectively. Also, when  $b = 0$ , the external microwave control pulse applied at the electron resonance frequency can only induce single spin flip of the electron. The single spin transition is usually called allowed transition. The electron-nuclear double spin flip is usually called forbidden transition. However, when  $b \neq 0$ , the

microwave control pulse combined with the anisotropic part of the hyperfine coupling can drive the forbidden transition with non-zero probability. Exploiting anisotropic hyperfine interaction for controlling the nuclear spin will be explained in more detail in Sec. 4.4.1.

In the diagonal basis, the Hamiltonian is written as

$$\mathcal{H}_d = \omega_S \mathcal{S}_z + \sum_{k=1}^N \left( \omega_{12}^k \mathcal{S}^\uparrow \mathcal{I}_z^k + \omega_{34}^k \mathcal{S}^\downarrow \mathcal{I}_z^k \right) = \omega_s \mathcal{S}_z + \sum_{k=1}^N \left( \frac{\omega_+^k}{2} \mathcal{I}_z^k + \frac{\omega_-^k}{2} 2\mathcal{S}_z \mathcal{I}_z^k \right), \quad (4.10)$$

with nuclear frequencies

$$\omega_{12}^k = \left( \omega_I^k + \frac{a^k}{2} \right) \cos(\eta_\uparrow^k) - \frac{b^k}{2} \sin(\eta_\downarrow^k), \quad \omega_{34}^k = \left( \omega_I^k - \frac{a^k}{2} \right) \cos(\eta_\uparrow^k) + \frac{b^k}{2} \sin(\eta_\downarrow^k) \quad (4.11)$$

and  $\omega_+^k = \omega_{12}^k + \omega_{34}^k$  and  $\omega_-^k = \omega_{12}^k - \omega_{34}^k$ . The eigenstates of the  $k^{\text{th}}$  nuclear spin are a mixture of the nuclear Zeeman eigenstates as following:

$$|\uparrow_0^k\rangle = \cos\left(\frac{\eta_\uparrow^k}{2}\right) |\uparrow\rangle - \sin\left(\frac{\eta_\uparrow^k}{2}\right) |\downarrow\rangle, \quad (4.12)$$

$$|\uparrow_1^k\rangle = \sin\left(\frac{\eta_\uparrow^k}{2}\right) |\uparrow\rangle + \cos\left(\frac{\eta_\uparrow^k}{2}\right) |\downarrow\rangle, \quad (4.13)$$

$$|\downarrow_0^k\rangle = \cos\left(\frac{\eta_\downarrow^k}{2}\right) |\uparrow\rangle - \sin\left(\frac{\eta_\downarrow^k}{2}\right) |\downarrow\rangle, \quad (4.14)$$

$$|\downarrow_1^k\rangle = \sin\left(\frac{\eta_\downarrow^k}{2}\right) |\uparrow\rangle + \cos\left(\frac{\eta_\downarrow^k}{2}\right) |\downarrow\rangle. \quad (4.15)$$

The subscript 0 and 1 indicate that electron spin is either in the spin-up or spin-down state.

### 4.3 System characterization: Hamiltonian determination

The spin Hamiltonian of the electron-nuclear coupled system is characterized by the hyperfine coupling parameters  $a$  and  $b$  in the lab frame (Eq. 4.7) or equivalently by the nuclear frequencies  $\omega_{12}$  and  $\omega_{34}$  in the diagonal basis (Eq. 4.11).

The first step towards high fidelity control of the hyperfine coupled electron-nuclear spin system is to precisely determine  $g$ - and hyperfine tensors. Given the tensors, one can





### 4.3.1 Electron g-tensor and hyperfine interaction tensor characterization

First, we explain the  $g$ -tensor determination procedure. For a static magnetic field  $\mathbf{B}_0 = B_0(l_x, l_y, l_z)$  where  $l_x, l_y$  and  $l_z$  are direction cosines of the magnetic field in the axes of the crystal satisfying  $l_x^2 + l_y^2 + l_z^2 = 1$ , the electron Zeeman energy levels can be rewritten as

$$E_{\pm} = \pm \frac{1}{2} \mu_B B_0 (l_{\alpha} \Gamma_{\alpha\beta} l_{\beta})^{1/2}, \quad (4.16)$$

where we introduce  $\Gamma = \mathbf{g} \cdot \mathbf{g}$ . In the absence of nuclear spins, the magnetic resonance condition  $\Delta E = h\nu = \mu_B g B_0$  leads to

$$g = \frac{h\nu}{\mu_B B_0} = \frac{\Delta E}{\mu_B B_0} = \frac{E_+ - E_-}{\mu_B B_0} = (l_{\alpha} \Gamma_{\alpha\beta} l_{\beta})^{1/2}, \quad (4.17)$$

where  $g$  is the experimentally observed value,  $\Delta E$  is the difference between  $E_+$  and  $E_-$ , and  $\nu$  is the frequency of the microwave field. For  $\mathbf{B}_0 = B_0(\cos \theta, \sin \theta, 0)$ , using the symmetry  $\Gamma_{\alpha\beta} = \Gamma_{\beta\alpha}$ , the dependence of  $g$  on  $\theta$  can be written as

$$(g(\theta))^2 = l_{\alpha} \Gamma_{\alpha\beta} l_{\beta} = \Gamma_{xx} \cos^2 \theta + \Gamma_{yy} \sin^2 \theta + 2\Gamma_{xy} \cos \theta \sin \theta. \quad (4.18)$$

By measuring  $g(\theta)$  at various  $\theta$  and solving Eq. 4.18,  $\Gamma_{xx}$ ,  $\Gamma_{yy}$  and  $\Gamma_{xy}$  can be determined. Similarly, by orienting  $\mathbf{B}_0$  within the  $x$ - $z$  and  $y$ - $z$  planes and measuring  $g(\theta)$  for various  $\theta$  (where  $\theta$  is the angle between  $\mathbf{B}_0$  and  $z$ , or between  $\mathbf{B}_0$  and  $y$ ),  $\Gamma_{zz}$ ,  $\Gamma_{xz}$  and  $\Gamma_{yz}$  can be determined. Therefore full knowledge of  $\Gamma$  can be obtained.

Now we consider the electron-nuclear coupled spin Hamiltonian which contains  $\mathcal{H}_e$ ,  $\mathcal{H}_{hf}$  and  $\mathcal{H}_n$ . In this case, the 1st order approximation of the energy levels of the system gives

$$E_{M_S M_I} = g \mu_B B_0 M_S + \sum_{n=1}^K \left\{ \frac{4\pi^2}{g^2} (l_{\alpha} \Gamma^{\mathbf{A}^n}_{\alpha\beta} l_{\beta}) + \frac{\gamma_n^2 B_0^2}{M_S^2} - \frac{4\pi}{g M_S} \gamma_n B_0 (l_{\alpha} (\mathbf{g} \cdot \mathbf{A}^n)_{\alpha\beta} l_{\beta}) \right\}^{1/2} M_I^n M_S, \quad (4.19)$$

where  $\Gamma^{\mathbf{A}} = \mathbf{g} \cdot \mathbf{A} \cdot \mathbf{A} \cdot \mathbf{g}$ , and  $M_S$  and  $M_I^n$  are quantum numbers for the electron spin and the  $n^{\text{th}}$  nuclear spin, respectively. As mentioned before, all ESR transitions can be classified into two types: allowed and forbidden transitions. Allowed transitions refer to an electron-only spin flips, while forbidden transitions refer to the flips of electron spin along with one or more nuclear spins. In the absence of anisotropic hyperfine coupling, i.e.  $b^n = 0$ , forbidden transitions are completely suppressed and produce no observable ESR signal. When  $b^n \neq 0$ , these transitions can lead to signals comparable to, but typically

smaller than, the allowed transitions. For the purpose of hyperfine tensor determination, it suffices to track only allowed ESR transitions. [96] argues that nuclear Zeeman energy is generally much smaller than hyperfine coupling strength and can be usually omitted in the traditional process of determining hyperfine tensors using ESR spectra. After omitting the nuclear Zeeman energy, the ESR allowed transition energy gap in the 1 electron-1 nucleus system is

$$\Delta E = g\mu_B B_0 + \frac{2\pi}{g}(l_\alpha \Gamma^A_{\alpha\beta} l_\beta)^{1/2} M_I, \quad (4.20)$$

where the nuclear spin quantum numbers  $M_I = \pm 1/2$  represent spin up and spin down states, respectively. The ESR spectrum then splits into two distinct peaks separated by a frequency  $A = g^{-1}(l_\alpha \Gamma^A_{\alpha\beta} l_\beta)^{1/2}$ . Similar to Eq. (4.18), when the static magnetic field is  $\mathbf{B}_0 = B_0(\cos \theta, \sin \theta, 0)$  we have

$$(g(\theta)A(\theta))^2 = \Gamma^A_{xx} \cos^2 \theta + \Gamma^A_{yy} \sin^2 \theta + 2\Gamma^A_{xy} \cos \theta \sin \theta, \quad (4.21)$$

and, as before, expressions for  $\mathbf{B}_0$  in the  $x$ - $z$  and  $y$ - $z$  planes relate the other tensor components of  $\Gamma^A$  to  $(gA)^2$ . In our Hamiltonian determination work, after the procedure

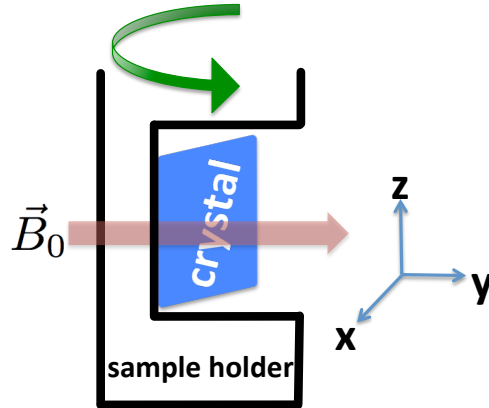


Figure 4.2: Schematic of the crystal mounted on a sample holder for the orientation study. Axes  $x$ ,  $y$  and  $z$  indicate the lab frame in which measurements are taken. The curved green arrow indicates rotation of the crystal for orientation studies.

presented in [96] as explained above, we implemented an optimization process which takes the nuclear Zeeman energy into consideration. The optimization procedure provides more accurate hyperfine tensors especially when the nuclear Zeeman energy is comparable to

the hyperfine coupling. As discussed previously, we need only to detect the spectral positions of the allowed transitions, which can be distinguished from forbidden transition peaks because of their larger intensities. Each measured ESR spectrum is fitted to a set of allowed transition peaks defined by their amplitude, frequency and a common line width. The nuclear Zeeman term is also included as the peak positions are calculated. The peak positions for all measurements in one plane give a set of trajectories for that plane, from which we obtained the dependence of  $\mathbf{g}$  and  $\mathbf{A}^n$  on  $\theta$ . Doing this in three orthogonal planes allows extraction of the  $g$ -factor tensor  $\mathbf{g}$  and hyperfine tensors  $\mathbf{A}^n$  by solving Eqs. (4.18) and (4.21). After this, we used the method of least square fitting to optimize  $\mathbf{g}$  and  $\mathbf{A}^n$  by minimizing the difference between the experimental peak trajectories and the simulated trajectories.

Another method to determine hyperfine tensors is to make use of ENDOR experiments. For ENDOR transitions that correspond to  $\Delta M_S = 0$  and  $\Delta M_I = \pm 1$ , the energy gap in the 1 electron-1 nucleus system can also be readily obtained from Eq. (4.19) and its square is given by

$$\Delta E^2 = \gamma_n^2 B_0^2 + \frac{4\pi^2 M_S^2}{g^2} (l_\alpha \Gamma_{\alpha\beta}^A l_\beta) - \frac{4\pi M_S \gamma_n B_0}{g} (l_\alpha (\mathbf{g} \cdot \mathbf{A})_{\alpha\beta} l_\beta). \quad (4.22)$$

Since  $M_S = \pm 1/2$ , ENDOR spectral peaks also split into two. Denoting observed ENDOR frequencies as  $\nu_\pm$  for  $M_S = \pm 1/2$ , Eq. (4.22) can be rewritten as

$$\nu_\pm^2 = \nu_I^2 + \frac{1}{4g^2} (l_\alpha \Gamma_{\alpha\beta}^A l_\beta) \mp \frac{\nu_I}{g} (l_\alpha (\mathbf{g} \cdot \mathbf{A})_{\alpha\beta} l_\beta), \quad (4.23)$$

where  $\nu_I = \gamma_n B_0 / 2\pi$ . An equation similar to Eqs. 4.18 and 4.21 can be obtained when the static magnetic field is  $\mathbf{B}_0 = B_0(\cos \theta, \sin \theta, 0)$ :

$$\frac{g}{2\nu_I} (\nu_-^2 - \nu_+^2) = (\mathbf{g} \cdot \mathbf{A})_{xx} \cos^2 \theta + (\mathbf{g} \cdot \mathbf{A})_{yy} \sin^2 \theta + 2(\mathbf{g} \cdot \mathbf{A})_{xy} \cos \theta \sin \theta. \quad (4.24)$$

Then the magnitude of  $\mathbf{A}$  can be extracted by measuring the orientation dependence of  $g(\nu_-^2 - \nu_+^2)/2\nu_I$  in three distinct rotation planes.

### 4.3.2 Hamiltonian determination at a fixed crystal orientation

ESEEM or pulsed ENDOR can be employed to measure the magnitudes  $|\omega_{12}|$ ,  $|\omega_{34}|$ ,  $|\omega_+|$ , and  $|\omega_-|$  at a fixed crystal orientation. From these values, the magnitudes of the hyperfine coupling constants  $a$  and  $b$  in Eq. 4.7 can also be calculated. For experimentally determined

values of  $g$ ,  $A$ , and the orientation of the crystal with respect to the static field, these spectroscopic techniques serve as useful tools for validating the Hamiltonian parameters. Notice from Eq. 4.11 that the nuclear frequencies are invariant under the sign change of  $b$  since  $\cos(\arctan(x))$  and  $x \sin(\arctan(x))$  are even functions with respect to  $x$ . Thus the sign of  $b$  is irrelevant for the high fidelity control. Here we briefly review ESEEM and pulsed ENDOR by using 1 electron and 1 nuclear coupled spins as an example. For further details, [95] is an excellent reference.

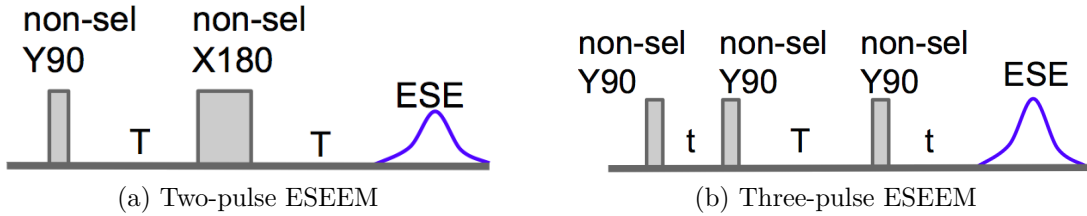


Figure 4.3: (a) Pulse sequence for two-pulse ESEEM. Non-selective  $\pi/2$  and  $\pi$  pulse (denoted non-sel in the figure) separated by time  $T$  produces a spin echo (denoted ESE in the figure) at time  $T$  after the  $\pi$  pulse. The echo is modulated as a function of  $T$ . (b) Pulse sequence for three-pulse ESEEM. In this pulse sequence, the spin echo produced after three non-selective  $\pi/2$  pulses is modulated as a function of  $T$  while  $t$  is fixed.

In previous sections, we have seen that a microwave pulse can generate coherences on both allowed and forbidden electron spin transitions when the anisotropic part of the hyperfine interaction is non-zero. Here we denote the transition between eigenstates  $k$  and  $l$  as  $(k,l)$ . Due to the anisotropy in the hyperfine coupling, a  $\pi/2$  microwave pulse can excite allowed transitions  $(1,3)$  and  $(2,4)$ , and forbidden transitions  $(1,4)$  and  $(2,3)$  in the 1 electron-1 nuclear spin system (see Fig. 4.1b) as long as the pulse has a wide enough frequency bandwidth to excite all transitions (i.e. non-selective). From Eq. 4.35, one can see that the non-selective  $\pi$  pulse transfers the coherence, for example, on  $(1,3)$  transition to coherence on all transitions  $(1,3)$ ,  $(2,3)$ ,  $(1,4)$  and  $(2,4)$ . Then at time  $T$  after the  $\pi$  pulse, each coherence  $(k,l)$  gains a phase  $(\omega_{kl} - \omega_{13})T$ . The time dependent phase appears as a modulation in the spin echo as a function of  $T$ , and the modulation frequency corresponds to nuclear frequencies and their sum and difference. The behaviour of the other coherences at the incident of the  $\pi$  pulse and after is analogous. The pulse sequence for two-pulse ESEEM is shown in Fig 4.3a. A sequence of three non-selective  $\pi/2$  pulses separated by certain time delays can also be used for observing the modulation of the spin echo as a function of  $T$  (Fig. 4.3b). The advantage of the three-pulse ESEEM is that the spin echo is modulated only by the nuclear frequencies unlike the two-pulse technique in which the sum and difference of the nuclear frequencies also contribute to the modulation.

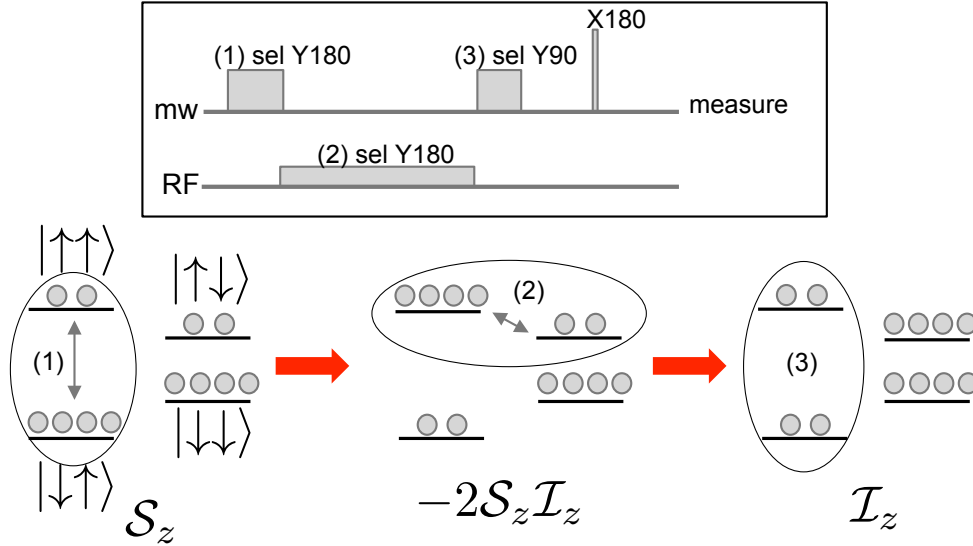


Figure 4.4: Schematics illustrating the idea of pulsed ENDOR. A selective  $\pi$  pulse on the electron spin flip transition denoted as (1) in the figure exchanges the populations of the selected states. In the next step, a selective RF pulse denoted (2) in the figure is applied with some frequency. If the RF pulse frequency is on-resonance with one of the nuclear transition frequencies, the electron and nuclear polarizations are swapped and no electron spin echo can be detected in step (3). In the pulsed ENDOR experiment, the RF frequency is varied and the nuclear frequencies coincide with the pulse frequencies at which the electron spin echo vanishes.

Pulsed ENDOR can be employed to measure nuclear spin frequencies even in the absence of the anisotropic hyperfine coupling. The pulsed ENDOR technique for 1 electron and 1 nuclear coupled spins as an example can be explained using Fig. 4.4. For brevity, here we assume the initial state can be written as  $\mathcal{S}_z$ , meaning that the nuclear polarization is negligible. First, a selective microwave  $\pi$  pulse is applied to one of the ESR allowed transitions, for example, to drive the transition  $|\uparrow\uparrow\rangle \leftrightarrow |\downarrow\uparrow\rangle$  where the first state is for the electron. In the product operator form, the selective pulse transforms  $\mathcal{S}_z$  to  $-2\mathcal{S}_z\mathcal{I}_z$ . Next, a selective RF  $\pi$  pulse is applied, for example, to the  $|\uparrow\uparrow\rangle \leftrightarrow |\uparrow\downarrow\rangle$  transition. When the RF pulse frequency is on-resonance with the nuclear frequency, the populations of the two states  $|\uparrow\uparrow\rangle$  and  $|\uparrow\downarrow\rangle$  are exchanged. At this stage the density matrix is given as  $\mathcal{I}_z$ . Since the electron polarization is swapped with that of the nuclear spin, the electron spin echo can not be detected. On the other hand, if the RF pulse is off-resonance from the nuclear frequency, the pulse induces some rotation of an angle smaller than  $\pi$ , meaning that the

nuclear transition occurs with less probability. Then only part of the electron polarization is transferred to the nuclear spin, and the amount of polarization remaining on the electron transition and thus the electron spin echo intensity varies as a function of the RF frequency. Therefore, in the pulsed ENDOR experiment, the nuclear frequencies can be found by sweeping the RF pulse frequency over some range and looking for the frequencies at which the electron spin echo vanishes.

## 4.4 Closed system control

Given the density matrix  $\rho(t)$  that describes the state of a closed quantum system, the time evolution of the system can be described by the differential Schrödinger equation:

$$\dot{\rho}(t) = \frac{-i}{\hbar} [\mathcal{H}_0 + \mathcal{H}_c(t), \rho(t)], \quad (4.25)$$

where  $\mathcal{H}_0$  is a time-independent natural Hamiltonian and  $\mathcal{H}_c$  is the time-dependent control Hamiltonian.  $[\square, \square]$  denotes commutator (and  $\{\square, \square\}$  is anti-commutator). Provided the initial condition  $\rho(0)$ , the differential equation can be integrated and the final state at time  $\tau$  is:

$$\rho(\tau) = U(\tau)\rho(0)U(\tau)^\dagger. \quad (4.26)$$

The unitary propagator  $U$  is defined as

$$U(\tau) = \mathcal{T} \exp \left( \frac{-i}{\hbar} \int_0^\tau dt (\mathcal{H}_0 + \mathcal{H}_c(t)) \right), \quad (4.27)$$

where  $\mathcal{T}$  is the Dyson time ordering operator specifying the order of the non-commutivity of  $\mathcal{H}$  at different times. In NMR and ESR QC, the external control Hamiltonian is established by applying an oscillating pulse transverse to the direction of the static magnetic field. For the system of  $N$  spin qubits, the control Hamiltonian in the lab frame can be written as a sum of all available control knobs:

$$\mathcal{H}_c(t) = \sum_k^N \frac{\omega_k(t)}{2} \left( \cos(\Omega_k t + \phi_k(t)) \sigma_x^k + \sin(\Omega_k t + \phi_k(t)) \sigma_y^k \right) \quad (4.28)$$

$$= \sum_k^N \sum_{i \in \{x, y\}} u_k^i \sigma_i^k, \quad (4.29)$$

where  $u_k^i$  denotes the control field with the amplitude  $\omega_k(t)$  and the phase  $\phi_k(t)$  applied at a transmitter frequency  $\Omega_k$ .

There are two streams for achieving universal control in the electron-nuclear coupled system. First method is irradiating oscillating magnetic fields resonant with certain spin transition frequency to explore the full Hilbert space. This includes both electron and nuclear spin transitions, much like the electron-nuclear double resonance (ENDOR) spectroscopic technique [95]. The addressability of single qubits, combined with two body interaction Hamiltonian, is sufficient for universal control. Second method is to use anisotropy of the hyperfine interaction and manipulate nuclear spins solely by irradiating microwave control field at electron spin transitions. Hereinafter, we call the latter approach Anisotropic Hyperfine Control (AHC). The control universality via anisotropic hyperfine interaction was proved in [31], and demonstrated experimentally in [32] for a single nuclear spin qubit gate and in [97] for a gate involving two nuclear spin qubits. The advantage of the indirect control technique is that it simplifies the instrumentation as additional rf excitations are not needed, and faster gate implementation relative to ENDOR can be achieved when the hyperfine coupling strength exceeds the Larmor frequency of the nucleus in a given external field. In the following section, we use 1 electron, 1 nuclear spin system as an example to illustrate the idea.

#### 4.4.1 Universal control via anisotropic hyperfine interaction

Consider 1 electron and 1 nuclear spins that are hyperfine-coupled as an example. The eigenstates of this system are:

$$|1\rangle = |\uparrow\rangle \otimes \left( \cos\left(\frac{\eta_\uparrow}{2}\right) |\uparrow\rangle - \sin\left(\frac{\eta_\uparrow}{2}\right) |\downarrow\rangle \right), \quad (4.30)$$

$$|2\rangle = |\uparrow\rangle \otimes \left( \sin\left(\frac{\eta_\uparrow}{2}\right) |\uparrow\rangle + \cos\left(\frac{\eta_\uparrow}{2}\right) |\downarrow\rangle \right), \quad (4.31)$$

$$|3\rangle = |\downarrow\rangle \otimes \left( \cos\left(\frac{\eta_\downarrow}{2}\right) |\uparrow\rangle - \sin\left(\frac{\eta_\downarrow}{2}\right) |\downarrow\rangle \right), \quad (4.32)$$

$$|4\rangle = |\downarrow\rangle \otimes \left( \sin\left(\frac{\eta_\downarrow}{2}\right) |\uparrow\rangle + \cos\left(\frac{\eta_\downarrow}{2}\right) |\downarrow\rangle \right), \quad (4.33)$$

where the first state is for the electron. The electron spin control Hamiltonian in the rotating frame is

$$\mathcal{H}_c(t) = \omega(t) (\cos(\phi(t)) \mathcal{S}_x + \sin(\phi(t)) \mathcal{S}_y), \quad (4.34)$$

where  $\omega$  and  $\phi$  represent the microwave amplitude and phase, respectively. Without loss of generality, we set  $\omega = \text{constant}$ , and  $\phi = 0$ . In the eigenbasis of the internal Hamiltonian,

the rotating-frame control Hamiltonian becomes:

$$\tilde{\mathcal{H}}_c = \frac{\omega}{2} \begin{bmatrix} 0 & 0 & \cos(\eta) & -\sin(\eta) \\ 0 & 0 & \sin(\eta) & \cos(\eta) \\ \cos(\eta) & \sin(\eta) & 0 & 0 \\ -\sin(\eta) & \cos(\eta) & 0 & 0 \end{bmatrix}, \quad (4.35)$$

where  $\eta = (\eta_\uparrow - \eta_\downarrow)/2$ . From Eq. 4.35, one can see that the control Hamiltonian is able to induce all transitions between any eigenstates of the electron spin up manifold and the electron spin down manifold provided  $\eta \neq n\pi/2$  where  $n$  is an integer and eigenstates are non-degenerate. The energy level connectivity can be represented as a graph, and the complete connectivity of the graph generated by the control Hamiltonian and non-degenerate energy levels guarantee universal control of the system [32, 98, 99]. Since the spin Hamiltonian does not consider nuclear-nuclear dipolar interactions, the idea presented for 1 electron, 1 nuclear spin system can be easily extended to larger number of nuclear spins, provided that suitable and distinct hyperfine couplings exist.

#### 4.4.2 Pulse design

The goal of pulse design is to find the control parameters that realize a desired unitary propagator  $U_d$  at some time  $T$  when combined with the natural Hamiltonian  $\mathcal{H}_0$ . Pulse engineering techniques must minimize the effect of relaxation and experimental limitations for practical applications. The experimental limitations include qubit selectivity due to finite frequency bandwidth, time-independent incoherent errors such as static and RF field inhomogeneities, miscalibration of pulse power or duration and frequency offset. Over the last 30 years, numerous multi-pulse techniques have been developed for control in NMR QIP. Traditionally, average Hamiltonian theory has been a powerful tool that provides intuitive guidelines for constructing pulse sequences for simple cases [88]. In particular, composite pulses [100], adiabatic pulses [101–104] and shaped pulses [105] were introduced during the earlier development of NMR QIP to obtain selective operations by using low pulse power and to better compensate for static and rf field inhomogeneities by increasing the number of degrees of freedom in the pulse shape. However, the long pulse times required by these techniques lead to greater decoherence and relaxation effects, and interference of selective pulses simultaneously applied to different spins causes significant deviation from desired operations [106].

Another pulse design method that aims to reduce decoherence effects is to constantly modulate the system's dynamics with high-power control fields to generate the desired



unitary propagator [106]. A common strategy to the problem is to first discretize the total evolution time  $T$  in  $M$  equal steps of duration  $\Delta t = T/M$  in some rotating frame such that in each step the control parameters are approximately constant. The approximation is valid if  $\Delta t \ll 1/\|\mathcal{H}_j\|$ , where  $\mathcal{H}_j$  is the time-independent total Hamiltonian in the rotating frame during the time step  $j$  with a control set  $\{\omega_k^j, \phi_k^j\}$ . Then the total unitary evolution of length  $T$  can be approximated as the product of the propagators for each period,

$$U(T) \approx \prod_j U_j, \quad (4.36)$$

where  $U_j = \exp(-i\Delta t \mathcal{H}_j)$  is the unitary propagator of time step  $j$ . Using above approach, the pulse design problem can be formulated as an optimization problem that is to maximize a fitness function  $\Phi(U(T), U_d) = |\text{Tr}(U(T)^\dagger U_d)|^2/D^2$  over the feasible parameters  $\{\omega_k^j, \phi_k^j\}$ , where  $D$  is the size of the Hilbert space. For more than two qubits, the analytical approach to the optimization problem becomes intractable, and numerical methods are required. For larger systems, the majority of optimal control methods are based on a gradient approach, such as the Gradient Ascent Pulse Engineering (GRAPE) algorithm [72]. The GRAPE algorithm can be briefly summarized as follows. It begins with an initial guess for a set of control parameters  $u_k(j) = \{\omega_k^j \cos(\phi_k^j), \omega_k^j \sin(\phi_k^j)\}$  for all time step  $j \leq M$  and for all spin  $k \leq N$  that are being manipulated. Then in each iteration, the algorithm calculates  $\delta\Phi/\delta u_k^i(j)$ :

$$\frac{\delta\Phi}{\delta u_k^i(j)} = \frac{1}{M^2} \left[ \text{Tr} \left( U_{goal}^\dagger U_N \dots U_{j+1} \frac{\delta U_j}{\delta u_k^i(j)} U_{j-1} \dots U_1 \right) + c.c \right]. \quad (4.37)$$

To first order, the derivative of  $j^{\text{th}}$  step unitary propagator with respect to the control fields is calculated as

$$\frac{\delta U_j}{\delta u_k^i(j)} \approx -i\Delta t \sigma_i^k U_j, \quad (4.38)$$

which is valid as long as the discrete time step is chosen to be significantly smaller than the inverse magnitude of the system Hamiltonian, i.e.  $\Delta t \ll 1/\|\mathcal{H}_j\|$ . For the gradient calculation, the GRAPE algorithm requires calculating the matrix exponential only once for each time step and storing it in the memory, and uses a few matrix multiplications. This is computationally much less costly compared to a brute force approach which requires the simulation of the entire dynamic for the change of control parameter in a single time step. Once the derivative of the fidelity function with respect to the control parameters are calculated, the algorithm updates  $u_k^i(j)$  as

$$u_k^i(j) \rightarrow u_k^i(j) + \epsilon \frac{\delta\Phi}{\delta u_k^i(j)}, \quad (4.39)$$

where  $\epsilon$  is an adjustable step size. The iteration continues until the improvement in the performance index  $\Phi$  is smaller than a chosen threshold value. The GRAPE algorithm can also design pulses robust to experimental imperfections such as static field and rf inhomogeneities and miscalibration if the parameters are sampled over a range of discrete values determined by the distribution. Then the total fidelity to be optimized can be measured as  $\Phi_{tot} = \sum_{\alpha} \Phi(x_{\alpha})$ , where  $x_{\alpha}$  is a particular value of some parameter seen by a fraction of spins. However, just as with any optimal control method, the GRAPE algorithm cannot deterministically locate global minima but instead finds local minima in the search space. Therefore the ultimate fidelities that can be achieved are limited by the initial guess, even if unit fidelity pulses are possible in principle.

## 4.5 Decoherence model

The dynamic of a quantum system described in Sec. 4.4 is formulated assuming that the qubit is perfectly isolated from the environment. However, in physical implementations of QIP, qubits of interest undergo unwanted interactions with environment and eventually lose quantum coherence. In this section, we briefly review the representations of open quantum system dynamics that are useful in designing and simulating the experiment as a necessary step towards realizing complex quantum algorithms.

### 4.5.1 Kraus representation

A general dynamical map  $\Lambda$  acting on a system qubit  $\rho_s$  can be described as the effect of a unitary operator on extended Hilbert space  $H_s \otimes H_e$  acting on an uncorrelated system-environment initial state [22, 107]. The environment state in Hilbert space  $H_e$  can be simply assumed to be  $|0_e\rangle\langle 0_e|$  without loss of generality. Then the system qubit obtained after the transformation is

$$\rho_s(t) = \Lambda(\rho_s(0)) = \text{Tr}_e \left( U(t) \rho_s(0) \otimes |0_e\rangle\langle 0_e| U^\dagger(t) \right) = \sum_k A_k \rho_s(0) A_k^\dagger, \quad (4.40)$$

where  $\text{Tr}_e$  is a partial trace operator acting on the environment and  $A_k = \langle k|U(t)|0_e\rangle$  is a linear operator acting on  $H_s$ . This map preserves the trace of the output state:

$$\text{Tr} \left( \sum_k A_k \rho_s(0) A_k^\dagger \right) = 1, \quad (4.41)$$

and the linear operators  $A_k$  satisfy the following property:

$$\sum_k A_k^\dagger A_k = \mathbb{1}_s. \quad (4.42)$$

Note that by linearity, a decomposition of the same form is obtained in the case when the environment is initially a mixed state.

Any linear map  $\Lambda$  taking linear operators to linear operators is called a superoperator. A quantum dynamical superoperator  $\Lambda_q$  describing the evolution of a quantum state over a time  $t$  must satisfy completely positive and trace-preserving (CPTP) conditions. The complete positivity condition guarantees that probabilities are positive and real even when the map is acting on part of an extended system if the initial state is composed of uncorrelated two systems. The trace-preserving condition guarantees that probability is conserved.

The expression in Eq. 4.40 subject to the condition in Eq. 4.42 is called a Kraus decomposition of the map  $\Lambda$ , and  $A_k$  are called Kraus operators. The Kraus representation of a given process is not unique, but all sets of operators are related through a unitary transformation.

## 4.5.2 Liouville representation

The Liouville representation [108] is a practical way of describing the action of a superoperator on a given state. Using the Liouville representation, the evolution can be written as vectorial multiplication between the state and the superoperator:

$$\Lambda(\rho) = \hat{\Lambda}|\rho\rangle\rangle, \quad (4.43)$$

where  $\hat{\Lambda}$  is a  $d^2 \times d^2$  matrix representation of  $\Lambda$ ,  $|\rho\rangle\rangle$  is a  $d^2 \times 1$  vector constructed by stacking the rows (or the columns) of  $\rho$ . If  $|\rho\rangle\rangle$  is formed by stacking the rows,  $\hat{\Lambda}$  can be expressed using Kraus operators as [109, 110]

$$\hat{\Lambda} = \sum_k A_k \otimes A_k^*. \quad (4.44)$$

Alternatively, if  $|\rho\rangle\rangle$  is formed by stacking the columns,

$$\hat{\Lambda} = \sum_k A_k^* \otimes A_k. \quad (4.45)$$

### 4.5.3 Lindblad equation

Another useful tool in the study of open quantum systems is the approach of master equations. The master equation describes non-unitary time evolution of an open system with a differential equation, and it can be written most generally in the Lindblad form as [110, 111]

$$\frac{\partial \rho}{\partial t} = -i[\mathcal{H}, \rho] + \sum_j \left( L_j \rho L_j^\dagger - \frac{1}{2} \{L_j^\dagger L_j, \rho\} \right) = -i[\mathcal{H}, \rho] + \mathcal{D}(\rho), \quad (4.46)$$

where  $L_j$ 's are called the Lindblad operators,  $\mathcal{D}(\square)$  is the dissipator. The derivation of the master equation of the above form relies on assumptions that the system and environment begin in a product state and the environment is Markovian, meaning that the environment has no memory.

The solution to Eq. 4.46 can also be expressed in the Liouville representation using the superoperator as

$$\hat{\Lambda} = \exp \left( i\hat{\mathcal{H}} + \hat{\mathcal{D}} \right), \quad (4.47)$$

where

$$\hat{\mathcal{H}} = \mathcal{H}^* \otimes \mathbb{1} - \mathbb{1} \otimes \mathcal{H} \quad (4.48)$$

$$\hat{\mathcal{D}} = - \sum_j L_j^* \otimes L_j - \frac{1}{2} \left( \mathbb{1} \otimes L_j^\dagger L_j - L_j^T L_j^* \otimes \mathbb{1} \right). \quad (4.49)$$

### 4.5.4 Relaxations of a spin ensemble

Two main sources of noise in NMR and ESR are spin-spin relaxation also known as transverse relaxation or dephasing characterized by  $T_2$ , and spin-lattice relaxation also known as longitudinal relaxation or amplitude damping characterized by  $T_1$ . In fact,  $T_1$  and  $T_2$  processes are dominating sources of decoherence in many other quantum devices as well. In the following, Kraus and Lindblad operators for dephasing and amplitude damping are listed as a reference. These terms are used for realistic simulations in later chapters.

#### Dephasing

The Kraus operators for dephasing are

$$A_0^d = \sqrt{1-p} \mathbb{1}, \quad (4.50)$$

$$A_1^d = \sqrt{p} \sigma_z, \quad (4.51)$$

where  $p = (1 - \exp(-t/T_2))/2$ , and the Lindblad operator for dephasing is

$$L_0^d = \frac{1}{\sqrt{2T_2}}\sigma_z. \quad (4.52)$$

### Amplitude damping

The Kraus operators for amplitude damping can be expressed as

$$A_0^a = \sqrt{p} \left( \sigma_\uparrow + \sqrt{1-\xi}\sigma_\downarrow \right), \quad (4.53)$$

$$A_1^a = \sqrt{p\xi}\sigma_+, \quad (4.54)$$

$$A_2^a = \sqrt{1-p} \left( \sqrt{1-\xi}\sigma_\uparrow + \sigma_\downarrow \right), \quad (4.55)$$

$$A_3^a = \sqrt{(1-p)\xi}\sigma_-, \quad (4.56)$$

where  $\sigma_{\uparrow,\downarrow} = (\mathbb{1} \pm \sigma_z)/2$  and  $\sigma_\pm = (\sigma_x \pm i\sigma_y)/2$ . Here  $p = (1 - (p_\uparrow - p_\downarrow))/2$  where  $p_{\uparrow,\downarrow}$  represent population of up and down states and  $\xi = 1 - \exp(-t/T_1)$ . The Lindblad operators are

$$L_0^a = \sqrt{\frac{p}{T_1}}\sigma_+, \quad (4.57)$$

$$L_0^a = \sqrt{\frac{1-p}{T_1}}\sigma_-. \quad (4.58)$$

### 4.5.5 Electron-nuclear cross relaxation

In a coupled spin system, if the probability of the forbidden two spin flip transition to occur is non-zero, the spin-lattice relaxation of one spin species induces relaxation of the other, the effect known as cross-relaxation. Typically, spin-lattice relaxation characteristic time scales with similar factor to gyromagnetic ratio and therefore the nuclear  $T_1$  process occurs in much longer time scale than that of an electron. However, in the electron-nuclear spin coupled systems, the cross-relaxation can introduce fast relaxation of the nucleus when anisotropic hyperfine interaction is strong. The effect of electronic  $T_1$  and anisotropic hyperfine interaction on a nuclear spin can be analytically shown via Kraus representation. Let us assume that the only source of noise acting on the electron-nuclear system is the electron  $T_1$  process. Then the Kraus operators describing the relaxation are  $A_0^a \otimes \mathbb{1}$ ,  $A_1^a \otimes \mathbb{1}$ ,

$A_2^a \otimes \mathbb{1}$ , and  $A_3^a \otimes \mathbb{1}$  in the  $\sigma_z$  basis, where  $A_j^a$  are shown in Eq. 4.53-4.56. Then we write these terms in the eigenbasis of the electron-nuclear spin Hamiltonian shown in Eq. 4.7 to obtain new Kraus operators Eq. 4.59-4.62.

$$\tilde{A}_0^a = A_0^a \otimes \mathbb{1}, \quad (4.59)$$

$$\tilde{A}_1^a = \sqrt{p\xi} (\cos(\eta)\sigma_+ \otimes \mathbb{1} - i \sin(\eta)\sigma_+ \otimes \sigma_y), \quad (4.60)$$

$$\tilde{A}_2^a = A_2^a \otimes \mathbb{1}, \quad (4.61)$$

$$\tilde{A}_3^a = \sqrt{(1-p)\xi} (\cos(\eta)\sigma_- \otimes \mathbb{1} + i \sin(\eta)\sigma_- \otimes \sigma_y), \quad (4.62)$$

where  $\eta$  was defined in Sec. 4.4.1. The forbidden transition rate of the electron-nuclear spin system scales as  $\sin(\eta)$  (see Eq. 4.35). We can see from the Kraus terms above that the strength of noise induced on the nucleus also scales with the strength of the forbidden transition.

## 4.6 Crystal orientation selection for optimal control

Eq. 4.5 shows that the orientation the static magnetic field with respect to the molecular crystal of electron-nuclear coupled spins alters the spin Hamiltonian. Hence the magnetic field orientation must be chosen in a way that reduces the durations and optimizes the fidelities of the quantum operations. AHC and pulsed ENDOR control schemes have very different orientation selection criteria, which are discussed below.

### 4.6.1 Orientation Criteria for Anisotropic hyperfine control

Nuclear spin flips can occur via electron-nuclear flip-flip forbidden transitions driven at a rate  $\omega \sin(\eta)/2$ , while the on-resonance allowed ESR transition is driven at  $\omega \cos(\eta)/2$  (see Eq. 4.35). Depending on the nuclear isotope and the dc field orientation,  $\sin(\eta)/2$  can be very small, preventing efficient control of the nuclear spins via microwave excitation. Thus, we aim to have an orientation that yields a pair of hyperfine coupling constants  $a$  and  $b$  (Eq. 4.7) that the ratio of forbidden to allowed transition rates are in the same order of magnitude, i.e.  $\tan(\eta) \sim 1$ . On the other hand, one desires to avoid strong forbidden transition rate in order to minimize the nuclear spin cross-relaxation induced by the electron  $T_1$  process as described in the previous section. Secondly, all allowed and forbidden transition frequencies should be separated from each other by at least the ESR line width in order to achieve universal control.

### 4.6.2 Orientation Criteria for ENDOR control

In the ENDOR control scheme, nuclear spin rotations are implemented directly by applying rf pulses on resonance with the nuclear transitions. Hence,  $\tan(\eta)$  does not need to be large. In fact, it is desirable to minimize  $\tan(\eta)$  in order to suppress cross-relaxation. As before, the allowed ESR transitions must be separated by at least the ESR linewidth, and the NMR transitions must be separated by at least the NMR (ENDOR) linewidth. The latter is determined by the nuclear dephasing time  $T_2^n \gg T_2^e$ , and is therefore much narrower than the ESR line width.

# Chapter 5

## Home-built instrumentation for X-band pulsed electron spin resonance

### 5.1 Introduction

This chapter describes our home-built pulsed electron spin resonance (ESR) spectrometer and a variable temperature probe containing a loop-gap resonator specifically designed for QIP applications using electron-nuclear spin systems. A pulsed ESR spectrometer operating at 8-12 GHz (X-band) provides acceptable thermal spin polarization and sensitivity for QIP experiments with relatively low cost. At the corresponding static field ( $\mathbf{B}_0$ ) strengths, the nuclear Zeeman and hyperfine interaction terms can be comparable, allowing for universal quantum control of electron-nuclear systems to be achievable by microwave-only control [31, 32, 97]. Most available commercial pulsed ESR spectrometers do not provide the flexibility and precision of control necessary for QIP with optimal control pulses. Hence we custom-designed and built an X-band ESR spectrometer, including a variable temperature probe and specially designed loop-gap resonator (LGR). The author's contribution to the home-built system is designing and building the low temperature probe assembly including the loop-gap resonator for about 10 GHz operating frequency. The probe is designed to fit in CF935O continuous flow cryostat from Oxford Instruments which is provided by Dr. David Cory, and can be cooled to just below 2 K. The probe also includes a sample holder which is used for positioning the ESR sample in a desired orientation with respect to the static magnetic field for optimizing the control, and the ability to apply



pulse implementation corrections.

## 5.2 Pulsed ESR spectrometer

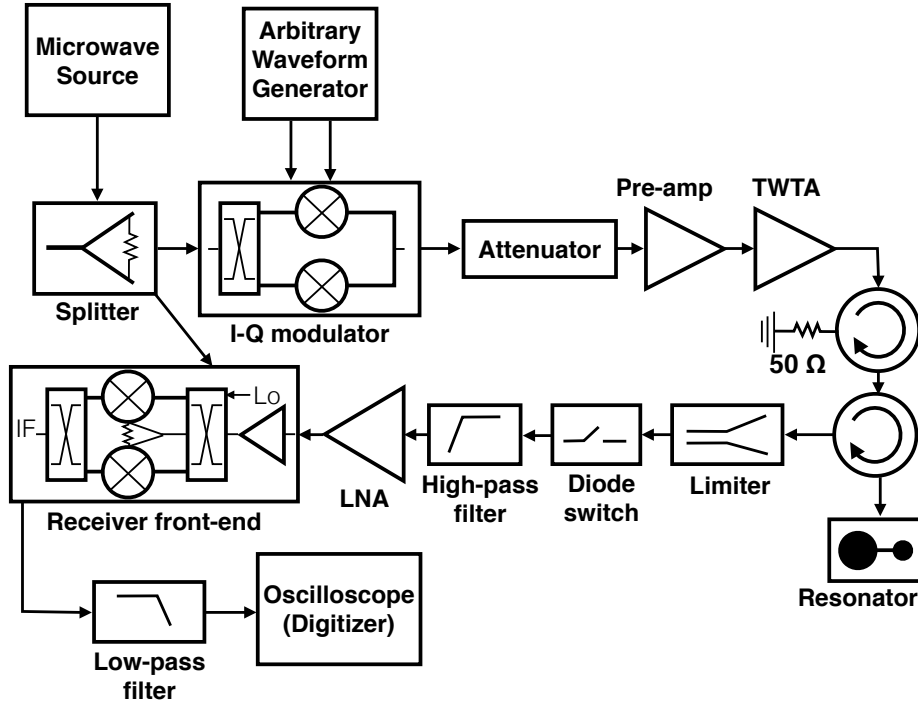


Figure 5.1: Schematic of the home-built X-band ESR spectrometer. A signal generated from the microwave source is mixed at the I-Q modulator with  $0^\circ$  (X) and  $90^\circ$  phase-shifted (Y) components of a shaped pulse from the arbitrary waveform generator. The I-Q modulator outputs the shaped pulse at upconverted frequency, and the pulse phase is accurately controlled (see text for details). TWT amplifier combined with a pre-amp and an attenuator provides the maximum output of 500 W. The amplified control pulse is transmitted to the sample placed in the loop-gap resonator, and the ESR signal is downconverted with the reference carrier frequency at the receiver. The high-pass filter removes IF transient produced by switching. The remaining IF signal is digitized by a fast oscilloscope.

Our X-band ESR spectrometer for quantum information processing was custom-designed and constructed by C. Ryan and J. Chamilliard [112]. The schematic of the home-built

X-band pulsed ESR spectrometer is depicted in Fig. 5.1. Microwave source (Rohde and Schwarz SMF100A) can provide a CW output of frequency ranging from 1 to 22 GHz, and the system is typically operated at  $\omega_0 \sim 10$  GHz for our applications. The source is equipped with options for enhanced phase noise performance and high output power up to +25 dBm. In order to generate arbitrary pulse shapes required by QIP such as Gradient Ascent Pulse Engineering (GRAPE) [72], we use single-sideband (SSB) upconversion technique [112, 113] and I-Q modulator as the SSB mixer. Arbitrary waveform generator (AWG) provides both  $0^\circ$  (X) and  $90^\circ$  phase-shifted (Y) pulse inputs from two output channels with  $\omega_{IF} = 150$  MHz intermediate frequency (IF). Applying IF signals of same amplitude but phase-shifted by  $\pi/2$  at I and Q ports suppresses the phase error of the output pulse due to non-linear power response of the I-Q modulator. The phase of the output microwave pulse is then controlled by the phase of IF signal generated by AWG, accurate upto 1 part in 16384. As the microwave CW signal with frequency  $\omega_0$  is mixed with the IF inputs with frequency  $\omega_{IF}$  at I and Q ports, the I-Q modulator outputs only the upconverted signal at  $\omega_0 + \omega_{IF}$ , and the lower sideband is removed. The shaped pulse must be amplified prior to being launched to the resonant sample cavity. Travelling wave tube (TWT) amplifier used in the system has maximum output of about 1 kW at 10 GHz. Prior to the TWT, a variable attenuator and low-gain solid-state amplifier are used in order to fully utilize the dynamic range of the TWT. The output microwave pulse from the TWT amplifier is directed by a circulator and travels to the loop-gap resonator (see Sec. 5.3) that surrounds the sample, where the pulse results in an oscillating magnetic field  $\mathbf{B}_1$ . The circulator has a peak power limit of 500 W, hence the TWT input is adjusted so that its output is limited to this value. The weak spin magnetization signal is directed by the circulator to a low-noise preamplifier and then to the receiver, where it is mixed with the reference frequency  $\omega_0$  and downconverted to  $\omega_{IF}$ . The receiver includes a second state of low-noise amplification. A diode switch (Advanced Technical Materials S1517D) is used to protect the receiver from being damaged by high power pulses from circulator leakage and reflection of signals from the loop-gap resonator. The switch is controlled by a marker channel of AWG. In addition, a diode limiter is used to protect the switch, which is also easily damaged by high microwave power. After the switch, a high-pass filter is incorporated in order to remove transients at IF caused by switching. Finally, the spin signal is digitized using a fast-digitizing and -signal-averaging LeCroy oscilloscope and is recorded on a computer for further data processing and analysis.

For more details about the home-built spectrometer design, we point to the reference [112] that provides comprehensive explanations.

### 5.3 Loop-gap resonator

In an ESR spectrometer, the resonator is used to convert input oscillating voltage to  $\mathbf{B}_1$  field on the sample and also to detect weak spin signals. We designed a loop-gap resonator (LGR) adapted from [114] in our home-built spectrometer with a resonance frequency of about 10GHz. The advantages of the LGR compared to conventional cavity resonators in the commercial spectrometers are large filling factors, large  $\|\mathbf{B}_1\|$  per square root watt, good  $\mathbf{B}_1$  uniformity and lower quality factor ( $Q$ ) which leads to larger bandwidths and shorter ringdown times [112, 115]. Fig. 5.2 shows the schematic of the two-loop, one-gap resonator. The loops and the gap are cut by wire electric discharge machining from a 9.6 mm  $\times$  5.4 mm  $\times$  2.5 mm copper block. The loop radii are 1.2 mm and 0.6 mm, and the gap is 0.1 mm wide and 3 mm long. The geometry of the LGR is chosen in order to have around 10 GHz resonance frequency and the  $Q \sim 150-300$ . The magnetic and electric field directions are shown in red and blue in the figure, respectively. The electric field is the strongest in the gap while the magnetic field is the strongest in the loop, and a sample is placed inside the smaller loop.

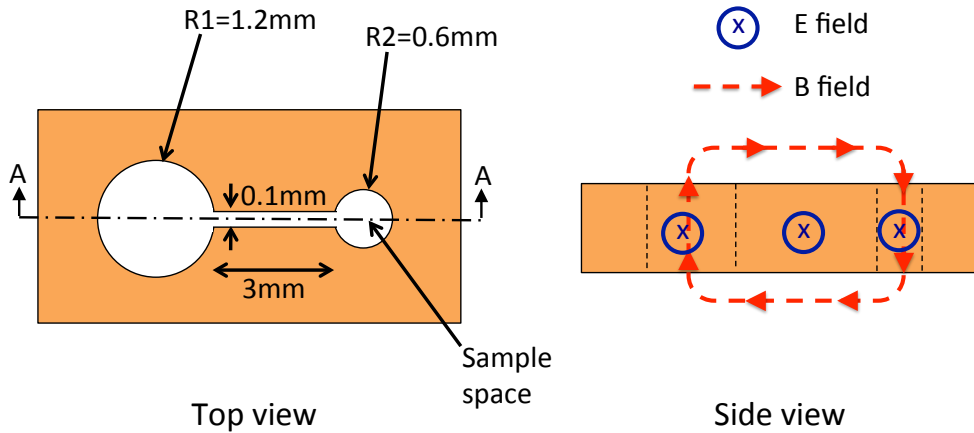


Figure 5.2: Schematic of the loop-gap resonator. The resonator has two loops and one gap, and it is made of copper. The geometry of the resonator is determined to yield about 10 GHz resonance frequency with  $Q \sim 150-300$ . The magnetic and electric field directions are shown in red and blue in the side view. The electric field is the strongest in the gap while the magnetic field is the strongest in the loop, and an ESR sample is placed inside the smaller loop.

## 5.4 Variable temperature probe

The resonator is placed in a copper rectangular box of a dimension  $9.4 \text{ mm} \times 9.6 \text{ mm} \times 5.4 \text{ mm}$ . For the given dimension, the lowest resonance frequency of this box is well above 12 GHz, and hence does not interfere with the LGR frequency. The inner conductor of a coaxial cable is formed into a one-turn loop and brought close to the larger of the two LGR loops, where it inductively couples the microwave signal to the LGR. The outer conductor of the coaxial cable is copper, and the inner conductor is silver-plated copper. Tuning and matching of the resonance is done by adjusting the position of the LGR relative to the coupling inductor. Note that Fig. 5.3 also shows another inductor that is inserted near the sample space above the smaller resonator loop for pulse implementation correction which is explained later in Sec. 5.6.

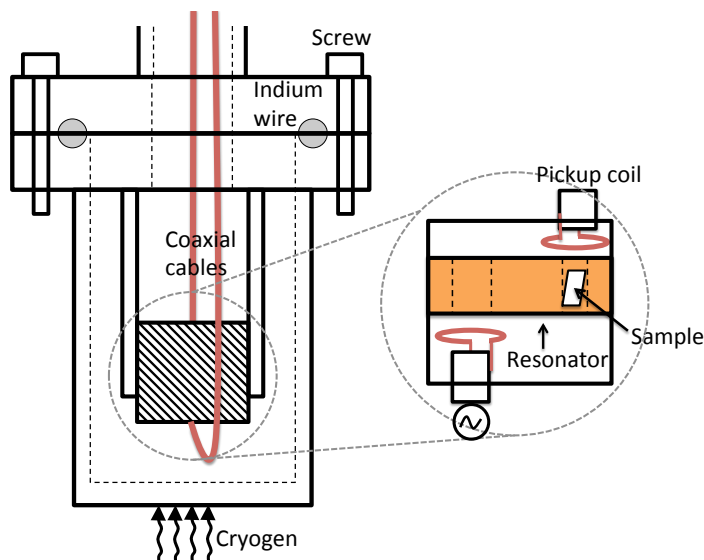


Figure 5.3: Schematic of the home-built ESR probe. The two-loop, one-gap resonator is placed in a copper rectangular box, and the box is placed in a cylindrical copper enclosure which makes contact with liquid helium vapour during cryogenic cool down. The cylindrical enclosure is sealed using indium wire and screws, and is evacuated during experiments. The inner conductor of a coaxial cable at one end is used to create an inductive loop, and the loop is placed near the larger LGR loop in order to couple the microwave input to the LGR. Tuning and matching of the resonance can be done by adjusting the position of the LGR relative to the coupling inductor. A second coaxial cable is used to pick up the microwave field during a pulse in order to correct the input for pulse imperfections.

In order to perform QIP with higher electron thermal spin polarization, we desire to cool the sample to cryogenic temperatures. Hence we designed and built a low-temperature probe that can be inserted in Oxford Instruments CF935O continuous-flow cryostat, and can be cooled with liquid helium. The rectangular box is mounted in the home-built low-temperature probe. The schematic of the probe is illustrated in Fig. 5.3. The resonator box is held inside the cylindrical enclosure made of copper, and the cylinder has 27.7 mm inner diameter and 85 mm inner depth. The probe is vacuum-pumped prior to and during the cryogenic cool down, and is sealed using indium wire and screws. The cylindrical enclosure makes contact with liquid helium vapour in order to cool the sample to cryogenic temperatures. Vacuum electrical feedthroughs are used to make coaxial connections between the electronics outside at the atmosphere pressure to the resonator.

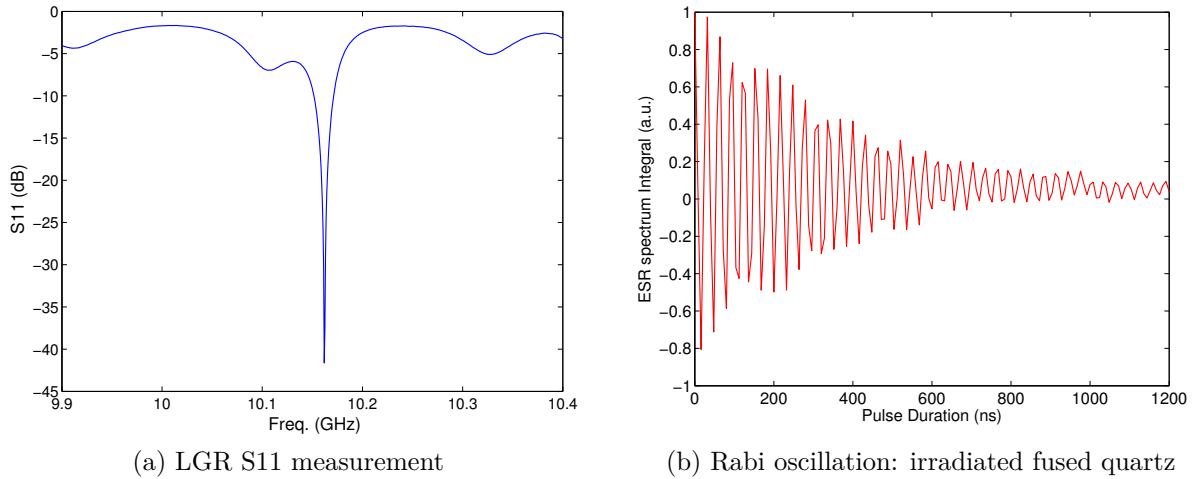


Figure 5.4: (a) LGR  $S_{11}$  measurement taken using a vector network analyzer (VNA). The measurement shows that the LGR’s resonance frequency is peaked at 10.16 GHz and the  $Q$  value is about 240. (b) The result of Rabi oscillation of an irradiated fused quartz ESR sample using the home-built spectrometer and the probe.

Fig. 5.4a shows typical resonator  $S_{11}$  (reflected microwave power) trace measured using a vector network analyzer (VNA) at room temperature when the resonator is assembled together with the probe. At the tuned frequency of 10.16 GHz, nutation frequency of about 30 MHz can be obtained with about 5 W input power level. Fig. 5.4b shows the result of Rabi oscillation of an irradiated fused quartz ESR sample using the home-built spectrometer and the probe.

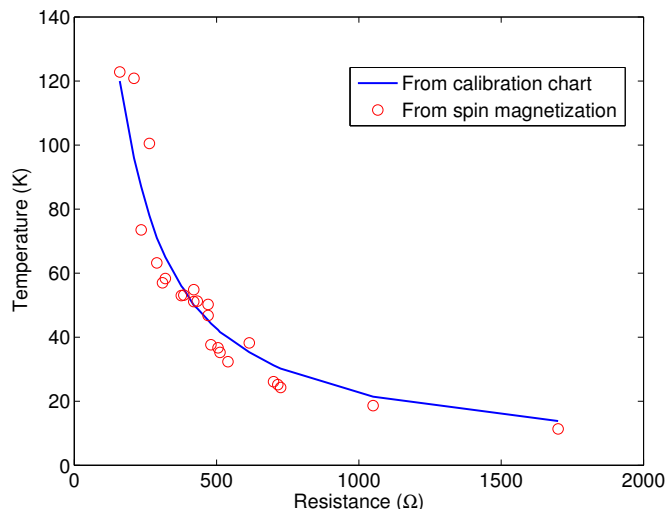


Figure 5.5: Various temperatures that an ESR sample have reached during an actual cool-down using liquid helium. A temperature sensor is mounted on the rectangular box and the reading on the temperature monitor is given as resistance in  $\Omega$ . The blue solid curve is obtained by using the calibration data provided by the temperature sensor’s manufacturer which converts the resistance reading to the temperature. The red circles are obtained by comparing the integral of a Fourier-transformed ESR spectrum measured at various temperatures to the integral of the room-temperature spectrum. The signal integrals normalized by the room-temperature data allows one to match the various resistance readings to temperatures on the y-axis of the plot.

Fig. 5.5 demonstrates various temperatures that an ESR sample have reached during an actual cool-down experiment using liquid helium. A temperature sensor is mounted on the rectangular box in order to estimate the sample temperature as precisely as possible. The temperature monitor is connected to the sensor and displays the resistance measured by the sensor. A calibration data table provided by the sensor’s manufacturer is used to convert the resistance to temperature (blue solid curve in Fig. 5.5). The sample temperature can also be calculated using Eq. 2.10, provided that a value of spin polarization at known temperature is given. We measured spin polarization at various temperatures, and used the value at room-temperature as a reference to calculate the sample temperature (red circles in Fig. 5.5) and compared to the measurement obtained by using the temperature sensor along with the calibration data. The results shown in Fig. 5.5 demonstrate good agreement between the two measurement methods, meaning that the measurement by the

temperature sensor is a good indication of the actual temperature of the ESR sample.

## 5.5 Sample holder

In Sec. 7.2.3, we discussed that the magnetic field needs to be oriented with respect to the sample in a way that optimizes the control fidelity. Since the position of the electromagnets of the spectrometer is fixed in the laboratory, one must be able to mount the sample in any desired orientation with respect to the magnetic field direction. One can start this task by selecting a clean surface of the target crystal, and measuring wanted hyperfine tensor in the coordinate system defined by the selected surface and its two orthogonal axes. Then the desired optimal orientation can be identified with respect to the selected surface of the crystal. A sample holder shown in Fig. 5.6 can be used to fix the crystal orientation in the resonator loop. The sample holder is cut from a cylindrical rod of rexolite. The sample holder has a freedom to rotate along the axis perpendicular to the direction of  $\mathbf{B}_0$  field by rotating the entire ESR probe. The selected crystal surface is glued on the surface of the sample holder that makes an angle  $\theta$  with respect to the direction of  $\mathbf{B}_0$  as shown in Fig. 5.6b, along an axis  $u$  (red arrow in Fig. 5.6a) in the plane perpendicular to the rotating axis of the probe (green arrow in Fig. 5.6b). The freedom to select the direction of  $u$  and  $\theta$  allows one to orient the chosen surface of the crystal in any target orientation.

One drawback of using the sample holder is that it limits the size of the crystal, which results in reduced detection sensitivity. Therefore, the surface of the crystal must be wisely chosen so that when the crystal on the sample holder is inserted in the resonator loop it fills as much space as possible. Moreover, the design of the sample holder must ensure that the ESR sample is placed at the center of the cylindrical sample space as much as possible for good  $\mathbf{B}_1$  field homogeneity.

## 5.6 Pulse implementation correction

The control field seen by the paramagnetic sample does not exactly match the desired pulse shape due to random noise in the electronics and systematic errors by non-linearities in the pulse generation and amplification, and by the limited bandwidth ( $\sim \omega_0/(2\pi Q)$ ) of the probe circuit. To achieve high fidelity control, these errors must be minimized so that the spin system is irradiated with the pulse shape as close as possible to the designed one. The systematic portion of the errors can be reduced substantially by placing a pickup coil to measure the pulse in the vicinity of the sample space and running a feedback loop

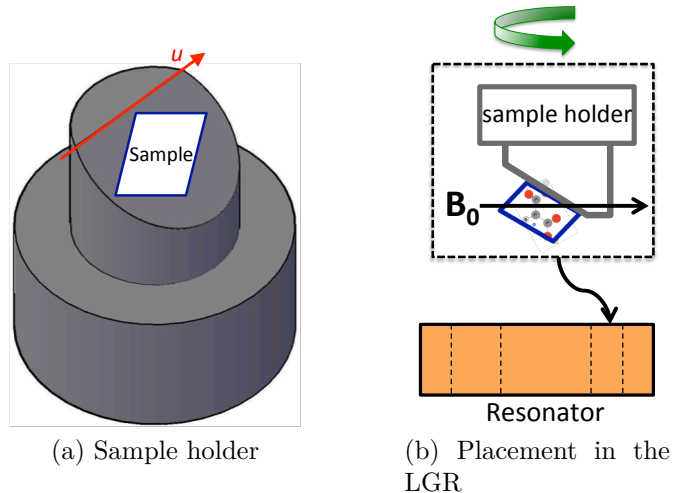


Figure 5.6: (a) Schematic of ESR sample holder. The sample holder is cut from a rexolite cylindrical rod, and the ESR sample is glued on the slanted surface whose angle is determined by desired crystal orientation.  $u$  is the axis of rotation for the slanted surface, and the direction of  $u$  can be determined by rotating the probe around the axis perpendicular to the direction of  $B_0$  field. The sample holder is placed in the resonator as shown in (b)

such that a new pulse form is calculated to compensate for the imperfections [37]. The control field is adjusted based on the measured pulse shape. The feedback loop is repeated until the measured new pulse is close enough to the desired shape. The closeness between the actual and the ideal pulses can be defined as the sum of the squares of the residuals normalized by the number of points.

The amplitude of the signal transmitted from the resonator is orders of magnitude larger than that generated by the spin. Thus, a variable attenuator is used to reduce the reflected signal amplitude. The amplification steps in the receiving train is also removed. By omitting the amplification steps, distortions of the pulse as it is transmitted to the oscilloscope can be reduced. Instead of using the receiver front-end which included additional amplification, a mixer is used for downconverting the measured signal to IF. The circulator port that was used to output the spin signal reflected from the resonator is terminated with a  $50 \Omega$  load since now the pulse is transmitted through the pickup coil. The spectrometer modification for the pulse implementation correction is depicted in Fig. 5.7.

Fig. 5.8 shows a sample result of the pulse-fixing procedure. The top figure (a) compares the actual pulse shape measured by the pickup coil (red solid) to the ideal one (blue



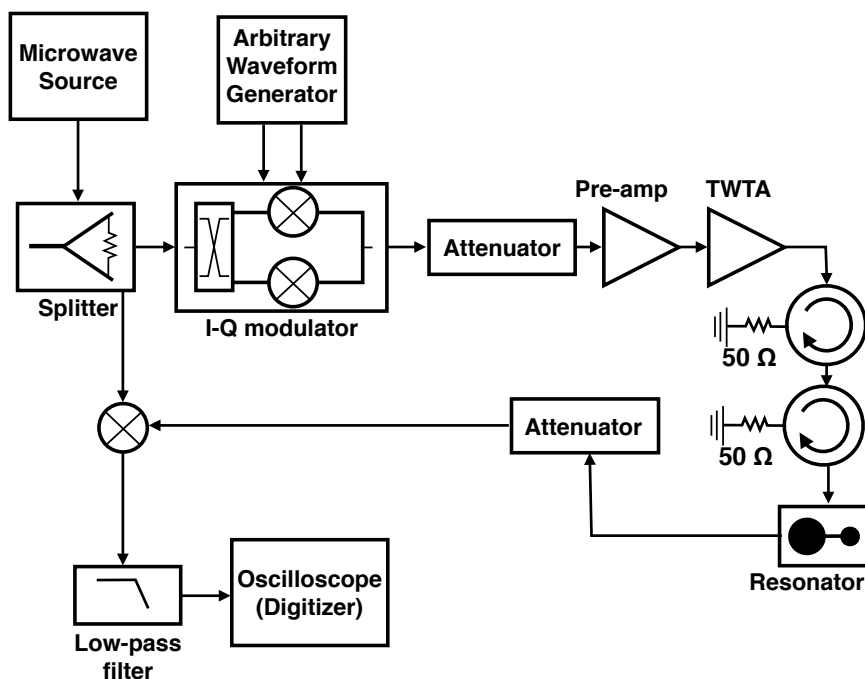
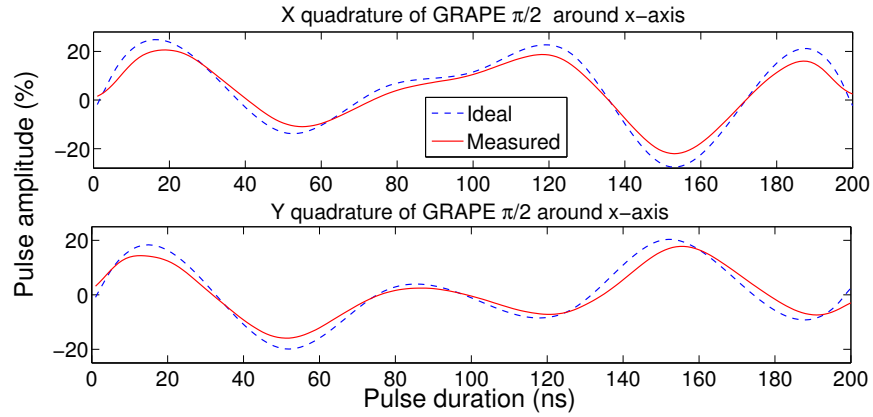


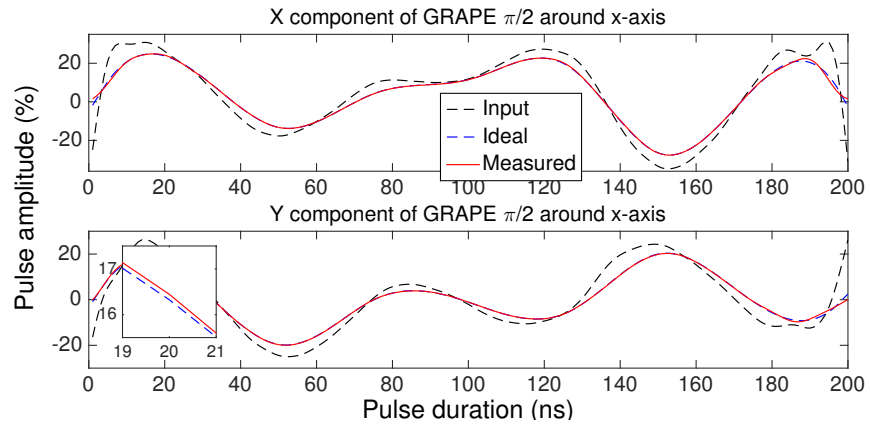
Figure 5.7: Schematic of the spectrometer modified for the pulse implementation correction. The signal is transmitted from the resonator through the pickup coil that is connected to a mixer for downconverting to IF. Then the IF signal is observed by the oscilloscope. The circulator port that was used to transmit the spin signal is terminated with a  $50 \Omega$  load. Since the amplitude of the pulse transmitted from the resonator is much larger than the spin signal, a variable attenuator is used in between the pickup coil and the mixer. Also, the pre-amplification in the receiving train is removed. Removing the amplification steps also helps to prevent any pulse distortions that may arise in the amplification steps.

dashed) before applying pulse correction. The bottom figure (b) demonstrates that the pulse implementation correction procedure adjusts the input pulse shape so that the measured pulse matches very close to the ideal one. The green dashed curve is the adjusted input pulse shape obtained after running several cycles of pulse-fixing that outputs a measured pulse that is reasonably close to the intended shape. GRAPE pulse can be designed to be robust to small pulse amplitude deviations (Sec. 4.4.2), and hence high fidelity control can be achieved as long as the difference between the measured and ideal pulses are small.

Note that the pulse imperfections depend on the pulse power. Therefore, it is important



(a) Measured vs ideal pulse shape before pulse-fixing



(b) Measured vs ideal pulse shape after pulse-fixing

Figure 5.8: (a) Pulse shape measured by the pickup coil (red) before pulse implementation correction compared to desired pulse shape (blue dashed). The figure shows large disagreement between the two which leads to large gate error. (b) After applying the pulse implementation correction several iterations, the input pulse shape is adjusted (black dashed) such that the pulse measured in the vicinity of the sample (red) is very close to the desired one (blue). The amplitude difference between the measured and ideal pulses is very small that they are hard to be distinguished in the figure scale. The inset at the bottom figure magnifies a part of the plot region to show small difference between red and blue curves. GRAPE pulse can be made robust to small amplitude fluctuations to compensate for remaining errors between the measured and ideal pulse shapes.

that the pulse is corrected at the power level at which it will be used. Also, this procedure assumes that the transfer function of the pickup coil is flat over the entire bandwidth of the control field, which in practice is only approximately true.

## 5.7 Future work

The home-built spectrometer described in this chapter is capable of irradiating the paramagnetic samples with only microwave pulses that induce electron spin transitions. Although universal control can be achieved using AHC, and ESEEM allows measurement of the nuclear frequencies for spin Hamiltonian determination at given orientation, constructing a pulsed ENDOR set-up can be beneficial. The pulsed ENDOR is particularly useful for the spin Hamiltonian determination and optimal control when the anisotropic part of the hyperfine interaction is weak. Some preliminary work towards implementing the pulsed ENDOR feature is already done. The AWG used for creating IF in the microwave pulse forming step can also be utilized for generating RF pulses at nuclear resonance frequencies. The probe is equipped with extra coaxial cables on which an RF coil can be easily mounted, and the coaxial cables are connected to vacuum electrical feedthroughs as well. Moreover, our simulation code that runs on a classical computer already includes capability of simulating ENDOR experiments. The most important and challenging task that remains is adding an RF amplifier to the spectrometer, and making sure that the RF pulses are formed and delivered to the electron-nuclear system as desired.

# Chapter 6

## Randomized benchmarking of quantum gates as a tool for characterizing and improving microwave control

### 6.1 Introduction

For the newly constructed instrumentation explained in the previous chapter, the first natural experiment is benchmarking the performance, identifying issues, and then incorporating further improvements. This chapter presents our work on randomized benchmarking of single qubit operations for characterizing and improving the microwave control available in the home-built ESR spectrometer introduced in Ch. 5.

Characterizing how well an operation is implemented in a given quantum architecture is of fundamental importance in the development of QIP. In Ch. 1, we mentioned that according to the threshold theorem, arbitrarily long computation with given accuracy is possible using a polynomial amount of resources, provided that the error per gate is below a certain threshold value. The average gate error threshold for fault tolerant quantum computing is in general thought to be around  $10^{-4}$ , although the tolerance to errors can be less stringent given impractically large amount of resources [116], or in certain quantum computational models [117]. Thus any quantum devices developed for QIP must be assessed to determine whether the required level of control is reached. One way of characterizing the quantum operation is quantum process tomography (QPT) [118], but the number of measurement

necessary to completely map a process increases exponentially with the number of qubits involved. Moreover, QPT is not able to distinguish between the state preparation and measurement (SPAM) errors and control errors, restricting QPT from measuring control errors that are smaller than or comparable to SPAM errors. Fortunately, one does not require the complete knowledge of the quantum process, but rather a coarse grained parameter that accurately represents the computationally relevant average gate error suffices in the context of fault tolerant quantum computing. Randomized benchmarking (RB) protocol [19, 119, 120] is a scalable approach to estimate average error probability, and has been used to assess average gate fidelity in various quantum information processors such as trapped ions [19, 121, 122], liquid state NMR [123], superconducting qubits [124, 125], atoms in optical lattices [126], and  $^{31}\text{P}$  donor in silicon [127]. The basic idea of RB is to randomize over a set of computational gate sequences followed by a reverse (recovery) operation so that the entire evolution is the identity operation in the absence of error. The computational gate set should be chosen such that it forms a depolarizing channel upon averaging when each operation is subject to gate-independent error. Then the depolarizing parameter  $d$  of the averaged channel  $\bar{\Lambda}$ :

$$\bar{\Lambda} = (1 - d)\rho + \frac{d}{D}\mathbb{1} \tag{6.1}$$

is related to the average gate fidelity. Randomization over the unitary group provides a benchmark over the complete set of quantum gates. However, since the unitary group is a continuous set with a number of parameters increasing exponentially in the number of qubits  $n$ , generating an arbitrary unitary operator is also exponentially hard in  $n$ . Tracking the state through the computation in order to calculate the final state fidelity and the recovery operation is also exponentially hard. Therefore, it is more practical to benchmark a discrete set of gates that is useful in quantum computation. Also, it is desirable that the operations are efficiently tractable and can be generated using a scalable number of known one and two qubit gates. Clifford group, denoted as  $\mathcal{C}$ , is one such set that is attractive for benchmarking for several reasons. First, although the Clifford group itself is not a universal gate set, the unitary group can be generated using  $\mathcal{C}$  with an additional single-qubit gate, such as  $\pi/8$  gate. The  $\pi/8$  gate can be implemented using a magic-state [128], Clifford gates, and a measurement in the computational basis, meaning that there exists a universal quantum computation model in which all necessary gates can be drawn from the Clifford group [128]. Furthermore, benchmarking the Clifford gates is useful since most encoding schemes for fault tolerant QIP are based on stabilizer codes, in which the error correction is performed mainly using Clifford gates. Therefore, our experiment is focused on quantifying the average gate fidelity of the single qubit Clifford operations.

## 6.2 Single qubit protocol

The single qubit randomized benchmarking protocol used to quantify the error per gate exactly follows the liquid state NMR version of the benchmarking experiment presented in [123]. The single qubit Clifford twirling is equivalent to a twirling using the 48 operations parametrized as [38, 123, 129]

$$\mathcal{C} \cong \mathcal{SP} = \exp\left(\pm i\frac{\pi}{4}Q\right) \exp\left(\pm i\frac{\pi}{2}V\right), \quad Q \in \{\sigma_x, \sigma_y, \sigma_z\}, V \in \{\mathbb{1}, \sigma_x, \sigma_y, \sigma_z\}. \quad (6.2)$$

In this protocol, the  $\pi/2$  pulses (denoted  $\mathcal{S}$  in Eq. 6.2) are computational operations while the Pauli operations serve only to redefine the Pauli frame which helps to depolarize the noise. A natural choice for the known initial state is the thermal state, which can be simply represented by its traceless part as  $\rho_i = \sigma_z$  since the identity part of the density matrix is irrelevant in both unitary evolution and the measurement in ESR QIP. The initial state is tracked through a sequence of Clifford operations (Eq. 6.2), and the sequence is truncated at different lengths  $l \leq L$  to measure the fidelity decay curve. At each truncation  $l$ , a recovery gate is chosen at random to return the state to either  $\pm\sigma_z$ . The spin echo is detected for the measurement. In the experiment, we pre-calculated the final state prior to the spin echo measurement, and chose the phase of the read-out pulse so that we always measure the positive eigenvalue.

The quantum circuit implementing a particular series of Clifford operations is shown in Fig. 6.1.

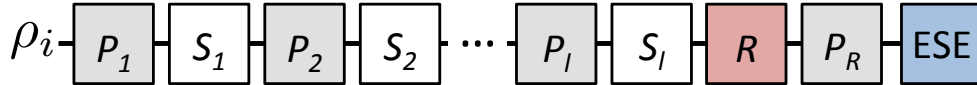


Figure 6.1: A particular realization of Clifford sequence in the randomized benchmarking protocol.  $P$  and  $S$  indicate Pauli and computational operations, respectively, and  $R$  is the recovery gate that brings the state to either  $\pm\sigma_z$  chosen at random with equal probability. The sequence is truncated at some length  $l$ , and the final state is measured from electron spin echo (denoted ESE in the figure).

The single qubit protocol can be summarized as follows:

1. Choose a maximum number of Clifford operations  $L$ , and a set of random integers  $l \in \{l_1 < \dots < L\}$  that is the length of a truncated pulse sequence (i.e. a subsequence). The number of elements in  $l$  is denoted  $N_l$ .

2. Generate  $N_g$  random sets of  $L$  computational gates, and truncate each sequence at length  $l_k \in l$ .
3. For each subsequence of length  $l_k$  (total  $N_g \times N_l$  subsequences), do the following:
  - (a) Generate  $N_p$  random sets of Pauli gates of length  $l_k + 2$ .
  - (b) Interleave computational gates with the  $l_k + 1$  Pauli gates.
  - (c) Calculate recovery operation and insert it after  $(l_k + 1)^{th}$  Pauli gate.
  - (d) Insert final Pauli randomization gate before the spin echo detection.
  - (e) Calculate the phase of the spin echo read-out pulse that yields the positive eigenvalue of  $\sigma_z$ .
4. Evolve the known initial state under each of the  $N_g \times N_l \times N_p$  number of random pulse subsequences.
5. Measure electron spin echo integrated intensity at the end of each subsequence and compare with a reference state.
6. For each  $l_k$  where  $k = 1 \dots N_l$ , calculate the average remaining spin magnetization along  $\sigma_z$  by averaging over  $N_g \times N_p$  subsequences.
7. Plot the average remaining signal as a function of  $l$ , and fit the curve to  $f_l = \alpha(1-d)^l$ , where the average gate error is  $d/2$ . The SPAM error is absorbed in the constant  $\alpha$ .

As indicated in steps 6 and 7, we calculate the average gate error from the decay rate of  $\langle \sigma_z \rangle$  as a function of the number of gates  $l$ .

## 6.3 Experiment

### 6.3.1 Simulations and initial experimental run

The single qubit system employed for the benchmarking experiment is irradiated fused-quartz [130], a paramagnetic sample in powder form. We measured  $T_1 = 160 \mu s$ ,  $T_2 = 5 \mu s$ , and  $T_2^* = 60 \text{ ns}$  at room-temperature.  $T_2^*$  is obtained from the linewidth of the thermal-state ESR spectrum in the frequency domain. The  $T_2^*$  broadening here is mainly due to the anisotropy of the g-value, which produces a powder pattern of width of about 5 MHz, and also to non-uniformity of the static magnetic field. Different spins within the

sample may also experience different nutation frequencies due to the inhomogeneity of the applied microwave ( $\mathbf{B}_1$ ) field in the resonator loop. By taking the Fourier transform of the time-domain Rabi oscillations, we obtain the  $\mathbf{B}_1$  distribution profile over the sample. The ESR line-broadening due to  $T_2^*$  noise and the  $\mathbf{B}_1$  distribution profile are shown in Fig. 6.6. Using the decoherence parameters and the  $\mathbf{B}_1$  inhomogeneity data, we simulate RB protocol with  $N_g = 7$ ,  $N_p = 14$  giving a total of 98 sequences, and  $l = \{1, 2, 7, 9, 10, 12, 14, 18, 20, 21, 25, 28, 32, 57, 60, 66, 74, 97, 110, 128\}$ . Both computational and Pauli gates are realized by 35 ns long Gaussian-shaped microwave pulses, yielding Clifford operations that are 70 ns in total length. Figure 6.2 summarizes the simulation results

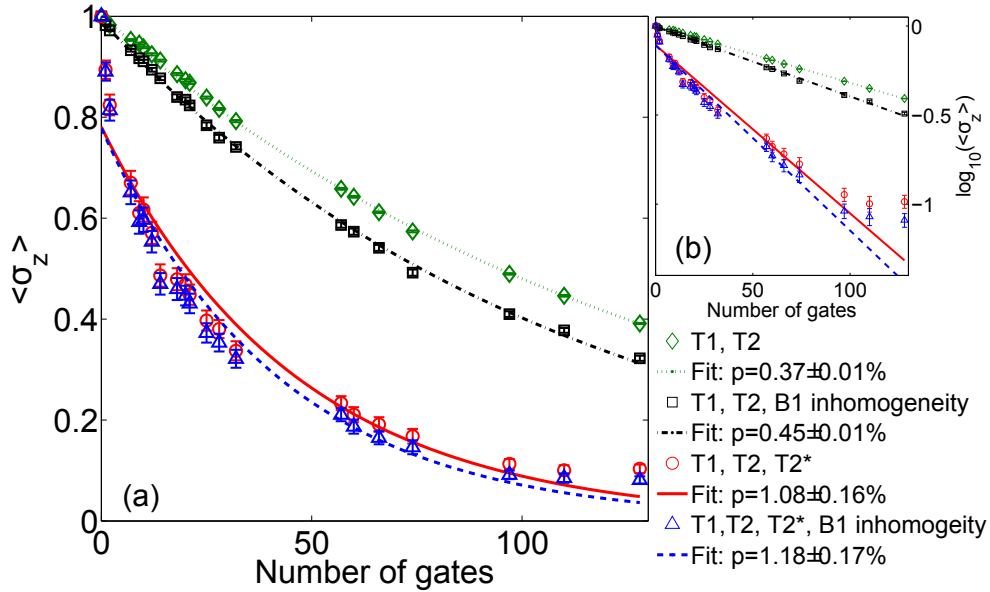


Figure 6.2: Results of simulated randomized benchmarking on the single qubit (fused quartz) spin system. (a) and (b) show the results plotted in the linear and semi-log scale, respectively. The expectation value  $\langle \sigma_z \rangle$  is measured after application of  $l$  randomized gates. The simulations used experimentally measured values of  $T_1$ ,  $T_2$ , and  $T_2^*$  at room-temperature, which are  $160 \mu\text{s}$ ,  $5 \mu\text{s}$ , and  $60 \text{ ns}$ , respectively. Green is obtained by simulating with only  $T_1$  and  $T_2$  of the electron as the error source. Black curve includes  $B_1$  field inhomogeneity, and the  $B_1$  distribution obtained from the Rabi oscillation experiment is used for the simulation. Red curve shows the simulation result with  $T_2^*$ , but no  $B_1$  distribution, and blue is the result from simulating all noise sources,  $T_1$ ,  $T_2$ ,  $T_2^*$  and  $B_1$  distribution.

under four different conditions: (1) no  $B_1$  inhomogeneity and no  $T_2^*$  effect, (2) with  $B_1$



inhomogeneity and no  $T_2^*$  effect, (3) no  $B_1$  inhomogeneity and with  $T_2^*$  effect, (4) with  $B_1$  inhomogeneity and  $T_2^*$  effect.  $T_1$  and  $T_2$  processes are included in all four cases. In the absence of any local field distributions, the error per gate is 0.37%. Since there are no pulse implementation errors, the imperfection is solely due to  $T_1$  and  $T_2$  processes. As the local field inhomogeneities are included, the error per gate increases to 0.45% for  $B_1$ , 1.08% for  $T_2^*$  and 1.18% for both  $B_1$  and  $T_2^*$ . It can be concluded that  $T_2^*$  inhomogeneous broadening more critically increases the error rate than  $B_1$  inhomogeneity in our case.

Without any optimization of the microwave pulses, randomized benchmarking was implemented in the quartz single-qubit system. The error per gate was more than 6%, indicating an insufficient level of control for QIP purposes. In the following section, we discuss the modifications on the hardware configuration made to minimize the control imperfections.

### 6.3.2 Hardware configuration optimization for high fidelity control

The pickup coil introduced in Sec. 5.6 is used to directly measure the microwave field in the vicinity of the sample. The largest and most obvious pulse imperfection revealed by the pickup coil was a phase transient error. The input testing pulse is 35 ns Gaussian shape applied along the y-axis, meaning that the amplitude of the imaginary component (x-axis component) of the pulse is zero everywhere. However, as shown in Fig. 6.3a, the measured output pulse indicates a noticeable phase transient. This transient was found to be present at the output of the I-Q modulator. The transient effect leads to undesired spin dynamics as shown in Fig. 6.3b.

The figure shows the rotation of the spin magnetization vector as the power of the input Gaussian pulse is varied. The pulse is applied along the y-axis, and solid and dashed curves represent real (x) and imaginary (y) components of the measured spin signal. In the absence of the pulse error, the imaginary part is zero at all power levels since the spin magnetization vector remains within the x-z plane. However, the non-zero y-component in Fig. 6.3b indicates that the spin is rotated out of the x-z plane by the phase transient. In order to suppress this pulse error, we design an input pulse with an imaginary part of equal amplitude but opposite sign to cancel the transient. The phase transient corrected (PTC) pulse is designed as follows. First, we take the imaginary part of the measured pulse shape, and digitize it so that the time resolution of the measured pulse matches the AWG sampling rate. Then we multiply the imaginary part of the digitize pulse by a factor of  $-1$  to negate the phase error. However, the digitization step can introduce

small unwanted scaling in the pulse amplitude, and thus the multiplication by  $-1$  may not exactly cancel the unwanted imaginary component. We found that introducing a scaling factor of 1.07 to the PTC pulse yields the best result in minimizing the phase transient effect. Fig. 6.4a demonstrates that using the modified input pulse, the phase transient error is significantly reduced. The deviation of the spin evolution trajectory from the x-z plane previously shown in Fig. 6.3b is significantly suppressed when the same experiment is conducted using the PTC input pulse as shown in Fig. 6.4b. It should be noted that the real component of the pulse is asymmetric in time, with a slowly decaying tail; this is due to the finite bandwidth of the resonator. However, since the integrated pulse area of the real part can be adjusted with high accuracy to yield desired spin rotation by the pulse amplitude calibration, we only correct the distortion in the imaginary part of the pulse.

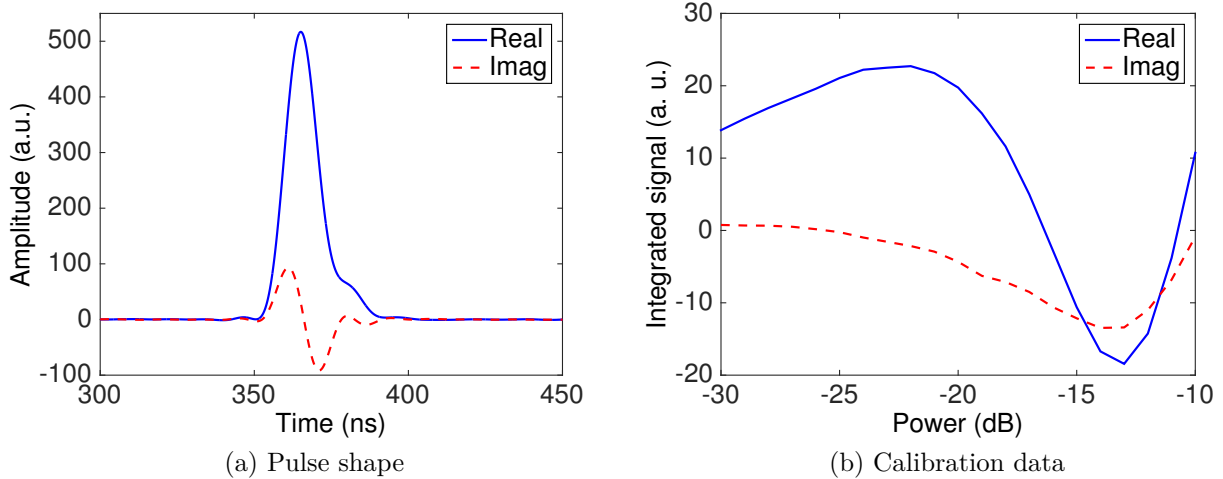


Figure 6.3: (a) The shape of a 35 ns Gaussian pulse measured using the pickup coil shown in Fig. 5.3. The pulse is applied along the y-axis. The solid curve represents the real part (phase along +y) of the measured pulse and the dashed curve is the imaginary part (phase along +x). Ideally, the imaginary component of the pulse is zero everywhere, but a considerable phase transient is observed. (b) Spin magnetization signal measured as a function of the pulse power of the 35 ns Gaussian pulse shown in (a). Without pulse imperfections, only the real part (x-component) of the signal (solid) should oscillate as a function of the pulse power while the imaginary part should be zero everywhere. However, the phase transient leads to undesired spin rotation out of the x-z plane.

Another factor that significantly contributed to the large error per gate was the phase and amplitude droop arising from the high power TWT microwave amplifier, and found

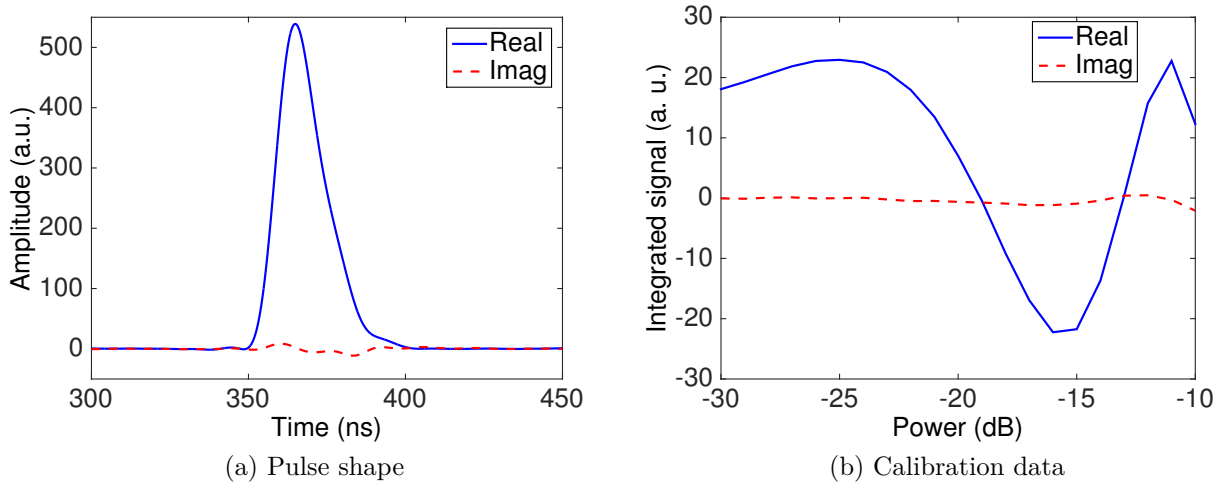


Figure 6.4: (a) The shape of a 35 ns Gaussian pulse after implementing the phase transient correction explained in the main text. The unwanted imaginary component (x-quadrature) of the pulse is suppressed. (b) Spin magnetization signal measured as a function of the pulse power of the corrected pulse. The unwanted deviation of the spin trajectory from the x-z plane is much lower compared to the uncorrected pulse.

to be dependent on the pulse blanking time. Fig. 6.5a shows the shape of a series of the phase transient corrected (PTC) 35 ns Gaussian pulses when the TWT blanking delay is set to be 300 ns. It is clear from the figure that both amplitude and phase are not stable until about 2  $\mu$ s after the blanking switch is turned on. Use of the 300 ns blanking delay is clearly problematic for any experiment involving a sequence of pulses or long pulses. Therefore we configured the TWT blanking switch to be 2  $\mu$ s prior to a pulse to allow both amplitude and phase of the output pulses to stabilize. Fig. 6.5b shows that with the 2  $\mu$ s TWT blanking delay, the pulse amplitude and phase stabilities are very good.

After the phase transient effect is corrected and the TWT blanking delay is set to 2  $\mu$ s, the randomized benchmarking experiment was carried out again, and the error per gate found to be  $1.72 \pm 0.25\%$ . Nevertheless, the error per gate is still about an order of magnitude larger compared to the error rate expected due to  $T_1$  and  $T_2$  effects. The error probability can be further decreased by reducing local field inhomogeneities, which will be discussed in the next section.

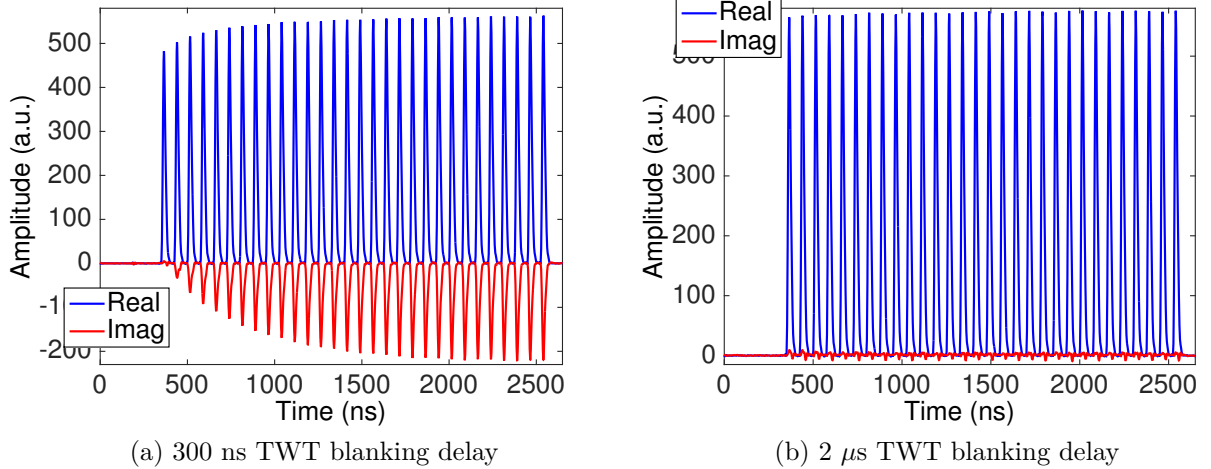


Figure 6.5: (a) Series of the phase transient corrected 35 ns Gaussian pulses with 300 ns TWT blanking delay. After the blanking switch is on, the amplitude and phase of the pulse require about 2  $\mu$ s to stabilize. (b) The same series of pulses with a 2  $\mu$ s blanking delay, indicating good stability of both phase and amplitude.

### 6.3.3 Selection sequence to reduce field inhomogeneities

The simulation results shown in Fig. 6.2 indicate that the average gate fidelity is notably limited by local field inhomogeneities such as  $T_2^*$  effect that is related to the uncertainty in the Larmor frequency and the  $\mathbf{B}_1$  field inhomogeneity that is related to the uncertainty in the nutation frequency.

One approach to overcome such field inhomogeneities is to use composite pulses [131]. However, designing a composite pulse sequence typically involves many number of pulses. For example, a composite pulse for the spin inversion ( $\pi$ -rotation) that is robust to the field inhomogeneity requires at least three individual pulses [132], meaning that the total pulse duration of either a Pauli or a computational gate in our implementation is 115 ns (three gaussian pulses each with 35 ns). The minimum duration of the composite pulse sequence is already longer than  $T_2^*$ , and also when the benchmarking pulse sequence is composed of such long composite pulses,  $T_2$  noise starts to contribute more significantly. Even in the absence of the field inhomogeneities, simulating the randomized benchmarking protocol using the 115 ns three-pulse composite pulses yields the error per gate of  $1.08 \pm 0.01\%$  where the error solely comes from  $T_1$  and  $T_2$ . The error probability is as high as when the system is exposed to the non-uniform field error, but no composite pulses are used. Thus,

designing composite pulses does not help improving the average gate fidelity in our case where the composite pulse duration is not sufficiently shorter than the decoherence time scale.

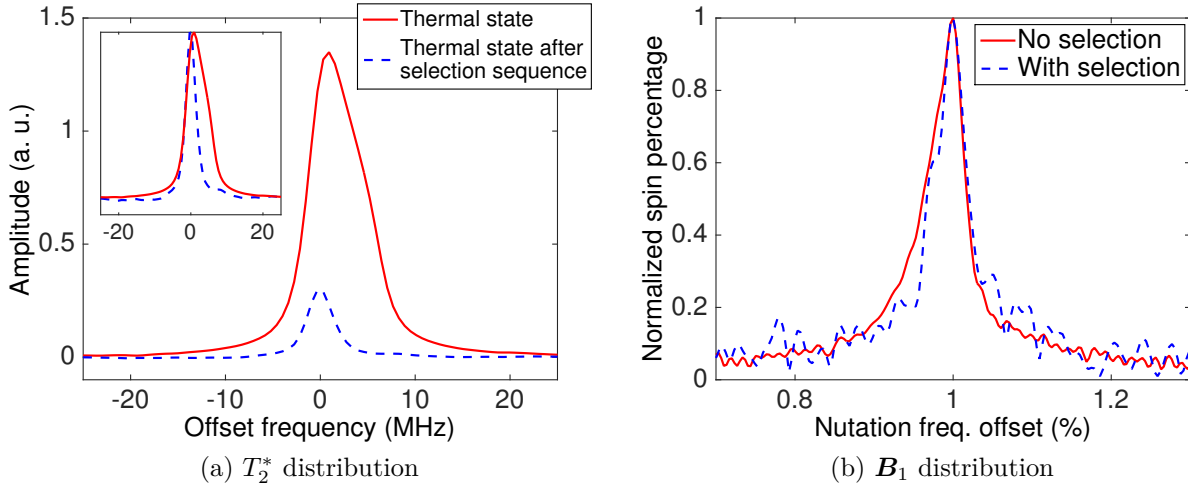


Figure 6.6: (a) Comparison of the ESR spectrum before (solid) and after (dashed) applying the spatial selection sequence explained in the main text. The signal intensity is substantially reduced since only a small portion of the spin magnetization remains after the sequence. However, the linewidth is significantly reduced, as shown in the inset where we plot the two spectra normalized to the same amplitude. The sequence reduces spin magnetizations at larger frequency off-sets while selecting spin packets near zero off-set frequency. Hence the center of the ESR spectrum shifts towards zero off-set frequency after the selection sequence. (b)  $B_1$  distribution profile obtained by taking the Fourier transform of the Rabi oscillation data without the selection sequence (red) and after implementing the selection sequence (blue).

Another approach is to design a selection pulse sequence that leaves polarization on only a subset of the spin ensemble with narrower inhomogeneous line-broadening, similar to the idea of RF selection [37, 69, 70]. The selection sequence is constructed as follows. First, a 400 ns GRAPE pulse with 1 ns discrete time step rotates spins that experience exactly on-resonance local field by  $2\pi$  around x-axis with 99.9% unitary fidelity. For the spin packets seeing off-resonance local fields, the unitary fidelity quickly decreases. Hence most of the spins pointing along the z-axis after the GRAPE pulse sees on-resonance field. Next, we wait  $T_2$  in order to dephase the transverse component of the off-resonance spin packets pointing along some other directions in the Bloch sphere. By repeating these two

steps, one can reduce off-resonance portion of the spin ensemble. Although longer wait time is desired for eliminating the transverse spin magnetization, the delay must be much shorter than  $T_1$  in order to minimize the equilibration of the unwanted off-resonance spin packets. We find that waiting for  $T_2$  is sufficient for effectively reducing the width of the  $T_2^*$  line-broadening. There is a trade off between the amount of signal and the width of the distribution, and in our case, iterating the sequence four times provides the optimal result. Despite the signal loss, after four cycles of the sequence,  $T_2^*$  is extended to about 160 ns as shown in Fig. 6.6a. Note that the selection sequence does not necessarily improve the  $\mathbf{B}_1$  field inhomogeneity as shown in Fig. 6.6b. In order to reduce  $\mathbf{B}_1$  field inhomogeneity, only the spin packets from localized region of the sample needs to be selected. Although our sequence selects a subset of the powder pattern, the selected spin packets are uniformly distributed across the sample, and thus there is not much difference in the  $\mathbf{B}_1$  distribution before and after the sequence. Nevertheless, since the dominant source of the error is the  $T_2^*$  process, our current sequence significantly improves the average gate fidelity

### 6.3.4 Final results and discussions

Randomized benchmarking results under different conditions are plotted in Fig. 6.7. The plot shows the expectation value of  $\sigma_z$  measured after applying  $l$  Clifford gates, in (a) linear and (b) semi-log scale. The depolarizing constant as well as the error per gate can be calculated from the decay rate of the expectation value as a function of the number of Clifford operations. The initial experimental result before implementing control improvements discussed in the previous sections is shown using  $\times$  symbols. The triangle data points demonstrate that some control improvement is gained by using 2  $\mu$ s TWT blanking delay. The semi-log plot shows that the two worst results ( $\times$  and  $\triangle$ ) deviate substantially from a single exponential fit after about 30 gates. Since the expectation value is close to zero after 30 gates, we only use first few points for fitting the data to the exponential curve. Further control enhancement is achieved by designing phase transient corrected (PTC) pulses, and the result is shown using diamond symbols. Combining longer TWT delay with PTC pulses, the error per gate is reduced to  $1.72 \pm 0.25\%$ . Although the control fidelity is improved, the non-exponential behaviour of the decay curve is still observed up to this point. This non-exponential behaviour can be explained by the  $T_2^*$  field distribution over the spin ensemble which leads to the incoherent error (See Appendix). We can intuitively interpret the non-exponential decay as a sum of single exponential decay curves with different decay rates due to different spin packets seeing different local field strengths. The Appendix details on how the incoherent error results in the non-exponential decay. After incorporating the selection sequence to increase  $T_2^*$  timescale as described in the previous

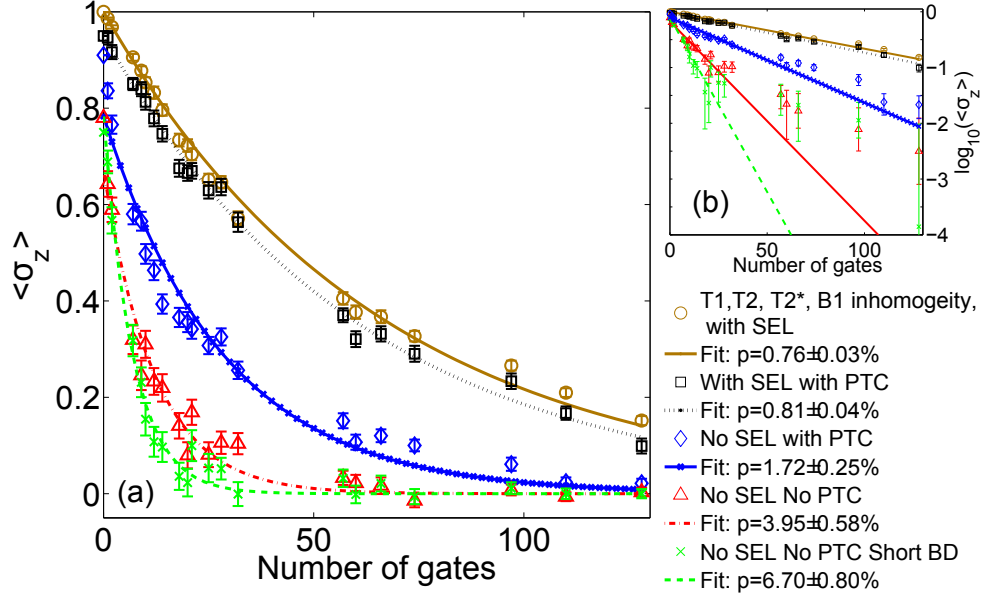


Figure 6.7: Summary of experimental results plotted in (a) linear scale and (b) semi-log scale. The expectation value  $\langle \sigma_z \rangle$  is measured after  $l$  randomized gates. Before incorporating the control improvement explained in the main text, the average error rate is above 6% ( $\times$ ). The triangles indicate the result obtained after setting the TWT blanking delay to  $2 \mu\text{s}$ , and the error probability is reduced to 3.95%. Using the phase transient corrected pulses, the error rate is further reduced to 1.72% ( $\diamond$ ). Finally, after incorporating the selection sequence for reducing  $T_2^*$  noise, the error per gate is decreased to 0.81% ( $\square$ ). The circles are the simulation results of the randomized protocol using  $T_1$ ,  $T_2$ ,  $T_2^*$  values, and  $\mathbf{B}_1$  inhomogeneity profile determined in the experiment that includes the selection sequence, assuming perfect control. The size of the error bars represents standard error of the mean averaged over 98 random sequences. In the plot legend, SEL, PTC and BD represent the selection sequence for reducing the local field distribution, phase transient corrected, and blanking delay, respectively.

section, the decay curve fits to a single-exponential curve very well. With the selection sequence, the error per gate is reduced to  $0.81 \pm 0.04\%$ . This is a remarkable enhancement compared to the initial result of 6.7%. The randomized benchmarking protocol including the selection sequence is simulated with experimentally determined values of  $T_1$ ,  $T_2$ ,  $T_2^*$  and  $\mathbf{B}_1$  distribution. The error per gate in the simulation is  $0.76 \pm 0.03\%$  and the simulation result is represented in circles in Fig. 6.7. The excellent agreement between the simulation and experimental results suggest that the contributions from the intrinsic noise and the

extrinsic control imperfections cannot be distinguished at the current level of control.

In the experimental results obtained before implementing the selection sequence for reducing field distributions (green, red, and blue data in Fig. 6.7), non-exponential behavior in the depolarizing curve is observed. In the following section, we show that the incoherent errors such as the field inhomogeneities result in the non-exponential fidelity decay.

### 6.3.5 Effect of incoherent error on the fidelity decay

Incoherent error of a quantum process is caused by classical noise, for example, a distribution over external experimental parameters [133, 134] such as  $\mathbf{B}_1$  inhomogeneity and  $T_2^*$  line-broadening. In our system, after optimizing the TWT blanking delay and using the phase transient corrected pulses,  $T_2^*$  effect remains as the dominant source of the incoherent error.  $\mathbf{B}_1$  inhomogeneity is also present, but does not critically damage the control fidelity at current level. Hence only the  $T_2^*$  noise is considered in our incoherent error discussions. In this section, we adapt the analysis presented in [15] that was used to describe  $\mathbf{B}_1$  inhomogeneity effect on the fidelity decay to explain how  $T_2^*$  gives rise to the non-exponential decay observed in our experimental (Fig. 6.7) and simulated (Fig. 6.2) results.

Due to  $T_2^*$  local field inhomogeneity across the sample, unitary errors with different strengths arise on the spins experiencing off-resonance fields. Then the fidelity of the applied pulse is averaged over the distribution. Intuitively, since the spins at different Larmor frequencies experience different unitary errors, the signal decay curve should contain multiple depolarization rates, which explains the non-exponential behavior. For more concrete analysis, we consider a single step which consists of a computational gate ( $S$ ) followed by a Pauli gate ( $P$ ) in a randomized benchmarking sequence. The superoperator describing the process can be expressed as:

$$\hat{\Lambda} = \int d\epsilon g(\epsilon) \hat{\Lambda}_\epsilon PS. \quad (6.3)$$

Here  $\epsilon$  is off-resonance frequency,  $\hat{\Lambda}_\epsilon$  is the superoperator describing the cumulative error of  $PS$  for the fraction of the system with off-resonance frequency  $\epsilon$ , and  $g(\epsilon)$  is the distribution of  $\epsilon$ .  $g(\epsilon)$  can be obtained from a frequency domain thermal state spectrum (Fig. 6.6a for example).

The cumulative error strength can be defined as

$$\xi = 1 - \frac{1}{4} |\text{Tr}(SPU_{inh}^\dagger)|^2, \quad (6.4)$$



where  $U_{inh}$  is the faulty implementation of  $S$  and  $P$  due to the local field inhomogeneity, and  $\frac{1}{4}|\text{Tr}(SPU_{inh}^\dagger)|^2$  is the gate fidelity (Hilbert–Schmidt (HS) norm) of the faulty implementation. There are 9 different error strengths  $\xi$  depending on  $S$  and  $P$ , and they are labelled from 1 to 9 in Tab. 6.1 for different combinations of  $S$  and  $P$ .

|       | X90 | -X90 | Y90 | -Y90 | Z90 | -Z90 |
|-------|-----|------|-----|------|-----|------|
| X180  | 1   | 3    | 4   | 2    | 7   | 7    |
| -X180 | 3   | 1    | 2   | 4    | 7   | 7    |
| Y180  | 2   | 4    | 1   | 3    | 7   | 7    |
| -Y180 | 4   | 2    | 3   | 1    | 7   | 7    |
| Z180  | 6   | 6    | 6   | 6    | 8   | 8    |
| I     | 5   | 5    | 5   | 5    | 9   | 9    |

Table 6.1: Gate-dependent cumulative error types for different combinations of computational gates  $S$  (columns) and Pauli gates  $P$  (rows) labelled from 1 to 9. The errors are grouped to 9 types according to their strengths defined in Eq. 6.4.

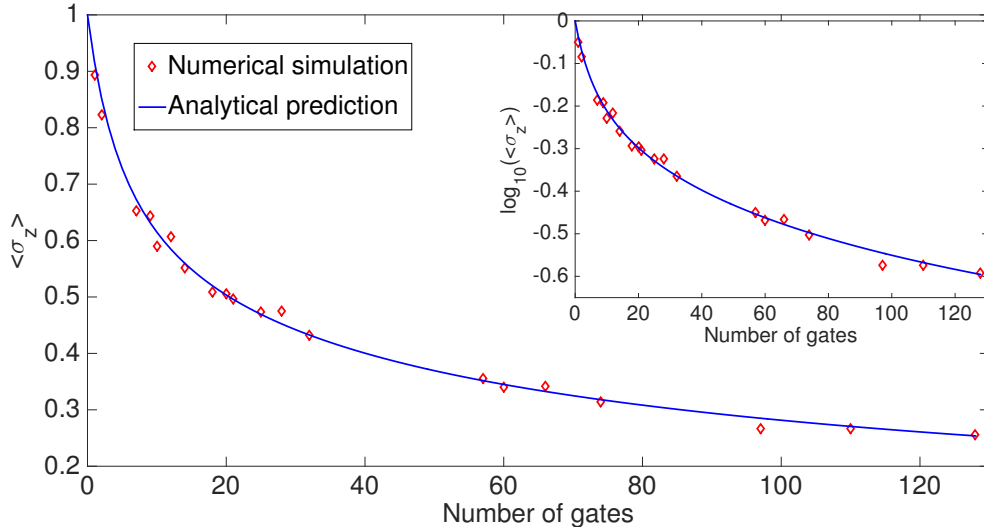


Figure 6.8: Comparison between the numerically calculated prediction using Eq. 6.7 (solid) and the realistic simulation averaged over 420 randomized benchmarking pulse sequences ( $\diamond$ ). Excellent agreement between the two is observed.  $T_1$  and  $T_2$  processes are not taken into account.

It is proven in [20, 119, 120] that the cumulative effect of the gate dependent errors in

the randomized benchmarking can still be described as a depolarizing channel as long as the gate dependence is weak enough. Consequently, the zeroth-order fitting model in [20, 120] (equivalently, the single-exponential decay model) can be used for fitting the observable fidelity decay. We will not discuss in detail the validity of using the zeroth-order fitting in the present case, but from the simulation results shown in Fig. 6.8, we can conclude that the zeroth-order fitting model is a very good approximation in our case. Therefore, upon averaging over random gate sequences,  $\hat{\Lambda}_\epsilon$  in Eq. 6.3 forms a depolarizing channel  $\hat{\Lambda}_{\epsilon,ave}$  with the depolarizing factor  $p_\epsilon$ .  $p_\epsilon$  is a weighted sum of the depolarizing factors of different errors associated with  $\epsilon$ . The depolarizing factors  $p_i$  where  $i = 1, \dots, 9$  labels different error types  $\xi$  can be calculated as [119]:

$$p_i = \frac{4 - |\text{Tr}(SPU_{inh}^\dagger)|^2}{3}. \quad (6.5)$$

Then the total depolarizing factor  $p_\epsilon$  is the weighted sum of  $p_i$ :

$$p_\epsilon = \sum_{i=1}^9 w_i p_i, \quad (6.6)$$

where  $w_i$  is the probability for the error type  $i$  to occur, and their values are 1/9, 1/9, 1/9, 1/9, 1/9, 2/9, 1/18, 1/18. Finally, by averaging over the distribution of  $\epsilon$ , the expression for the channel constructed from  $n$  random gates can be obtained as:

$$\hat{\Lambda}_{ave}(n) = \int d\epsilon g(\epsilon) \hat{\Lambda}_{\epsilon,ave}^n, \quad (6.7)$$

where  $\hat{\Lambda}_{\epsilon,ave}^n(\rho) = (1 - p_\epsilon)^n \rho$  and  $\rho$  is the deviation density matrix or the traceless part of the full density matrix. Therefore, the fidelity decay (in our case, the decay of the expectation value of  $\sigma_z$ ) is the sum of multiple exponential decays weighted with the distribution function  $g(\epsilon)$ .

Using experimentally measured values for  $g(\epsilon)$ , we compare in Fig. 6.8 the decay curve numerically calculated from Eq. 6.7 with the curve obtained by simulating randomized benchmarking sequences. The evaluation of Eq. 6.7 is carried out numerically since  $U_{inh}$  is generated by a time-dependent Hamiltonian with two non-commuting terms,  $\sigma_z$  term representing the off-resonance effect and  $\sigma_{x,y}$  terms for the external control. For the  $S$  and  $P$  gates, 35 ns gaussian pulses with 1 ns time steps are used. Two decay curves agree very well, indicating the  $T_2^*$  incoherent error is responsible for the non-exponential behavior of the fidelity decay. Furthermore, in the experimental data, the decay curve fits very well to a single exponential function within the error bar when  $T_2^*$  is extended using the selection sequence (squares in Fig. 6.7). Therefore, we conclude that the non-exponential fidelity decay can be explained by the  $T_2^*$  error.

## 6.4 Future work

The average gate fidelity can be further enhanced from current level by designing a new selection sequence that is more effective at reducing the local field inhomogeneities, perhaps both  $T_2^*$  and  $\mathbf{B}_1$  field distribution. The error per gate can also be further reduced by applying the benchmarking protocol to an ESR sample with longer  $T_2^*$ ,  $T_2$ , and  $T_1$ . One promising candidate is nitrogen-incarcerated fullerene (N@C<sub>60</sub>) dissolved in carbon disulfide [112, 135] for which extremely long relaxation times of 80  $\mu\text{s}$   $T_2$  and 120  $\mu\text{s}$   $T_1$  have been reported in room-temperature. Since the sample is in the liquid state, there is no  $g$  anisotropy which contributed to having short  $T_2^*$  of the quartz powder sample. On the other hand, the quartz sample with less irradiation dose can possess longer  $T_2$  at the cost of decreased signal to noise ratio. Once the relaxation errors are suppressed to the level where the extrinsic control noise dominates, it will be interesting to study the performance of different amplifier technologies for quantum control. The current TWT amplifier can be replaced with a solid state amplifier and the randomized benchmarking protocol can be carried out to compare and quantify their performances.

# Chapter 7

## Testing the feasibility of heat bath algorithmic cooling in the electron-nuclear spin system

### 7.1 Introduction

Purification of quantum states is essential for realizing fault tolerant quantum information processors. The procedure is needed not only for initializing the physical system for quantum algorithms, but also to dynamically supply fresh pure ancilla qubits for error correction. For quantum computation models that utilize an ensemble of identical systems such as NMR or ESR, acquisition of nearly pure quantum states in a scalable manner is extremely challenging. The polarization can be increased by decreasing temperature or increasing the strength of the static magnetic field as suggested in Eq. 2.10, but this way of achieving high polarization is experimentally costly. Moreover, as mentioned in Sec. 2.2, at low temperature, the nuclear  $T_1$  relaxation time scale becomes undesirably long, making the wait time for resetting to the thermal state impractically long. A potential solution is algorithmic cooling (AC), a protocol which purifies qubits by removing entropy from subset of them, while increasing the entropy of the rest [136, 137]. An explicit way to implement this idea in quantum computations was given by Schulman et al. [138]. They showed that it is possible to reach polarization of order unity using only a number of qubits which is polynomial in the initial polarization. However, their method was limited by the Shannon bound, which imposes a constraint on the entropy compression step in closed systems. This idea was further improved by adding contact with a heat bath to pump

entropy out of the system and transfer it into the heat bath [24], a process known as Heat Bath Algorithmic Cooling (HBAC). Based on this idea, many practical cooling algorithms have been designed [25, 28, 139]. In short, HBAC purifies qubits by applying alternating rounds of entropy compression and pumping out entropy from the system of interest to a thermal bath.

The Partner Pairing Algorithm (PPA) [28] is known to be an optimal way to implement HBAC provided three or more qubits and when there is one reset qubit that thermalizes to the bath polarization  $\epsilon_b$  much faster than the relaxation rate of the rest of the system qubits. In this scenario, polarizing 1 system qubit beyond  $\epsilon_b$  can be achieved by recurrently applying the entropy compression step and the refresh step. The compression is a permutation that rearranges the diagonal elements of the density matrix in non-increasing order so that the polarization of the first (target) qubit increases while the reset qubit polarization decreases. During the refresh step, the reset qubit thermalizes to the bath temperature and the overall entropy of the system is reduced. Repeating the above procedure, the polarization of the first qubit  $\epsilon_1$  asymptotically approaches a threshold value. The general expression for the maximum threshold polarization of the target qubit was worked out recently in [140] by solving the polarization of the steady state in the cooling limit. The cooling limit is reached when there is no operation that can compress the entropy of the computational qubits, or equivalently, when the diagonal elements of the total state are already sorted in non-increasing order [140, 141]. The maximum threshold polarization derived in [140] is

$$\epsilon_{max} = \frac{(1 + \epsilon_b)^{md} - (1 - \epsilon_b)^{md}}{(1 + \epsilon_b)^{md} + (1 - \epsilon_b)^{md}}, \quad (7.1)$$

where  $m$  is the number of reset qubits that are brought to thermal contact with the heat bath of polarization  $\epsilon_b$ , and  $d$  is the dimension of the computational qubits onto which the entropy is compressed during the unitary compression step. When  $m = 1$ , the threshold polarization can be reduced to more compact form in certain cases:  $\epsilon_{max} = \epsilon_b 2^{n-2}$  if  $\epsilon_b \ll 2^{-n}$ , and arbitrarily high polarization if  $\epsilon_b \gg 2^{-n}$ , where  $n$  is the number of system qubits including the target qubit for cooling [28, 41].

In this chapter, we investigate experimental feasibility of HBAC using realistic electron-nuclear coupled spin systems in single crystal form that can be readily prepared in the laboratory. Moving to ESR from NMR provides the boost in the polarization of a nuclear spin about three orders of magnitude (see Sec. 1). Next, through HBAC, the polarization can be improved further. Demonstrating the experimental feasibility of HBAC in the electron-nuclear system for achieving nuclear polarization beyond Shannon bound is a significant milestone towards implementation of multiple rounds of QEC.

## 7.2 Simulating HBAC using five hyperfine spin qubits

The stable malonyl radical  $\dot{\text{C}}\text{H}(\text{COOH})_2$  has been extensively studied by electron spin resonance (ESR) studies of gamma-irradiated single crystals. The hyperfine tensors of the  $\alpha$ -proton and of the  $^{13}\text{C}$ -labeled methylene carbon were previously published [142–144]. However, the hyperfine tensors of the  $^{13}\text{C}$ -labeled carboxyl carbons have not yet been reported. The carboxyl tensors are in fact different from each other owing to different dihedral angles of COOH relative to the C-C-C plane to accommodate the hydrogen bonding network; the carboxyl group with a larger dihedral angle has a slightly weaker carbon hyperfine coupling. Including these two carboxyl carbons and assuming they are spectroscopically distinct, the molecule can in principle realize a 5-qubit ensemble quantum information processor, with 1 electron and 4 nuclear spins. The nuclei are strongly hyperfine coupled to the electron and can be controlled either by exploiting the anisotropic part of the hyperfine interaction (AHC) or by using pulsed ENDOR techniques. The electron connects the nuclei to a heat-bath with a much colder effective temperature determined by the electron’s thermal spin polarization.

By accurately determining the full spin Hamiltonian and performing realistic algorithmic simulations, we show that an experimental demonstration of heat-bath algorithmic cooling beyond the Shannon bound is feasible in both 3-qubit and 5-qubit variants of this spin system. Similar techniques could be useful for polarizing nuclei in molecular or crystalline systems that allow for non-equilibrium optical polarization of the electron spin.

### 7.2.1 Sample preparation

Malonic acid,  $\text{CH}_2(\text{COOH})_2$ , crystallizes with a triclinic unit cell and belongs to the  $\text{P}\bar{1}$  space group [145, 146] at temperatures above 47 K. At lower temperatures, a structural phase transition occurs that has been discussed previously [147–149]. Above 47 K, there are two molecules per unit cell related by inversion symmetry, making them magnetically equivalent. We denote the methylene and carboxylic carbons as  $\text{C}_m$  and  $\text{C}_{1,2}$ , respectively. A schematic of the radical, obtained by removing one of the methylene protons, is shown in Fig. 7.1. The unpaired electron is of  $p$ -orbital character [143, 150, 151]. Malonic acid powder with all possible  $^{13}\text{C}$  isotopic labelling configurations was purchased either from Sigma Aldrich or Cambridge Isotopes. Single crystals were grown by slow evaporation from aqueous solutions at room temperature. To form radicals, crystals were irradiated to a dose of about 2 kGy at room temperature with  $\gamma$ -rays from a cobalt-60 pencil. Annealing at  $60^\circ$  for 12-15 hours following the irradiation suppresses ESR signals from all other radical

species except for the most stable radical,  $\dot{\text{C}}\text{H}(\text{COOH})_2$  [150]. Depending on the  $^{13}\text{C}$  labelling configuration, 2, 3, 4 or 5 qubit samples are obtained as (e-H), (e-H- $\text{C}_m$ ), (e-H- $\text{C}_{1,2}$ ) and (e-H- $\text{C}_m$ - $\text{C}_{1,2}$ ) respectively, where e denotes the electron spin. The  $\beta$ -protons of the carboxyl groups contribute to ESR line broadening and in some orientations can give rise to observable splittings [152]. However, due to weak hyperfine coupling ( $< 6$  MHz isotropic coupling [152]) they are not useful as qubits.

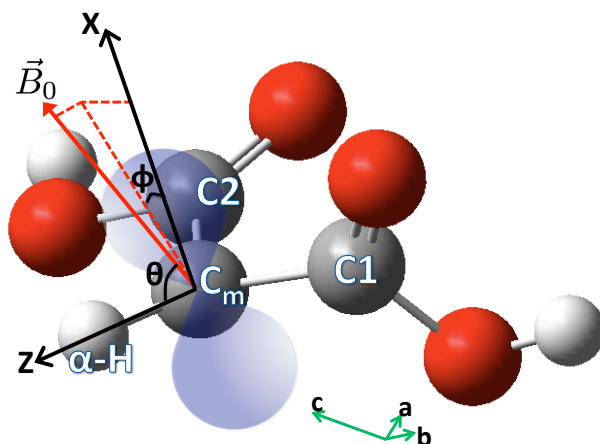


Figure 7.1: Molecular structure of  $\dot{\text{C}}\text{H}(\text{COOH})_2$  with unpaired electron density distribution schematically represented by the blue shaded region.  $x$  and  $z$  are two principal axes of the  $\alpha$ -proton hyperfine tensor, with  $z$  along the  $\text{C}_m$ - $\alpha$ -proton interatomic vector and  $x$  along the cylindrical symmetry axis of the electronic  $p$ -orbital. The  $y$  axis, not shown, is nearly parallel to the  $\text{C}_1$ - $\text{C}_2$  interatomic vector. The direction of the static field  $\vec{B}_0$  can be described using polar angle  $\theta$  and azimuthal angle  $\phi$  in the principal axis system of the  $\alpha$ -proton hyperfine tensor. The directions of the crystallographic axes  $a$ ,  $b$  and  $c$  with respect to the molecular structure are illustrated by the green axes [145, 153].  $c$  lies very close to the  $y$  axis of the  $\alpha$ -proton principal axis system. The direction cosines of  $a$ ,  $b$  and  $c$  in the  $\alpha$ -proton principal axis system are (0.1426, -0.6588, 0.7387), (-0.9729, -0.1888, 0.1335) and (0.0222, 0.9969, -0.0752), respectively.

## 7.2.2 Five-qubit malonic acid spin Hamiltonian determination

In this section, the electron  $g$  tensor and the hyperfine tensors for the  $\alpha$ -proton and three carbons in malonic acid is reported. The tensors are extracted using the method presented in Sec. 4.3.

## Continuous-wave ESR results

The tensor extraction model relies on two assumptions: the three planes of measurement are mutually non-parallel and the axis of the rotation to go from one to another belongs to both planes. The orientation experiments were designed to ensure that both assumptions are satisfied. In each of the three non-parallel planes, we took 24, 9 and 46 measurements with  $8^\circ$ ,  $20^\circ$  and  $4^\circ$  angle steps for the methylene-labeled, carboxyl-labeled and fully-labeled MA samples, respectively. The methylene-labeled data was used to extract the  $\alpha$ - $^1\text{H}$  and  $^{13}\text{C}_m$  tensors; the carboxyl-labeled data was used to extract the  $^{13}\text{C}_{1,2}$  (average) tensor, and the fully-labeled data was used to confirm all the tensors by fitting with simulated spectra. As discussed previously in Sec. 4.3, we need only to detect the spectral positions of the allowed transitions, which can be distinguished from forbidden transition peaks because of their larger intensities. Each measured spectrum is fit to a set of allowed transition peaks defined by their amplitude, frequency and a common line width. The peak positions for all measurements in one plane give a set of trajectories for that plane, from which we obtained the dependence of  $g$  and  $A^n$  on  $\theta$ . Doing this in all three planes allows extraction of the  $g$ -factor tensor  $\mathbf{g}$  and hyperfine tensors  $\mathbf{A}^n$  by solving Eq. 4.18 and Eq. 4.21. After this, we used the method of least square fitting to optimize  $\mathbf{g}$  and  $\mathbf{A}^n$  by minimizing the difference between the experimental peak trajectories and the simulated trajectories. It should be noted that in X-band ESR the nuclear Zeeman energy for  $^1\text{H}$  is about 15 MHz, which is comparable to the hyperfine coupling of  $\alpha$ - $^1\text{H}$  in some orientations. Therefore, in order to obtain more accurate  $\mathbf{A}^n$  tensors, we took into account the nuclear Zeeman energy when generating the simulated peak trajectories in the optimization procedure. The only noticeable difference from including this energy was for the  $\alpha$ - $^1\text{H}$ , as expected.

The  $\mathbf{g}$ ,  $\mathbf{A}^{\text{H}}$ ,  $\mathbf{A}^{\text{C}^m}$  and  $\mathbf{A}^{\text{C}_{1,2}}$  tensors were determined from continuous wave (CW) ESR spectra as described above, and are listed in Tab. 7.1. The hyperfine tensors of  $\text{C}_1$  and  $\text{C}_2$  are similar and require ENDOR measurements to be distinguished (see next section). From the ESR data we obtained an average hyperfine tensor describing  $\text{C}_1$  and  $\text{C}_2$ , denoted as  $\mathbf{A}^{\text{C}_{1,2}}$ . Negative signs of the principal values for  $\mathbf{A}^{\text{C}_{1,2}}$  were determined by a quantum chemical calculation using the Gaussian program [154]. Similar to the case of  $\alpha$ - $^1\text{H}$  [143, 150, 151], the negative principal values are due to a negative spin density on  $\text{C}_1$  and  $\text{C}_2$ . The results for  $\mathbf{g}$ ,  $\mathbf{A}^{\text{H}}$  and  $\mathbf{A}^{\text{C}^m}$  are consistent with the published results in [142–144, 149, 150, 153]. The simulated ESR peak trajectories generated from the tensors in Tab. 7.1 are in excellent agreement with the experimental data, as the examples in Fig. 7.2 and Fig. 7.3 demonstrate.



|  |                   | Direction cosines to A <sup>H</sup> principal axis |         |         |
|--|-------------------|--|---------|---------|
|  |                   | X  | Y       | Z       |
| g <sub>xx</sub>                            | 2.00250 ± 0.00038 | -0.1657  | 0.9779  | 0.1272  |
| g <sub>yy</sub>                            | 2.00373 ± 0.00037 | -0.9811  | -0.1766 | 0.0797  |
| g <sub>zz</sub>                            | 2.00417 ± 0.00036 | 0.1004   | -0.1115 | 0.9887  |
| A <sub>xx</sub> <sup>H</sup>               | -26.6 ± 2.8       | 1  | 0       | 0       |
| A <sub>yy</sub> <sup>H</sup>               | -56.0 ± 0.7       | 0  | 1       | 0       |
| A <sub>zz</sub> <sup>H</sup>               | -91.5 ± 0.6       | 0  | 0       | 1       |
| A <sub>xx</sub> <sup>Cm</sup>              | 24.5 ± 1.0        | 0.0696   | -0.0019 | 0.9976  |
| A <sub>yy</sub> <sup>Cm</sup>              | 43.0 ± 1.3        | 0.9962   | 0.0530  | -0.0694 |
| A <sub>zz</sub> <sup>Cm</sup>              | 212.3 ± 0.6       | -0.0528  | 0.9986  | 0.0056  |
| A <sub>xx</sub> <sup>C<sub>1,2</sub></sup> | -36.1 ± 0.3       | 0.0627   | 0.0082  | 0.9980  |
| A <sub>yy</sub> <sup>C<sub>1,2</sub></sup> | -39.3 ± 0.3       | 0.9805   | -0.1870 | -0.0601 |
| A <sub>zz</sub> <sup>C<sub>1,2</sub></sup> | -40.6 ± 0.3       | 0.1862   | 0.9823  | -0.0198 |

Table 7.1: Electronic g-factor and hyperfine coupling tensors determined from CW ESR measurements (principal hyperfine values are given in MHz). Principal values are given in the left column, while direction cosines relative to the principle axis system of the  $\alpha$ -proton are given in the three right columns. The uncertainties reflect a 90% confidence interval. The tensor A<sup>C<sub>1,2</sub></sup> gives an estimate of the average of A<sup>C<sub>1</sub></sup> and A<sup>C<sub>2</sub></sup>.

## Continuous-wave ENDOR results

In this section we describe the use of ENDOR, which has higher spectral resolution than ESR, to extract the distinct tensors describing A<sup>C<sub>1</sub></sup> and A<sup>C<sub>2</sub></sup>. From Eq. 4.23 we see that for each nucleus there are two resonant frequencies  $\nu_-$  and  $\nu_+$ . However, in experiments we found that one or sometimes two of the four peaks of C<sub>1</sub> and C<sub>2</sub> were obscured by the large peaks around 14.5 MHz that come from <sup>1</sup>H spins which have small hyperfine couplings with the electron radical (Fig. 7.4). The two higher frequency peaks (in the range of 20 – 25 MHz) were clearly resolved in all measured orientations. Judging from the sign of A<sup>C<sub>1,2</sub></sup>, we infer that these two peaks correspond to the  $\nu_+^{C_1}$  and  $\nu_+^{C_2}$  frequencies, with

$$(\nu_+^n)^2 = (\nu_I^n)^2 + \frac{1}{4g^2}(l_\alpha \Gamma_{\alpha\beta}^{A^n} l_\beta) - \frac{\nu_I^n}{g}(l_\alpha (\mathbf{g} \cdot \mathbf{A}^n)_{\alpha\beta} l_\beta) = (\nu_I^n)^2 + \frac{1}{g^2}(l_\alpha \mathbf{K}_{\alpha\beta}^{A^n} l_\beta), \quad (7.2)$$

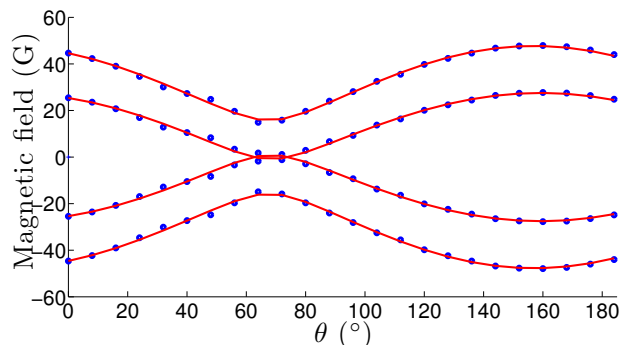


Figure 7.2: Comparison between the simulated ESR peak trajectories (red lines) and the experimental data (blue dots) of the methylene  $^{13}\text{C}$ -labeled sample in one of the planes measured. The direction cosines of the normal of this plane are  $(-0.3376, 0.9405, 0.0391)$  in the principal axis system of  $\mathbf{A}^{\text{H}}$ .

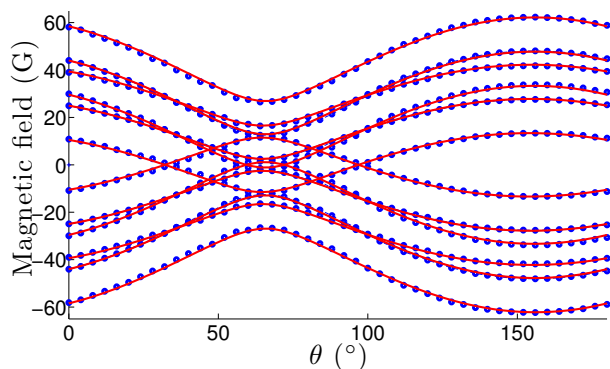


Figure 7.3: Comparison between the simulated ESR peak trajectories (red lines) and the experimental data (blue dots) of the per- $^{13}\text{C}$ -labeled sample in one of the planes measured. The direction cosines of the normal of this plane are  $(-0.3678, 0.9287, -0.0483)$  in the principal axis system of  $\mathbf{A}^{\text{H}}$ .

where  $n = 1, 2$  for  $\text{C}_1$  and  $\text{C}_2$  and  $\mathcal{K}^{\text{A}^n} = \Gamma^{\text{A}^n}/4 - \nu_I^n g \mathbf{g} \cdot \mathbf{A}^n$ . Using only the  $\nu_+$  frequencies requires a different approach than directly using Eq. 4.24. Instead of measuring the orientation dependence of  $g((\nu_-^n)^2 - (\nu_+^n)^2)/2\nu_I^n$ , we measured that of  $g^2((\nu_+^n)^2 - (\nu_-^n)^2)$  in three non-parallel planes to extract  $\mathcal{K}^{\text{A}^n}$  using Eq. 7.2, and then used  $\mathcal{K}^{\text{A}^n}$  to calculate  $\text{A}^{\text{C}_1}$  and  $\text{A}^{\text{C}_2}$ . In each plane, we took 9 measurements with  $20^\circ$  angle steps for the carboxyl-labeled MA sample. It should be mentioned that by using Eq. 7.2 to obtain  $\text{A}^{\text{C}_1}$  and  $\text{A}^{\text{C}_2}$ , we neglected the anisotropy of  $\mathbf{g}$ . For the hyperfine tensors, this approximation causes a

difference in the principal values less than the experimental uncertainty of  $\sim 0.1$  MHz. The experimentally determined  $A^{C_1}$  and  $A^{C_2}$  tensors are listed in Tab. 7.2.

|                |                 | Direction cosines to $A^H$ principal axis |         |         |
|----------------|-----------------|---|---------|---------|
|                |                 | X   | Y       | Z       |
| $A_{xx}^{C_1}$ | $-37.0 \pm 0.1$ | -0.5310                                   | -0.0010 | 0.8474  |
| $A_{yy}^{C_1}$ | $-40.5 \pm 0.1$ | 0.8452                                    | -0.0724 | 0.5295  |
| $A_{zz}^{C_1}$ | $-43.6 \pm 0.1$ | 0.0608                                    | 0.9974  | 0.0392  |
| $A_{xx}^{C_2}$ | $-34.0 \pm 0.1$ | -0.3477                                   | -0.0449 | -0.9365 |
| $A_{yy}^{C_2}$ | $-37.4 \pm 0.1$ | -0.2478                                   | 0.9677  | 0.0456  |
| $A_{zz}^{C_2}$ | $-39.6 \pm 0.1$ | -0.9043                                   | -0.2479 | 0.3476  |

Table 7.2: Hyperfine coupling tensors for  $A^{C_1}$  and  $A^{C_2}$  determined from CW ENDOR measurements (principal hyperfine values are given in MHz). Principal values are given in the left column, while direction cosines relative to the principle axis system of the alpha-proton are given in the three right columns. The uncertainties reflect a 90% confidence interval.

Fig. 7.4 and Fig. 7.5 show the experimental ENDOR and ESR spectra, together with the simulated spectra generated using the tensors given in Tab. 7.2, for the carboxyl-labeled sample when the orientation of the magnetic field is  $(0.6156 -0.7179 -0.3249)$  in the principal axis system of  $A^H$ . In Fig. 7.4, we can see that in this orientation there are three observable peaks of  $C_1$  and  $C_2$ , while the peak with the lowest frequency is obscured by the  $^1H$  peaks around 14.5 MHz. Excellent agreement between experiment and simulation can be seen in these examples, and a similar level of agreement was found for spectra in all measured orientations, indicating that the tensors in Tab. 7.2 are accurate.

### 7.2.3 Malonic acid orientation selection

#### Orientation criteria for AHC

The criteria for choosing the orientation for achieving optimal control in AHC scheme are discussed in Sec. 4.6.1. For the optimal orientation search,  $B_0$  is fixed at  $10 \text{ GHz}/\gamma_e \approx 3568$  G and  $\theta$  and  $\phi$  that appear in Fig. 7.1 are varied at  $1^\circ$  angle steps. The maximum values of  $\tan(\eta^n)$  are 1.3, 0.14, 0.016, and 0.017 for H,  $C_m$ ,  $C_1$ , and  $C_2$ , respectively. Roughly

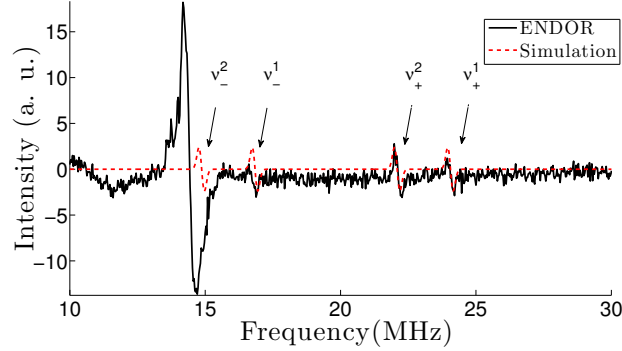


Figure 7.4: Comparison between the simulated ENDOR spectrum (red line) and the experimental spectrum (black line) of the carboxyl  $^{13}\text{C}$ -labeled sample. The orientation of magnetic field is  $(0.6156, -0.7179, -0.3249)$  in the principal axis system of  $\mathbf{A}^{\text{H}}$ . In the area around 14.5 MHz, there are large peaks which come from the distant  $^1\text{H}$  spins that have small hyperfine couplings with the electron radical. The ENDOR peak for  $\text{C}_2$  with the frequency  $\nu_-^2 = 14.9$  MHz is obscured by these  $^1\text{H}$  peaks. The other three ENDOR peaks for  $\text{C}_1$  and  $\text{C}_2$  with frequencies  $\nu_+^1 = 24.1$  MHz,  $\nu_+^2 = 22.1$  MHz and  $\nu_-^1 = 16.8$  MHz are clear.

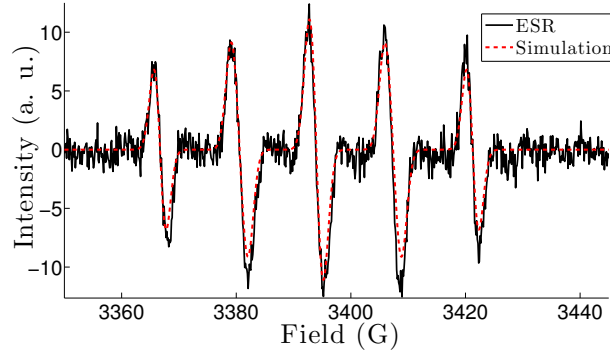


Figure 7.5: Comparison between the simulated ESR spectrum (red line) and the experimental spectrum (black line) of the carboxyl  $^{13}\text{C}$ -labeled sample. The orientation of magnetic field is  $(0.6156, -0.7179, -0.3249)$  in the principal axis system of  $\mathbf{A}^{\text{H}}$ . Using the tensors given in Tab. 7.2, the ESR peak positions are reproduced well and the line broadening due to the hyperfine couplings of the two carboxyl carbons fits well in all measured orientations.

speaking, since  $\tan(\eta^{\text{H}}) \lesssim 1$  and  $\tan(\eta^{\text{C}}) \ll 1$ , the duration of a GRAPE optimal control [72] pulse to accomplish an arbitrary unitary operation will scale as  $1/\tan(\eta^n)$ . We have

measured a nearly temperature-independent electron spin dephasing time  $T_2^e \sim 5 \mu\text{s}$  in this system, due to hyperfine coupling with distant protons, and their mutual dipolar interaction induced dynamics. Given that the shortest GRAPE pulses for arbitrary gates involving H require  $\sim 500$  ns, it is clear that high fidelity control of  $C_1$ , and  $C_2$  via AHC is simply not possible in this system. Moreover, the 5-qubit system contains 80 ESR resonances over a maximum spectral range of 250 MHz, consisting of 16 allowed and 64 forbidden transitions. Consequently, we find  $\max_{\theta, \phi} \{\min(\vec{\delta})\} = 1.4$  MHz, where the elements of  $\vec{\delta}$  are the distances between any two ESR transitions and  $\max_{\theta, \phi} \{\}$  indicates the maximization over all sets of  $\{\theta, \phi\}$  with  $1^\circ$  angle step. In practice, it only makes sense therefore to focus on the 3-qubit sample (e-H- $C_m$ ) for optimizing AHC control. Nonetheless, for completeness we show in Tab. 7.3 the best possible orientation for the 5-qubit system given these criteria.

For the 3-qubit sample, there are 4 allowed transitions and 8 forbidden transitions. It is still not possible to find orientations where  $\min(\vec{\delta}) \geq 12$  MHz, rather we find that  $\max_{\theta, \phi} \{\min(\vec{\delta})\} = 7.6$  MHz. We focus on orientations that satisfy  $\min(\vec{\delta}) \geq 6$  MHz, and then choose an orientation in which  $\tan(\eta^H)$  and  $\tan(\eta^{C_m})$  are both as large as possible. The forbidden transition rates at this orientation are 0.1418 and 0.1203 for H and  $C_m$ , respectively, and  $\min(\vec{\delta}) = 6.1$  MHz. These results are summarized in the table below:

|            |                       | $A_{zz}^n(\text{MHz}), B^n(\text{MHz}), \tan(\eta^n)$ |                             |                                |                                |                               |
|------------|-----------------------|---|-----------------------------|--------------------------------|--------------------------------|-------------------------------|
|            | $\theta, \phi$        | H   | $C_m$                       | $C_1$                          | $C_2$                          | $\min(\vec{\delta})$<br>(MHz) |
| 5<br>qubit | $54^\circ, 123^\circ$ | -<br>62.56,<br>23.67,<br>0.1948                       | 121.23,<br>90.54,<br>0.0303 | -<br>40.03,<br>3.27,<br>0.0161 | -<br>37.29,<br>1.63,<br>0.0093 | 1.1                           |
| 3<br>qubit | $29^\circ, 13^\circ$  | -<br>76.60,<br>27.07,<br>0.1418                       | 29.21,<br>17.78,<br>0.1203  |                                |                                | 6.1                           |

Table 7.3: Optimal orientations for AHC experiment with the fully-labeled (5 qubit) and  $C_m$ -labeled (3 qubit) malonyl radical, and corresponding values of hyperfine coupling constants  $A_{zz}^n$  and  $B^n$ , and the quantity  $\tan(\eta^n)$  characterizing the controllability of nuclear spin  $n$ .  $\min(\vec{\delta})$  represents the minimum separation between ESR transitions.

## Orientation criteria for ENDOR

The disadvantage of ENDOR control is that the RF pulses are typically of order  $\gamma_e/\gamma_n \sim 10^3$  times slower than the microwave control of electron spin. This severely limits the ability to perform arbitrary quantum algorithms within the electron  $T_2^e$ , however, in algorithmic cooling the electron spin is always in an eigenstate during the nuclear rotations so that electronic dephasing is not an issue. Since the hyperfine tensors of  $C_1$  and  $C_2$  are very similar, they cannot be separately addressed by microwave pulses, but only with RF pulses. At first glance, this seems to forbid selective swap gates between the electron and  $C_1$  or  $C_2$ , which is an essential step for HBAC. Fortunately, we show in Sec. 7.2.5 that it is possible to realize a pulse sequence combined with the electron refresh step in order to polarize both  $C_1$  and  $C_2$  to the bath polarization, as long as all NMR transitions can be addressed selectively, and the nuclei H and  $C_m$  are separately addressable by microwave pulses. The RF pulse durations are typically on the order of tens of  $\mu\text{s}$ , corresponding to

|            |                          | $A_{zz}^n(\text{MHz}), B^n(\text{MHz}), \tan(\eta^n)$ |                             |                           |                          |       |                               |
|------------|--------------------------|---|-----------------------------|---------------------------|--------------------------|-------|-------------------------------|
|            |                          | $\theta, \phi$  | H                           | $C_m$                     | $C_1$                    | $C_2$ | $\min(\vec{\delta})$<br>(MHz) |
| 5<br>qubit | $95.8^\circ, 86.3^\circ$ | -   | -                           | -                         | -                        | -     | 6                             |
|            |                          | 56.36,<br>3.59,<br>0.048                              | 209.48,<br>22.51,<br>0.0039 | 43.50,<br>0.70,<br>0.0029 | 37.56,<br>0.70,<br>0.004 |       |                               |
| 3<br>qubit | $90^\circ, 90^\circ$     | -56.0,<br>0, 0  | 211.83,<br>8.98,<br>0.0015  |                           |                          |       | 56                            |

Table 7.4: Optimal orientations for the ENDOR control scheme with fully-labeled (5 qubit) and  $^{13}\text{C}_m$ -labeled (3 qubit) molecules, corresponding values of hyperfine coupling constants  $A_{zz}^n$  and  $B^n$ , and the quantity characterizing forbidden transition rates  $\tan(\eta^n)$  for nuclear spin  $n$ . In these orientations, the NMR transitions are well separated for high fidelity control; the minimum distances between two NMR transition frequencies are 1.8 MHz and 7.6 MHz for the 5-qubit and 3-qubit systems, respectively. Here,  $\min(\vec{\delta})$  represents the minimum separation between allowed ESR transitions.

excitation bandwidths less than 100 kHz. Thus, for the 5 qubit sample, we search for an

orientation in which all NMR transition frequencies are at least 500 kHz apart, and all allowed ESR transition frequencies with the exception of the  $C_1$  and  $C_2$  resonances are at least 12 MHz apart. Then among this set, we select one orientation in which  $\tan(\eta)$  is as small as possible for all nuclei. The optimal orientation for the fully-labeled molecule and relevant parameters in that orientation is given in Tab. 7.4. The minimum distance between ESR transitions in this orientation is 6 MHz due to  $C_1$  and  $C_2$ . All other ESR transitions are at least 13 MHz apart from each other. Some forbidden transitions may be very close to the ESR allowed frequencies, but this is not a serious issue since the forbidden transitions can be ignored when  $\tan(\eta)$  is small.

For the 3-qubit molecule, it is relatively easy to find orientations in which the allowed ESR transitions are separated by at least 12 MHz. Among that set, an optimal orientation is chosen for which  $\tan(\eta)$  is minimized for both H and  $C_m$ . The results are summarized in Tab. 7.4.

### 7.2.4 Simulating 3-qubit HBAC

The quantum circuit for 3-qubit HBAC is shown in the top part of Fig. 7.6. Here, the electron is chosen as the bath qubit whose polarization is  $\epsilon_b \approx 8 \times 10^{-4}$  at room temperature and at  $\mathbf{B}_0 = 10 \text{ GHz}/\gamma_e \approx 3568 \text{ G}$ . Under these conditions,  $^1\text{H}$  and  $^{13}\text{C}$  equilibrium polarizations are about 660 and 2620 times smaller than the electronic polarization. For the 3-qubit PPA with completely mixed initial states, the first two entropy compression steps are polarization transfers (swaps) from the reset qubit to the 1<sup>st</sup> (target) and the 2<sup>nd</sup> qubits. After the 3<sup>rd</sup> gate operation (3-qubit compression), the target qubit polarization is higher than the bath polarization. These steps complete one round of the 3-qubit PPA. In theory, the first round of the 3-qubit PPA boosts the polarization of one nuclear spin to  $1.5\epsilon_b - 0.5\epsilon_b^3 \approx 1.5\epsilon_b$  for small  $\epsilon_b$ . By repeated application of these steps, the nuclear spin is asymptotically polarized to  $2\epsilon_b$ . Note that starting from the 2<sup>nd</sup> round, only one polarization swap gate is used since the target nucleus is already polarized above the bath polarization.

### Anisotropic hyperfine control

The crystal orientation used for the 3-qubit experiment using the AHC method is shown in Tab. 7.3. In this orientation, the forbidden transition rate of  $C_m$  in the presence of a resonant microwave field is weaker than that of the  $\alpha$ -proton. Consequently, the  $C_m$  polarization decays slower than that of proton during electron reset. Therefore  $C_m$  is chosen

as the target qubit for cooling. The electron reset is done by waiting for  $4.2 \times T_1^e$  ( $T_{1,2}^e$  denotes the electronic  $T_{1,2}$  throughout the text) in order to bring the electron polarization to about 98.5% its thermal polarization. A longer waiting time, e.g.  $5 \times T_1^e$ , brings the electron polarization to above 99%, however, we find that the wait time of  $4.2 \times T_1^e$  is optimal since nuclear spin polarizations decay during electron reset (due to the anisotropic hyperfine interaction). The microwave field swap and compression gates are designed using the gradient ascent pulse engineering (GRAPE) algorithm [72]. The GRAPE pulse lengths are 840 ns for the swap gates and 900 ns for the 3-qubit compression gate. The pulses are optimized over the electron Zeeman Hamiltonian distribution in order to be robust to  $T_2^* = 28$  ns. The design fidelities averaged over this distribution are 99%, 98% and 96% for the e-H swap, e-C swap, and 3-qubit compression, respectively. The bottom part of Fig. 7.6 illustrates the implementation of controls necessary for the first round of 3-qubit HBAC using AHC.

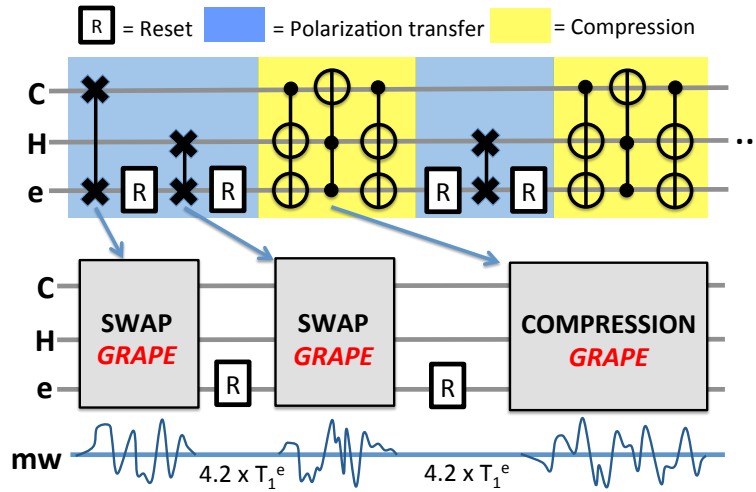


Figure 7.6: Quantum circuit of 3-qubit HBAC using the AHC method. The electron spin is the reset qubit, and it is refreshed by waiting for  $4.2 \times T_1^e$ . In the optimal crystal orientation for AHC, the forbidden transition strength of  $C_m$  is weaker than that of the proton. Consequently, the  $C_m$  polarization decays more slowly during electron reset and  $C_m$  is chosen as the target qubit. Two rounds of the algorithm are shown in the top panel. The 3-qubit PPA iteratively applies polarization transfer (shaded in blue) and the compression (shaded in yellow). All gates are designed in the microwave domain using the GRAPE algorithm. The GRAPE pulse lengths are 840 ns for the swap gates and 900 ns for the compression gate. A schematic of the AHC sequence for this circuit is shown in the lower part.



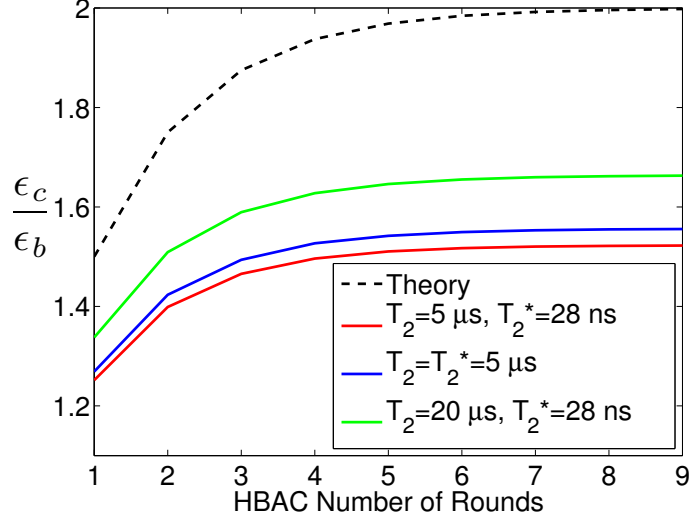


Figure 7.7: Simulation results for 3-qubit HBAC using AHC. The plot shows the ratio of the  $C_m$  polarization ( $\epsilon_c$ ) and the electron bath polarization ( $\epsilon_b$ ) at the end of each HBAC round, up to 9 rounds. The black dashed curve is the theoretical (ideal) value. The red curve is obtained by incorporating all experimentally determined (room temperature) relaxation parameters. The blue curve is obtained by allowing the  $T_2^*$  of the electron to equal  $T_2$ . The green curve is obtained by allowing  $T_2^e$  to be 20  $\mu\text{s}$ , 4 times longer than the measured value, in order to test the consequence of a longer  $T_2$ .

Fig. 7.7 shows the polarization of  $C_m$  at the end of each round of 3-qubit HBAC. The red curve is obtained when the simulation incorporates the experimentally determined, room temperature electron relaxation effects. The  $C_m$  polarization exceeds the bath polarization after the first round of HBAC, and increases further asymptotically as the HBAC is repeated. Nevertheless, the polarization enhancement is below the theoretically calculated value; after 9 HBAC rounds, the polarization of  $C_m$  is about 76% of the theoretical value. The largest contribution to the error is the loss of nuclear polarization due to the electron  $T_1$  process during the application of GRAPE pulses and the electron refresh steps. In the absence of decoherence, the GRAPE pulses transfer 99.6% and 99.8% of the electron polarization to  $C_m$  and H, respectively. The compression gate polarizes the carbon to  $1.49\epsilon_b$  at the end of the first round. However, when the  $T_1$  of the electron is introduced while  $T_2$  and  $T_2^*$  are still assumed to be infinite, the carbon and hydrogen polarizations prior to the compression step are reduced to 94.4% and 94.3% of the electron polarization, and the compression yields the carbon polarization of  $1.39\epsilon_b$ . Another source of the error is the

finite ratio of the electron  $T_2$  to the pulse duration;  $T_2^e$  is only about 5 to 6 times longer than the GRAPE pulses. One can imagine another type of 3-qubit molecule whose electron  $T_2$  is longer, for instance, 20  $\mu\text{s}$ . Then the polarization of the carbon after 7 rounds of HBAC is  $1.66\epsilon_b$ , which is 83% of the theoretical value (i.e. the green curve in Fig. 7.7). Finally, we consider a scenario in which the ESR linewidth is much narrower and  $T_2$  limited, i.e.  $T_2^* = T_2 = 5 \mu\text{s}$ . This result is indicated in blue in Fig. 7.7. Although there is a slight improvement by having a longer  $T_2^*$ , the experimental value of  $T_2^*$  does not pose a significant problem since the GRAPE pulses are designed to be robust to inhomogeneous line broadening.

## ENDOR control

In a pulsed ENDOR control scheme, the crystal orientation is chosen as shown in Tab. 7.4. In this orientation, the forbidden transition rates are both minimized, and it turns out the rate for H is weaker than that of  $C_m$ . Thus, H is chosen as the target qubit for cooling. The electron reset is done by waiting for  $5 \times T_1^e$  in order to bring the electron polarization to 99.3% of the thermal polarization. The loss of nuclear polarization during reset and control operations is negligible since the forbidden transition rates are both very weak. As shown in the bottom part of Fig. 7.8, the swap and compression gates can be decomposed into controlled-not (CNOT) gates and a toffoli gate. These operations can be realized by selective microwave and RF  $\pi$ -pulses. For example, the CNOT gate that flips the H spin if the electron is ‘spin down’ can be realized by RF pulses at frequencies that correspond to  $|\uparrow_H \uparrow_C \downarrow_e\rangle \leftrightarrow |\downarrow_H \uparrow_C \downarrow_e\rangle$  and  $|\uparrow_H \downarrow_C \downarrow_e\rangle \leftrightarrow |\downarrow_H \downarrow_C \downarrow_e\rangle$  transitions. In the compression step, a Toffoli gate that flips H spin if both  $C_m$  and electron are ‘spin down’ is required. However, the Toffoli gate on the proton cannot be realized by this method because the  $|\uparrow_H \uparrow_C \downarrow_e\rangle \leftrightarrow |\downarrow_H \uparrow_C \downarrow_e\rangle$  transition frequency is identical to the  $|\uparrow_H \downarrow_C \downarrow_e\rangle \leftrightarrow |\downarrow_H \downarrow_C \downarrow_e\rangle$  frequency. On the other hand, a Toffoli gate that flips the electron spin when both H and  $C_m$  are ‘spin down’ can be realized by applying a microwave pulse at the frequency of the  $|\downarrow_H \downarrow_C \uparrow_e\rangle \leftrightarrow |\downarrow_H \downarrow_C \downarrow_e\rangle$  transition, which is distinct from all other allowed ESR transition frequencies. Therefore, we modify the quantum circuit to extract the entropy from the electron during the compression, and use an additional swap gate to transfer the final polarization to the proton (see Fig. 7.8).

This quantum circuit enables one to repeatedly apply HBAC for pumping the H polarization. The compression step consists of four CNOT gates and a Toffoli gate, as shown in Fig. 7.8. Since the goal of the compression is only to extract entropy from the electron, the last two CNOT gates targetting the nuclear spins (shown in the red dashed box in Fig. 7.8) are not necessary. Hence, the compression is reduced to two CNOT gates and a Toffoli gate

as shown in the middle part of Fig. 7.8. The rectangular-shaped microwave and RF pulses shown at the bottom of Fig. 7.8 represent selective  $\pi$ -pulses, and the different shading of these pulses illustrate different frequencies.

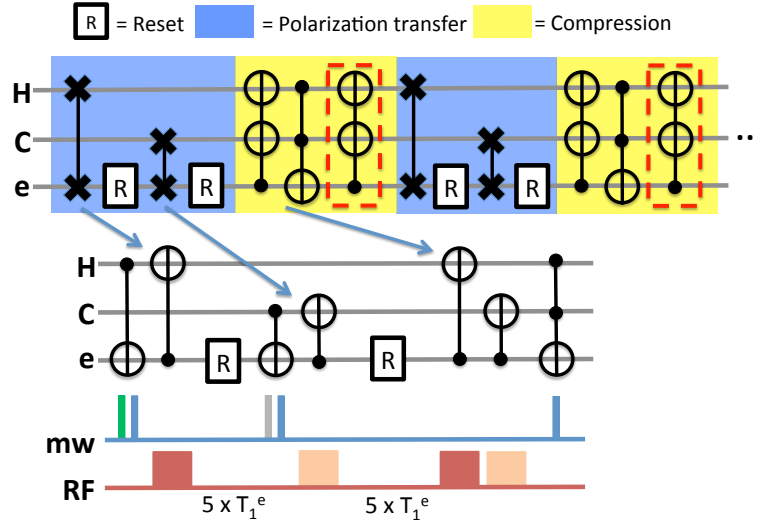


Figure 7.8: Quantum circuit of the 3-qubit HBAC using ENDOR control. The electron is used as the reset qubit, and it is refreshed by waiting for  $5 \times T_1$ . In the crystal orientation optimized for ENDOR, the forbidden transition rates of H are weaker than those of  $C_m$ , so H is chosen as the target qubit. The 3-qubit PPA iteratively applies polarization transfer (shaded in blue) and compression (shaded in yellow). All gates are realized using selective microwave and RF  $\pi$ -pulses. The compression step can only be implemented here to boost the electron polarization (see text for explanation), so a swap gate between the electron and proton is used to store the boosted polarization on the proton. The CNOT gates in the red dashed box are not necessary and are left out of the simulated implementation. The quantum circuit in the middle shows the gate decomposition of the swap and the compression into CNOT and Toffoli gates. The schematic of the microwave and RF pulse sequence at the bottom shows that the CNOT and Toffoli gates can be realized by transition-selective pulses. Shading illustrates different pulse frequencies.

The maximum power for microwave pulses is chosen such that the Rabi frequency is 25 MHz. In practice, the resonant microwave cavity has a finite bandwidth. This means that more input power is needed in order to drive transitions whose frequency is offset with respect to the cavity resonance frequency. Since the input power is limited in any real experimental setup, the pulse length must increase in order to apply the  $\pi$ -pulse at the offset frequency. Fig. 7.9 shows a simulated ESR spectrum centered at the resonator resonance

frequency of 10 GHz (red), and the voltage transfer function for a resonator with quality factor ( $Q$ ) of 100 (blue). If the pulse is applied at a frequency at which the corresponding value of the transfer function is  $x$ , then the pulse length must increase by a factor of  $1/x$  to compensate for the loss in transmitted power. This finite bandwidth effect must be taken into account in simulations because the algorithm cannot be successful if microwave pulse durations become comparable to the electron  $T_2$ . In the present simulations, the resonator quality factor  $Q$  is set to 100 and microwave pulse lengths are adjusted accordingly. The RF  $\pi$ -pulses are realized using  $15 \mu\text{s}$  (H) and  $60 \mu\text{s}$  ( $C_m$ ) square pulses, reflecting typical RF amplifier output power levels and assuming an untuned (broadband) RF circuit.

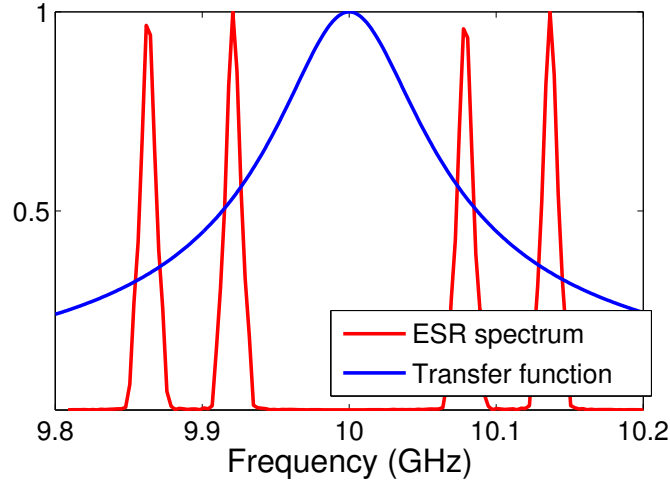


Figure 7.9: Simulated field-sweep spectra for the  $^{13}\text{C}_m$ -labeled malonic acid in the orientation given in Tab. 7.4 (red), and voltage transfer function for a microwave cavity with  $Q = 100$  (blue). The  $y$ -axis represents the scaling factor of square root of the microwave power in the cavity a function of the microwave frequency. Given a fixed maximum available microwave power, pulse durations for offset pulses must be increased relative to cavity-resonant pulses.

Using the room temperature electron  $T_1$ , the HBAC algorithm will not be successful because RF pulse lengths are similar to  $T_1^e$ . This can be solved by exploiting longer  $T_1^e$  values at lower temperatures. In unlabelled, irradiated malonic acid, we have found experimentally a  $T_1^e$  that grows roughly exponentially with temperature, e.g. with values of  $29 \mu\text{s}$ ,  $2.6 \text{ ms}$  and  $11 \text{ ms}$  at room temperature,  $43 \text{ K}$ , and  $22 \text{ K}$ , respectively. For simulating 3-qubit HBAC with ENDOR, we choose  $T_1^e = 2.6 \text{ ms}$  (ignoring the fact that a structural phase transition occurs at  $47 \text{ K}$ , probably complicating the ESR spectrum).

The selective microwave pulses must be designed with a care. While each pulse selectively excites certain transitions, they must also be broad enough to cover the ESR linewidth of about 12 MHz. First, we simulate 50 ns gaussian-shaped pulses with the full width at half maximum of 20 ns in order to excite the entire ESR linewidth and remain selective on the particular transition. The result is shown in Fig. 7.10 in red. The main source of the error is the inability of the Gaussian pulses to uniformly rotate all spins across the ESR linewidth; the pulse bandwidth must be close to 50 MHz in order to fully excite the entire ESR line width, but the minimum distance between two ESR allowed transition frequencies is about 56 MHz. Thus, even in the absence of  $T_1$  and  $T_2$  effects, each swap gate loses 8% polarization. For the improved microwave control, selective  $\pi$ -pulses are engineered using the GRAPE algorithm and can be made robust to  $T_2^* = 28$  ns which corresponds to the ESR line width of 12 MHz. Using this method, swap gates can transfer 98% of the polarization from the electron to the target nuclear spin. The simulation results for HBAC using GRAPE microwave pulses and rectangular RF pulses are shown in blue in Fig. 7.10.

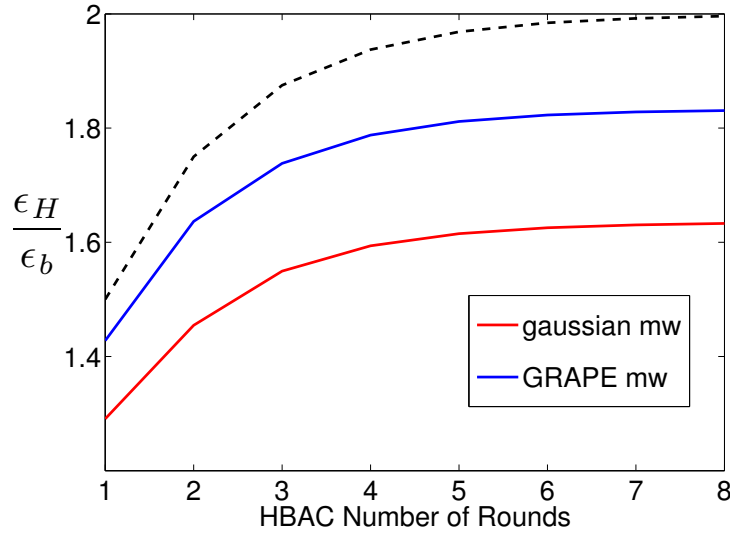


Figure 7.10: Simulation results of the 3-qubit HBAC using ENDOR control. The plot shows the ratio of H polarization to the electron thermal polarization after each round of the HBAC, up to 8 rounds. The black dashed curve is the theoretical value. The selective microwave  $\pi$ -pulses are designed in two different ways: (i) 50 ns gaussian-shaped MW pulses with 20 ns full width at half maximum (red), (ii) and GRAPE pulses (blue). In both cases, RF transitions are applied using square transition-selective pulses with 15 ns and 60 ns pulse lengths for H and  $C_m$  spins, respectively.

## 7.2.5 Simulating 5-qubit HBAC

As discussed in Sec. 7.2.3, due to weak forbidden transition rates of  $C_{1,2}$  and frequency overlap among ESR transitions, the AHC scheme cannot be implemented in the 5-qubit sample. Therefore, we focus on ENDOR control techniques in the simulation of 5-qubit HBAC. Here, we simulate one round of the 5-qubit HBAC as shown in Fig. 7.11, to demonstrate that cooling beyond the Shannon bound is experimentally feasible in the 5-qubit molecule. The quantum circuit we employ for 5-qubit HBAC is shown in Fig. 7.11. The electron is the target qubit, but the circuit can be easily modified to cool a nuclear spin by adding a swap gate after the compression step. Theoretically, by applying one round of the quantum circuit, the target qubit is cooled to  $\epsilon_b(15 - 10\epsilon_b^2 + 3\epsilon_b^4)/8 \approx 1.875\epsilon_b$  for small  $\epsilon_b$ . The orientation of the magnetic field used in the simulation is shown in Tab. 7.4, and the electron polarization and relaxation parameters are the same as used in the 3-qubit ENDOR HBAC simulation. The forbidden transition rates of the carbons are weaker than those of the proton, so the polarization transfer to H is done just before the compression gate, as shown in Fig. 7.11. Similar to the 3-qubit HBAC ENDOR circuit, the last CNOT gates in the compression step (inside the red dashed box) are not necessary since the electron is the target spin.

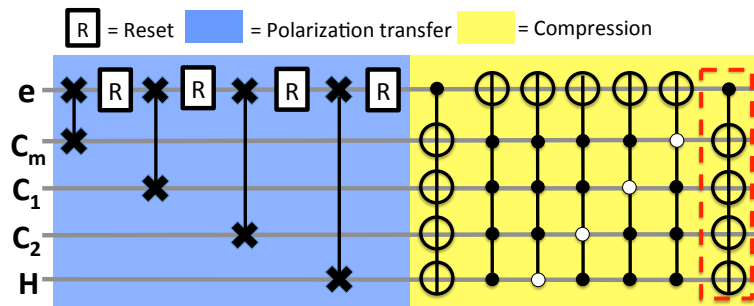


Figure 7.11: Quantum circuit for 5-qubit HBAC with the electron as the target spin. The polarization can be transferred to a nuclear spin with an additional swap gate. The last CNOT gates inside the red dashed box of the compression step are unnecessary, and are left out of the simulation. The open circles in the controlled gates indicate that the target spin is flipped if the control qubit is in the ‘spin up’ state. One round of the algorithm shown.

The usual method for a swap gate between the electron and one of the carboxyl carbons requires selective microwave control of  $C_1$  and  $C_2$ . However, the hyperfine tensors of  $C_1$  and  $C_2$  are very similar and it is impractical to separately address two spins by microwave

pulses due to spectral overlap. However, they can be separately addressed with RF pulses (see Sec. 7.2.3). Therefore, the polarization transfer step for  $C_{1,2}$  is modified as shown in Fig. 7.12, and theoretically polarizes both  $C_1$  and  $C_2$  to the electron thermal polarization.

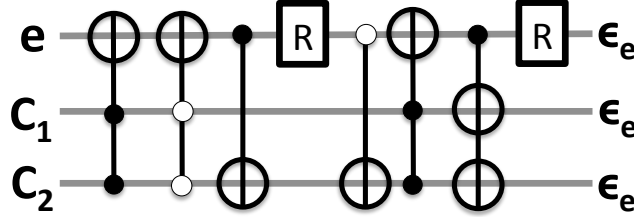


Figure 7.12: Circuit for polarization transfer between the electron and  $C_{1,2}$ . The circuit brings  $C_1$  and  $C_2$  to the bath temperature without selective microwave control, but requires selective RF pulses. The open circles in the controlled gates indicate that the target spin is flipped if the control qubit is in the ‘spin up’ state.

Note that the circuit shown in Fig. 7.11 is not the optimal cooling algorithm, i.e. the PPA. Fig. 7.13 compares the PPA and our cooling algorithm by showing the target qubit polarization  $\epsilon_t$  compared to the bath polarization as a function of HBAC steps. Here, each step consists of one refresh operation and one gate on the system qubits (in contrast to the ‘round’ used previously). In the low bath polarization regime, the PPA asymptotically increases the target qubit polarization to 8 times the bath polarization, while repeated application of the algorithm shown in Fig. 7.11 yields an asymptotic enhancement of 4. While it is possible to find sequences corresponding to the PPA, it is an open question whether such sequences could be practically implemented in this system. For the PPA, the gate decomposition of each system qubit operation depends on the input state, and can result in a complicated pulse sequence. An advantage of the algorithm implemented in our simulation is that the gate decomposition of each step is relatively simple and the asymptotic limit can be reached by simply repeating the quantum circuit.

As seen already in the 3-qubit HBAC simulation, designing microwave pulses that uniformly rotate all spin across the ESR line width while remaining transition-selective is a challenge. For the 5-qubit system, this problem is exacerbated since the ESR transitions are more closely spaced in frequency. In order to obtain the maximum polarization enhancement, GRAPE optimal control must again be used for designing the selective microwave pulses. GRAPE pulses that are robust to the experimentally determined value of  $T_2^*$  have been designed with at least 0.95 state fidelity and with 200 ns pulse lengths for the microwave pulses applied to  $C_m$  and  $C_2$ , 900 ns for  $C_1$  and  $^1\text{H}$ , and 100 ns for the 5-qubit

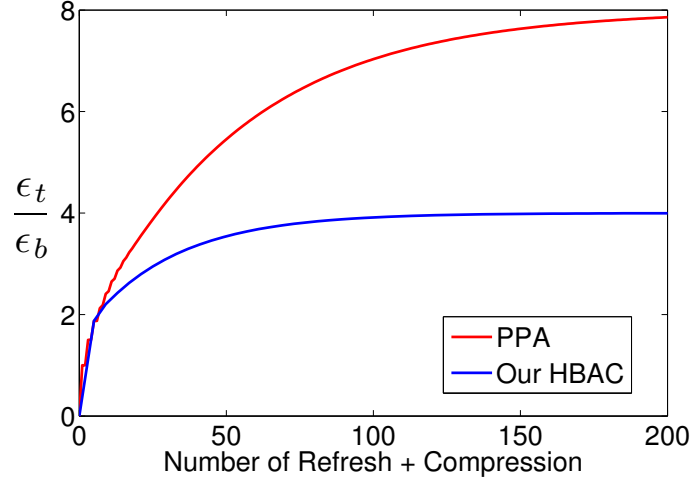


Figure 7.13: Theoretical target qubit polarization  $\epsilon_t$  normalized by the bath polarization, as a function of the number of cooling steps, to show the difference between the 5-qubit PPA and the algorithm in Fig. 7.11. Each step consists of one refresh operation and one gate on the system qubits. The red curve is obtained by the PPA while the blue curve is obtained by repeated application of the quantum circuit shown in Fig. 7.11. In the low polarization regime, the PPA allows the target qubit polarization to asymptotically approach 8 times the bath polarization, and 4 times the bath polarization with our algorithm.

compression. RF pulse lengths are chosen as  $5 \mu\text{s}$  and  $20 \mu\text{s}$  for  $^1\text{H}$  and  $^{13}\text{C}$ , respectively. Including the effects of the electron  $T_1$ ,  $T_2$ , and  $T_2^*$ , the polarization enhancement after one round of 5-qubit HBAC is  $1.67\epsilon_b$ . A major contribution to the error is the broad ESR line width compared to the spacing between ESR resonances, which makes realizing high fidelity transition-selective rotations on a time scale short compared to  $T_2^c$  difficult. Despite this, the simulation shows that a single round of 5-qubit HBAC with a realistic control sequence and relaxation yields a polarization enhancement beyond the Shannon bound, and also beyond the capability of a single round of 3-qubit HBAC. Another simulation is performed assuming a much narrower ESR line width, i.e.  $T_2^* = T_2$ . In this case, all microwave pulses can be designed with 99% unitary fidelity at 100 ns pulse length, and all nuclei reach at least 97% of the electron polarization during the polarization transfer steps. The polarization improvement after one round of 5-qubit HBAC is  $1.79\epsilon_b$ . This is 95% of the polarization improvement predicted by the theory, similar to the result of the 3-qubit HBAC simulation using ENDOR control with GRAPE microwave pulses. We expect the single qubit polarization to reach above  $3.6\epsilon_b$ , 90% of the theoretical value, as



the algorithm is repeated, similar to the 3-qubit case. The result shows that for HBAC with many qubits it is crucial to have a sharp ESR linewidth, which motivates a search for electron-nuclear spin systems having narrower ESR lines than the malonyl radical.

The 5-qubit HBAC results are summarized in Tab. 7.5.

|                         |       | <b>Simulation</b> |                         |                         |
|-------------------------|-------|-------------------|-------------------------|-------------------------|
|                         |       | <b>Theory</b>     |                         |                         |
|                         |       |                   | $T_2^* = 5 \mu\text{s}$ | $T_2^* = 28 \text{ ns}$ |
| $\epsilon_t/\epsilon_b$ | 1.875 | 1.79              | 1.67                    |                         |

Table 7.5: Polarization of the target qubit compared to the bath qubit after one round of 5-qubit HBAC. The quantum circuit for one round of 5-qubit HBAC is shown in Fig. 7.11. Results are shown for two different values of  $T_2^*$ . The electron spin lattice relaxation time is  $T_1^e = 2.6 \text{ ms}$  in this simulation.

Finally, we note two experimental caveats that are not taken into account in our simulations, but do not invalidate the main results. In the simulation sections, we accounted for a type of cross-relaxation in which the nuclear polarization decays due to a combination of the electronic spin-lattice relaxation process and the anisotropic term in the spin Hamiltonian of the form  $\hat{S}_z \hat{I}_x$ . There is an additional cross-relaxation mechanism involving noise acting directly on the nuclear operators, which we have not included in the Lindblad master equation. In future work, we plan to experimentally measure the cross-relaxation rates as a function of orientation and temperature to determine these additional contributions. If the additional mechanism is dominant, going to lower temperatures may be required in order to achieve sufficiently long nuclear  $T_1$  timescales. Secondly, a well known structural phase transition takes place in malonic acid at 46 K [147–149], which we have not considered here. Below 46 K, the  $P\bar{1}$  crystal symmetry is broken and there are two magnetically distinguishable molecules per unit cell. We have observed certain ENDOR transitions to split into two below 46 K, consistent with this phase change. However, experiments may be designed using phase-cycling techniques in order to cancel signal contributions from one of the molecules in the unit cell, so this does not in principle prevent the proposed AC experiments from being carried out.

### 7.3 Summary and future work

This chapter presented our work that accurately determined the full spin Hamiltonian of a five qubit electron-nuclear hyperfine coupled system in single crystal, irradiated malonic

acid. Using the hyperfine tensors, we determined the optimal magnetic field orientation for achieving high fidelity control using two control methods: anisotropic hyperfine control (AHC) and pulsed ENDOR techniques. Computer simulations were carried out using realistic experimental conditions and including the relevant electron spin relaxation parameters, demonstrating that the realization of 3-qubit and 5-qubit HBAC is feasible in this system. Using the 3-qubit molecule with AHC, the polarization of a nuclear spin is predicted to increase above  $1.5\epsilon_b$  after 9 rounds of the cooling algorithm. The ENDOR simulation assumed a lower temperature in which the electron  $T_1 = 2.6$  ms, in order to have the  $T_1$  sufficiently long compared to RF pulse lengths. Using GRAPE for selective microwave pulse design, the polarization of a nuclear spin is predicted to increase above  $1.8\epsilon_b$  after 9 rounds of the cooling algorithm. There is a tradeoff here between experimental simplicity and the achievable fidelity; the AHC experimental setup is simpler and can be performed at room temperature, but in general yields lower fidelities than the ENDOR approach at low temperature.

The carboxyl carbons in the 5-qubit sample have very weak forbidden transition rates under an applied microwave field, which prevents them from being practically controllable using AHC. Hence, for the 5-qubit HBAC simulation, we focused on the ENDOR control scheme. The 5-qubit simulation was again carried out at low temperature for a longer  $T_1$ , and the selective microwave pulses were designed using the GRAPE method. After one round of 5-qubit HBAC, the simulation predicts that the target qubit (the electron) would reach a polarization of  $1.67\epsilon_b$ . The major obstacle to reaching the ideal value of  $1.875\epsilon_b$  is the small spacing between certain allowed ESR transitions, similar in order to the ESR line width. Another simulation was performed assuming  $T_2^* = T_2$  to predict the outcome of the algorithm given a molecule that is similar to the malonic radical but with much sharper ESR transitions. Here, a target qubit polarization of  $1.79\epsilon_b$  is obtained after one round of the algorithm.

We conclude that the experimental demonstration of 3- and 5-qubit algorithmic cooling beyond the Shannon bound is feasible in the isotopically labelled malonyl radical. The 5-qubit system can yield a larger polarization enhancement compared to the 3-qubit system, as expected. The experimental value of  $T_2^*$  is found to be a critical factor that limits the fidelity of gate operations, and therefore the achievable polarization under HBAC. Nearly ideal results are obtainable when  $T_2^* = T_2$ .

The simulation results show that about 92% and 76% of the theoretically achievable polarization can be experimentally achieved after 8 rounds of 3-qubit HBAC using ENDOR and AHC methods, respectively. For 5-qubit HBAC simulation, about 89% of the ideal polarization value is obtained after 1 round. Assuming similar level of accuracy can be achieved after 10 rounds of HBAC, we can estimate realistic target qubit polarization after

applying 10 rounds of these HBAC as the temperature varies. This estimation gives us an idea at what temperature, the X-band spectrometer needs to be operating in order to be able to implement QEC using mixed ancilla qubits. In Sec. 2, we showed the result from [23] that if two ancilla qubits in the 3-qubit QEC code have same polarization  $\epsilon$ , then  $\epsilon > \sqrt{2} - 1 \approx 0.41$  is to be satisfied in order to improve the fidelity of a quantum state exposed to the dephasing channel. Fig. 7.14 shows the estimated values of the target spin qubit polarization as a function of temperature. One can see that near 1 to 2 K, an ancilla spin qubit can be polarized to the required value for QEC. Note that the improvement from the AHC methods should be better at lower temperatures since cross-relaxation rate is reduced as  $T_1$  of the electron increases at low temperatures. We expect that as the temperature is reduced, the polarization improvement in the AHC scheme will be slightly higher since the cross-relaxation effect during the GRAPE pulses are negligible. Nevertheless, the cross-relaxation effect on the nuclear polarization during the electronic reset is expected to be similar to the room-temperature case since longer  $T_1$  demands longer reset time.

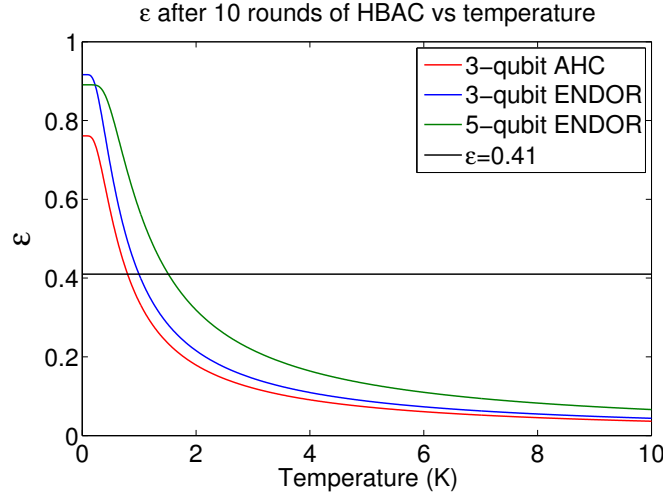


Figure 7.14: Estimation on the attainable target qubit polarization after 10 rounds of HBAC at various temperatures. The estimated values are obtained by assuming 92% and 76% of the theoretically achievable polarizations in the 3-qubit HBAC can be experimentally achievable, and 89% for the 5-qubit HBAC. At around 1-2 K temperature, one ancilla qubit can be polarized to above 0.41 that is required for the 3-qubit QEC code for dephasing to improve the fidelity of a quantum state exposed to the noisy channel.

The next step is to experimentally realize HBAC and demonstrate the polarization improvement predicted in the simulations. The first experiment is to apply the 3-qubit

algorithmic cooling to  $^{13}\text{C}_m$ -labelled malonic acid using both AHC and ENDOR control methods. We are currently testing our control to realize electron-nuclear two qubit gates with high fidelity using AHC scheme as a necessary step towards experimental realization of HBAC. The ENDOR experiment is currently undertaken by collaborators at the Osaka City University in Japan. I contributed to the ENDOR experiment by finding the optimal orientation for the given crystal shape, and by developing a simulation tool and obtaining preliminary simulation results.

# Chapter 8

## Conclusions and outlook

NMR quantum information processors are one of the best test beds to experimentally implement and develop protocols for exploring quantum control techniques that are also applicable in other platforms. High control fidelity has been shown in NMR quantum computing in the few-qubit regime, and a scalable method for characterizing noise is well developed. Nevertheless, for building a large scale quantum computer, the ability to implement quantum error correction is critical and still remains challenging for NMR quantum processors as well as for many potential implementations. The major obstacle against experimental realization of multiple rounds of QEC in NMR QIP is the difficulty in supplying highly polarized ancilla spin qubits on demand.

Moving to the solid state electron spin resonance systems where an unpaired electron is hyperfine-coupled to nuclear spins is promising direction for the development of larger scale quantum information processors. First, the electron's higher gyromagnetic ratio compared to that of nuclei can be exploited to provide about three orders of magnitude enhanced spin qubit polarization. In addition, imbalance of the  $T_1$  relaxation time scale between electron and nuclear spins opens the possibility for implementing open system cooling such as heat bath algorithmic cooling for purifying spin qubits beyond electron thermal equilibrium polarization. Also, fast gate operations can be realized by making use of strong anisotropic hyperfine interaction between electron and nuclear spins. Furthermore, there is a recent proposal of building a multi-node quantum computer containing about 100 qubits employing electron and nuclear spins [155]. Engineering such a system permits testing the ideas of quantum control and error correction in a setting unavailable to classical simulations, opening a path to the development of future large scale quantum devices.

In the introduction, we stated the main questions to be addressed in this thesis as

follows. The first goal was to achieve and demonstrate high accuracy in controlling the electron spin for QIP. The second was to study whether experimental implementation of heat bath algorithmic cooling is feasible with realistic electron-nuclear spin systems for cooling a nuclear spin beyond electron thermal equilibrium polarization. As an interlude on the way to answering these questions, we first demonstrated a liquid state NMR experiment utilizing three nuclear spin qubits that was designed to directly test the validity of Born's rule, one the fundamental postulates of quantum mechanics. Utilizing the high control fidelity available in the system, we experimentally bounded the deviation of the Born rule to  $\sim 10^{-3} \pm 10^{-3}$ . The experiment also serves to demonstrate that the control level in the liquid state NMR in the few-qubit regime is precise enough for experimentally testing foundational laws of quantum theory. Also, we reported our progress towards providing more detailed analysis on the  $T_{1\rho}$  noise spectroscopy protocol. The noise spectroscopy protocol can be a useful tool to design a dynamical decoupling sequence to decrease the system-environment interaction which in turn can be beneficial for QEC by reducing the error probability. Next, we moved onto the electron-nuclear system and first described the home-built spectrometer and the low temperature probe which enable quantum computations using electron and nuclear spin registers. The single qubit randomized benchmarking protocol was applied not only for measuring the average single qubit gate fidelity, but also for optimizing the spectrometer configuration and improving the quantum control. The error per single qubit Clifford gate on the electron in fused irradiated quartz was  $0.81 \pm 0.04\%$ . From this, the first goal is achieved; we built experimental tools for controlling the electron spin with greater than 99% accuracy. We answered the second question in Sec. 7 by extracting the full spin Hamiltonian of irradiated malonic acid  $\dot{\text{C}}\text{H}(\text{COOH})_2$  in single crystal, finding the crystal orientation for optimal control, and carrying out realistic simulations. Our work showed that both 3-qubit and 5-qubit HBAC can be realized in the electron-nuclear spin system and cool a nuclear spin beyond the electron thermal equilibrium polarization.

The short term future goal is to experimentally implement 3-qubit HBAC. At present, our collaborators in Japan are working on implementing 3-qubit HBAC using a pulsed ENDOR set-up. Meanwhile, our home-built spectrometer is capable of implementing the AHC scheme. The AHC simulation employed GRAPE pulses for implementing swap and compression gates with 96% to 99% gate fidelity at room temperature, and still acquired a nuclear polarization greater than 1.5 times the electron thermal polarization. Also, in the AHC scheme the dominating source of error was the cross-relaxation effect which induces nuclear relaxation via anisotropic hyperfine interaction and the electron  $T_1$  process. We expect that if the gates required in the 3-qubit HBAC can be implemented with a similar level of control that was demonstrated in the single qubit randomized benchmarking, experimental cooling of a nuclear spin beyond  $1.5\epsilon_b$  can be achieved. The polarization boost

can be slightly higher if the experiment is performed in cryogenic temperatures where the cross-relaxation effect on the nuclear polarization during GRAPE pulses is negligibly small due to longer electronic  $T_1$ . Currently, we are working towards demonstrating high fidelity two-qubit gates using the AHC method in our pulsed ESR spectrometer.

In the long run, it will be interesting to add the pulsed ENDOR capability to our home-built spectrometer and to explore benefits of having direct nuclear control in addition to the AHC scheme. It is even possible to add optical fibre in the current spectrometer that allows one to study photo-excited triplet states that can provide highly polarized spins at room-temperature by optical pumping and dynamic nuclear polarization [156, 157] for QIP applications.

# References

- [1] R. P. Feynman, “Simulating physics with computers,” *International Journal of Theoretical Physics*, vol. 21, p. 467, 1982.
- [2] P. Shor, “Algorithms for quantum computation: discrete logarithms and factoring,” in *Foundations of Computer Science, 1994 Proceedings., 35th Annual Symposium on*, pp. 124–134, Nov 1994.
- [3] L. K. Grover, “A fast quantum mechanical algorithm for database search,” in *Proceedings of the Twenty-eighth Annual ACM Symposium on Theory of Computing, STOC '96*, (New York, NY, USA), pp. 212–219, ACM, 1996.
- [4] E. Knill and R. Laflamme, “Theory of quantum error-correcting codes,” *Physical Review A*, vol. 55, no. 2, p. 900, 1997.
- [5] E. Knill, R. Laflamme, and W. H. Zurek, “Resilient quantum computation,” *Science*, vol. 279, no. 5349, pp. 342–345, 1998.
- [6] J. Preskill, “Reliable quantum computers,” *Proceedings of the Royal Society of London. Series A: Mathematical, Physical and Engineering Sciences*, vol. 454, no. 1969, pp. 385–410, 1998.
- [7] E. Knill, “Quantum computing with realistically noisy devices,” *Nature*, vol. 434, no. 7029, pp. 39–44, 2005.
- [8] P. Aliferis, D. Gottesman, and J. Preskill, “Accuracy threshold for postselected quantum computation,” *arXiv preprint quant-ph/0703264*, 2007.
- [9] D. Gottesman, *Stabilizer codes and quantum error correction*. PhD thesis, Caltech, 1997.



- [10] O. Moussa, J. Baugh, C. A. Ryan, and R. Laflamme, “Demonstration of sufficient control for two rounds of quantum error correction in a solid state ensemble quantum information processor,” *Physical review letters*, vol. 107, no. 16, p. 160501, 2011.
- [11] T. H. Taminiau, J. Cramer, T. van der Sar, V. V. Dobrovitski, and R. Hanson, “Universal control and error correction in multi-qubit spin registers in diamond,” *Nature Nanotechnology*, vol. 9, pp. 171–176, 03 2014.
- [12] J. Kelly, R. Barends, A. G. Fowler, A. Megrant, E. Jeffrey, T. C. White, D. Sank, J. Y. Mutus, B. Campbell, Y. Chen, Z. Chen, B. Chiaro, A. Dunsworth, I. C. Hoi, C. Neill, P. J. J. O’Malley, C. Quintana, P. Roushan, A. Vainsencher, J. Wenner, A. N. Cleland, and J. M. Martinis, “State preservation by repetitive error detection in a superconducting quantum circuit,” *Nature*, vol. 519, pp. 66–69, 03 2015.
- [13] E. Knill, R. Laflamme, R. Martinez, and C.-H. Tseng, “An algorithmic benchmark for quantum information processing,” *Nature*, vol. 404, no. 6776, pp. 368–370, 2000.
- [14] C. Negrevergne, T. S. Mahesh, C. A. Ryan, M. Ditty, F. Cyr-Racine, W. Power, N. Boulant, T. Havel, D. G. Cory, and R. Laflamme, “Benchmarking quantum control methods on a 12-qubit system,” *Physical Review Letters*, vol. 96, no. 17, p. 170501, 2006.
- [15] C. A. Ryan, M. Laforest, and R. Laflamme, “Randomized benchmarking of single- and multi-qubit control in liquid-state nmr quantum information processing,” *New Journal of Physics*, vol. 11, no. 1, p. 013034, 2009.
- [16] B. Criger, G. Passante, D. Park, and R. Laflamme, “Recent advances in nuclear magnetic resonance quantum information processing,” *Philosophical Transactions of the Royal Society A: Mathematical, Physical and Engineering Sciences*, vol. 370, no. 1976, pp. 4620–4635, 2012.
- [17] D. Lu, A. Brodutch, J. Park, H. Katiyar, T. Jochym-O’connor, and R. Laflamme, “NMR quantum information processing,” *arXiv:1501.01353 [quant-ph]*, 2015.
- [18] J. Emerson, M. Silva, O. Moussa, C. Ryan, M. Laforest, J. Baugh, D. G. Cory, and R. Laflamme, “Symmetrized characterization of noisy quantum processes,” *Science*, vol. 317, no. 5846, pp. 1893–1896, 2007.
- [19] E. Knill, D. Leibfried, R. Reichle, J. Britton, R. B. Blakestad, J. D. Jost, C. Langer, R. Ozeri, S. Seidelin, and D. J. Wineland, “Randomized benchmarking of quantum gates,” *Phys. Rev. A*, vol. 77, p. 012307, Jan 2008.

- [20] E. Magesan, J. M. Gambetta, and J. Emerson, “Characterizing quantum gates via randomized benchmarking,” *Phys. Rev. A*, vol. 85, p. 042311, Apr 2012.
- [21] D. Aharonov and M. Ben-Or, “Fault-tolerant quantum computation with constant error,” in *Proceedings of the Twenty-ninth Annual ACM Symposium on Theory of Computing*, (New York, NY, USA), pp. 176–188, ACM, 1997.
- [22] P. Kaye, R. Laflamme, and M. Mosca, *An Introduction to Quantum Computing*. Oxford University Press, 2007.
- [23] B. Criger, O. Moussa, and R. Laflamme, “Quantum error correction with mixed ancilla qubits,” *Physical Review A*, vol. 85, no. 4, p. 044302, 2012.
- [24] P. O. Boykin, T. Mor, V. Roychowdhury, F. Vatan, and R. Vrijen, “Algorithmic cooling and scalable nmr quantum computers,” *Proc. Natl. Acad. Sci. U.S.A.*, vol. 99, p. 3388, 2002.
- [25] J. M. Fernandez, S. Lloyd, T. Mor, and V. Roychowdhury, “Algorithmic cooling of spins: A practicable method for increasing polarization,” *International Journal of Quantum Information*, vol. 2, no. 4, pp. 461–477, 2004.
- [26] F. Rempp, M. Michel, and G. Mahler, “Cyclic cooling algorithm,” *Physical Review A*, vol. 76, p. 032325, 2007.
- [27] P. Kaye, “Cooling algorithm based on the 3-bit majority,” 2007. arXiv:quant-ph/0703194v3.
- [28] L. J. Schulman, T. Mor, and Y. Weinstein, “Physical limits of heat-bath algorithmic cooling,” *Physical Review Letters*, vol. 94, p. 120501, 2005.
- [29] J. Baugh, O. Moussa, C. A. Ryan, A. Nayak, and R. Laflamme, “Experimental implementation of heat-bath algorithmic cooling using solid-state nuclear magnetic resonance,” *Nature*, vol. 438, no. 7067, pp. 470–473, 2005.
- [30] C. A. Ryan, O. Moussa, J. Baugh, and R. Laflamme, “Spin based heat engine: Demonstration of multiple rounds of algorithmic cooling,” *Physical Review Letters*, vol. 100, p. 140501, 2008.
- [31] N. Khaneja, “Switched control of electron nuclear spin systems,” *Phys. Rev. A*, vol. 76, p. 032326, 2007.

- [32] J. S. Hodges, J. C. Yang, C. Ramanathan, and D. G. Cory, “Universal control of nuclear spins via anisotropic hyperfine interactions,” *Physical Review A*, vol. 78, no. 1, p. 010303, 2008.
- [33] Y. Zhang, C. A. Ryan, R. Laflamme, and J. Baugh, “Coherent control of two nuclear spins using the anisotropic hyperfine interaction,” *Phys. Rev. Lett.*, vol. 107, p. 170503, Oct 2011.
- [34] B. Criger, D. Park, and J. Baugh, *Few-Qubit Magnetic Resonance Quantum Information Processors: Simulating Chemistry and Physics*, vol. 154 of *Advances in Chemical Physics*, ch. Quantum Information and Computation for Chemistry, pp. 193–228. John Wiley & Sons, Inc., 2014.
- [35] D. K. Park, O. Moussa, and R. Laflamme, “Three path interference using nuclear magnetic resonance: a test of the consistency of born’s rule,” *New Journal of Physics*, vol. 14, no. 11, p. 113025, 2012.
- [36] D. K. Park, G. Feng, R. Rahimi, S. Labruyère, T. Shibata, S. Nakazawa, K. Sato, T. Takui, R. Laflamme, and J. Baugh, “Hyperfine spin qubits in irradiated malonic acid: heat-bath algorithmic cooling,” *Quantum Information Processing*, vol. 14, no. 7, pp. 2435–2461, 2015.
- [37] C. Ryan, *Characterization and Control in Large Hilbert Spaces*. PhD thesis, University of Waterloo, 2008.
- [38] M. Laforest, *Error characterization and quantum control benchmarking in liquid state NMR using quantum information processing techniques*. PhD thesis, University of Waterloo, 2008.
- [39] N. A. Gershenfeld and I. L. Chuang, “Bulk spin-resonance quantum computation,” *Science*, vol. 275, no. 5298, pp. 350–356, 1997.
- [40] D. G. Cory, A. F. Fahmy, and T. F. Havel, “Ensemble quantum computing by nmr spectroscopy,” *Proceedings of the National Academy of Sciences*, vol. 94, no. 5, pp. 1634–1639, 1997.
- [41] O. Moussa, “On heat-bath algorithmic cooling and its implementation in solid-state NMR,” Master’s thesis, University of Waterloo, 2005.

- [42] I. Almog, Y. Sagi, G. Gordon, G. Bensky, G. Kurizki, and N. Davidson, “Direct measurement of the system–environment coupling as a tool for understanding decoherence and dynamical decoupling,” *J. Phys. B: At. Mol. Opt. Phys.*, vol. 44, no. 15, p. 154006, 2011.
- [43] F. Yan, S. Gustavsson, J. Bylander, X. Jin, F. Yoshihara, D. G. Cory, Y. Nakamura, T. P. Orlando, and W. D. Oliver, “Rotating-frame relaxation as a noise spectrum analyser of a superconducting qubit undergoing driven evolution,” *Nat. Commun.*, vol. 4:2337, 2013.
- [44] T. Green, H. Uys, and M. J. Biercuk, “High-order noise filtering in nontrivial quantum logic gates,” *Phys. Rev. Lett.*, vol. 109, p. 020501, Jul 2012.
- [45] T. J. Green, J. Sastrawan, H. Uys, and M. J. Biercuk, “Arbitrary quantum control of qubits in the presence of universal noise,” *New J. Phys.*, vol. 15, p. 095004, 2013.
- [46] A. G. Kofman and G. Kurizki, “Unified theory of dynamically suppressed qubit decoherence in thermal baths,” *Phys. Rev. Lett.*, vol. 93, p. 130406, Sep 2004.
- [47] A. G. Kofman and G. Kurizki, “Universal dynamical control of quantum mechanical decay: Modulation of the coupling to the continuum,” *Phys. Rev. Lett.*, vol. 87, p. 270405, Dec 2001.
- [48] L. Cywiński, R. M. Lutchyn, C. P. Nave, and S. Das Sarma, “How to enhance dephasing time in superconducting qubits,” *Phys. Rev. B*, vol. 77, p. 174509, May 2008.
- [49] A. Ajoy, G. A. Álvarez, and D. Suter, “Optimal pulse spacing for dynamical decoupling in the presence of a purely dephasing spin bath,” *Phys. Rev. A*, vol. 83, p. 032303, Mar 2011.
- [50] M. J. Biercuk, A. C. Doherty, and H. Uys, “Dynamical decoupling sequence construction as a filter-design problem,” *J. Phys. B: At. Mol. Opt. Phys.*, vol. 44, no. 15, p. 154002, 2011.
- [51] G. A. Álvarez and D. Suter, “Measuring the spectrum of colored noise by dynamical decoupling,” *Phys. Rev. Lett.*, vol. 107, p. 230501, 2011.
- [52] H. Uys, M. J. Biercuk, and J. J. Bollinger, “Optimized noise filtration through dynamical decoupling,” *Phys. Rev. Lett.*, vol. 103, p. 040501, Jul 2009.

- [53] G. S. Uhrig, “Exact results on dynamical decoupling by  $\pi$  pulses in quantum information processes,” *New J. Phys.*, vol. 10, no. 8, p. 083024, 2008.
- [54] M. J. Biercuk, H. Uys, A. P. VanDevender, N. Shiga, W. M. Itano, and J. J. Bollinger, “Optimized dynamical decoupling in a model quantum memory,” *Nature*, vol. 458, pp. 996–1000, Apr 2009.
- [55] G. Gordon, G. Kurizki, and D. A. Lidar, “Optimal dynamical decoherence control of a qubit,” *Phys. Rev. Lett.*, vol. 101, p. 010403, Jul 2008.
- [56] T. Yuge, S. Sasaki, and Y. Hirayama, “Measurement of the noise spectrum using a multiple-pulse sequence,” *Phys. Rev. Lett.*, vol. 107, p. 170504, 2011.
- [57] J. Clausen, G. Bensky, and G. Kurizki, “Bath-optimized minimal-energy protection of quantum operations from decoherence,” *Phys. Rev. Lett.*, vol. 104, p. 040401, Jan 2010.
- [58] G. S. Uhrig, “Keeping a quantum bit alive by optimized  $\pi$ -pulse sequences,” *Phys. Rev. Lett.*, vol. 98, p. 100504, 2007.
- [59] Y. Pan, Z.-R. Xi, and W. Cui, “Optimal dynamical decoupling sequence for the ohmic spectrum,” *Phys. Rev. A*, vol. 81, p. 022309, Feb 2010.
- [60] N. Bar-Gill, L. Pham, C. Belthangady, D. L. Sage, P. Cappellaro, J. Maze, M. Lukin, A. Yacoby, and R. Walsworth, “Suppression of spin-bath dynamics for improved coherence of multi-spin-qubit systems,” *Nat. Commun.*, vol. 3:858, 2012.
- [61] E. Geva, R. Kosloff, and J. L. Skinner, “On the relaxation of a two-level system driven by a strong electromagnetic field,” *J. Chem. Phys.*, vol. 102, p. 8541, Jun 1995.
- [62] F. J. Dyson, “The radiation theories of Tomonaga, Schwinger, and Feynman,” *Phys. Rev.*, vol. 75, pp. 486–502, 1949.
- [63] W. Magnus, “On the exponential solution of differential equations for a linear operator,” *Comm. Pure Appl. Math.*, vol. 7, no. 4, pp. 649–73, 1954.
- [64] M. Born, “Zur quantenmechanik der stossvorgange,” *Zeitschrift fur Physik*, vol. 37, pp. 863–867, 1926.
- [65] U. Sinha, C. Couteau, T. Jennewein, R. Laflamme, and G. Weihs, “Ruling out multi-order interference in quantum mechanics,” *Science*, vol. 329, no. 5990, p. 418, 2010.

- [66] U. Sinha, C. Couteau, Z. Medendorp, I. Sollner, R. Laflamme, R. Sorkin, and G. Weihs, “Testing Born’s Rule in Quantum Mechanics with a Triple Slit Experiment,” in *Foundations of Probability and Physics-5, American Institute of Physics Conference Proceedings*, 2008.
- [67] R. Sorkin, “Quantum Mechanics as Quantum Measure Theory,” *Mod. Phys. Lett.*, vol. 9, no. 33, pp. 3119–3128, 1994.
- [68] R. Laflamme, E. Knill, D. G. Cory, E. M. Fortunato, T. Havel, C. Miquel, R. Martinez, C. Negrevergne, G. Ortiz, M. A. Pravia, Y. Sharf, S. Sinha, R. Somma, and L. Viola, “Introduction to nmr quantum information processing,” *Los Alamos Science*, vol. 27, p. 226, 2002.
- [69] D. Cory, “A DANTE-based method for radio frequency-field selection,” *Journal of Magnetic Resonance, Series A*, vol. 103, no. 1, pp. 23 – 26, 1993.
- [70] A. Shaka, J. Keeler, M. Smith, and R. Freeman, “Spatial localization of nmr signals in an inhomogeneous radiofrequency field,” *Journal of Magnetic Resonance (1969)*, vol. 61, no. 1, pp. 175 – 180, 1985.
- [71] E. Knill, R. Laflamme, R. Martinez, and C. H. Tseng, “An algorithmic benchmark for quantum information processing,” *Nature*, vol. 404, no. 6776, p. 368, 2000.
- [72] N. Khaneja, T. Reiss, C. Kehlet, T. Schulte-Herbrüggen, and S. J. Glaser, “Optimal control of coupled spin dynamics: design of nmr pulse sequences by gradient ascent algorithms,” *Journal of Magnetic Resonance*, vol. 172, no. 2, pp. 296–305, 2005.
- [73] Y. S. Weinstein, T. F. Havel, J. Emerson, N. Boulant, M. Saraceno, S. Lloyd, and D. G. Cory, “Quantum process tomography of the quantum fourier transform,” *J. Chem. Phys.*, vol. 121, no. 13, p. 6117, 2004.
- [74] C. A. Ryan, M. Laforest, and R. Laflamme, “Randomized benchmarking of single- and multi-qubit control in liquid-state nmr quantum information processing,” *New J. of Phys.*, vol. 11, no. 1, p. 013034, 2009.
- [75] V. Athalye, S. S. Roy, and T. S. Mahesh, “Investigation of the leggett-garg inequality for precessing nuclear spins,” *Phys. Rev. Lett.*, vol. 107, p. 130402, 2011.
- [76] J. R. Samal, A. K. Pati, and A. Kumar, “Experimental test of the quantum no-hiding theorem,” *Phys. Rev. Lett.*, vol. 106, p. 080401, 2011.

- [77] O. Moussa, R. C. A., D. G. Cory, and R. Laflamme, “Testing contextuality on quantum ensembles with one clean qubit,” *Phys. Rev. Lett.*, vol. 104, no. 16, p. 160501, 2010.
- [78] A. M. Souza, A. Magalhães, J. Teles, E. R. deAzevedo, T. J. Bonagamba, I. S. Oliveira, and R. S. Sarthour, “Nmr analog of bell’s inequalities violation test,” *New J. Phys.*, vol. 10, no. 3, p. 033020, 2008.
- [79] A. M. Souza, I. S. Oliveira, and R. S. Sarthour, “A scattering quantum circuit for measuring bell’s time inequality: a nuclear magnetic resonance demonstration using maximally mixed states,” *New J. Phys.*, vol. 13, no. 5, p. 053023, 2011.
- [80] G. Ithier, E. Collin, P. Joyez, P. J. Meeson, D. Vion, D. Esteve, F. Chiarello, A. Shnirman, Y. Makhlin, J. Schrieffer, and G. Schön, “Decoherence in a superconducting quantum bit circuit,” *Phys. Rev. B*, vol. 72, p. 134519, Oct 2005.
- [81] J. Bylander, S. Gustavsson, F. Yan, F. Yoshihara, K. Harrabi, G. Fitch, D. G. Cory, Y. Nakamura, J.-S. Tsai, and W. D. Oliver, “Noise spectroscopy through dynamical decoupling with a superconducting flux qubit,” *Nat Phys*, vol. 7, no. 7, pp. 565–70, 2011.
- [82] D. H. Slichter, R. Vijay, S. J. Weber, S. Boutin, M. Boissonneault, J. M. Gambetta, A. Blais, and I. Siddiqi, “Measurement-induced qubit state mixing in circuit qed from up-converted dephasing noise,” *Phys. Rev. Lett.*, vol. 109, p. 153601, Oct 2012.
- [83] C. P. Slichter and D. Ailion, “Low-field relaxation and the study of ultraslow atomic motions by magnetic resonance,” *Phys. Rev.*, vol. 135, p. A1099, Aug 1964.
- [84] D. C. Ailion and C. P. Slichter, “Observation of ultra-slow translational diffusion in metallic lithium by magnetic resonance,” *Phys. Rev.*, vol. 137, p. A235, Jan 1965.
- [85] D. C. Ailion, “NMR and ultraslow motions,” *Adv. Mag. Res.*, vol. 5, pp. 177–227, 1971.
- [86] D. C. Look and I. J. Lowe, “Nuclear magnetic dipole-dipole relaxation along the static and rotating magnetic fields: Application to gypsum,” *The Journal of Chemical Physics*, vol. 44, no. 8, p. 2995, 1966.
- [87] J. M. Martinis, S. Nam, J. Aumentado, K. M. Lang, and C. Urbina, “Decoherence of a superconducting qubit due to bias noise,” *Phys. Rev. B*, vol. 67, p. 094510, Mar 2003.

- [88] J. S. Waugh, *Average hamiltonian theory*. John Wiley & Sons, Ltd., 2007.
- [89] J. S. Waugh, L. M. Huber, and U. Haeberlen, “Approach to high-resolution nmr in solids,” *Phys. Rev. Lett.*, vol. 20, pp. 180–182, Jan 1968.
- [90] U. Haeberlen and J. S. Waugh, “Coherent averaging effects in magnetic resonance,” *Phys. Rev.*, vol. 175, pp. 453–467, 1968.
- [91] S. Blanes, F. Casas, J. Oteo, and J. Ros, “The magnus expansion and some of its applications,” *Phys. Rep.*, vol. 470, no. 5-6, p. 151, 2009.
- [92] U. Haeberlen, *High Resolution NMR in Solids: Selective Averaging*. Advances in Magnetic Resonance, New York: Academic Press, 1976.
- [93] J. Baugh, O. Moussa, C. A. Ryan, R. Laflamme, C. Ramanathan, T. F. Havel, and D. G. Cory, “Solid-state nmr three-qubit homonuclear system for quantum-information processing: Control and characterization,” *Phys. Rev. A*, vol. 73, p. 022305, 2006.
- [94] T. W. Borneman, C. E. Granade, and D. G. Cory, “Parallel information transfer in a multinode quantum information processor,” *Phys. Rev. Lett.*, vol. 108, p. 140502, Apr 2012.
- [95] A. Schweiger and G. Jeschke, *Principles of pulse electron paramagnetic resonance*. Oxford University Press, 2001.
- [96] N. Atherton, *Principles of electron spin resonance*. Ellis Horwood Limited, 1993.
- [97] Y. Zhang, C. A. Ryan, R. Laflamme, and J. Baugh, “Coherent control of two nuclear spins using the anisotropic hyperfine interaction,” *Physical review letters*, vol. 107, no. 17, p. 170503, 2011.
- [98] G. Turinicia and H. Rabitzb, “Quantum wavefunction controllability,” *Chemical Physics*, vol. 267, no. 1–3, pp. 1–9, 2001.
- [99] C. Altafini, “Controllability of quantum mechanical systems by root space decomposition of  $\mathfrak{su}(n)$ ,” *J. Math. Phys.*, vol. 43, no. 5, p. 2051, 2002.
- [100] M. H. Levitt, “Composite pulses,” *Progress in Nuclear Magnetic Resonance Spectroscopy*, vol. 18, pp. 61–122, 1986.



- [101] J. Baum, R. Tycko, and A. Pines, “Broadband and adiabatic inversion of a two-level system by phase-modulated pulses,” *Phys. Rev. A*, vol. 32, pp. 3435–3447, 1985.
- [102] E. Kupce and R. Freeman, “Adiabatic pulses for wideband inversion and broadband decoupling,” *Journal of Magnetic Resonance, Series A*, vol. 115, no. 2, pp. 273 – 276, 1995.
- [103] R. A. Degraaf, Y. Luo, M. Terpstra, H. Merkle, and M. Garwood, “A new localization method using an adiabatic pulse, bir-4,” *Journal of Magnetic Resonance, Series B*, vol. 106, no. 3, pp. 245 – 252, 1995.
- [104] M. Garwood and L. DelaBarre, “The return of the frequency sweep: Designing adiabatic pulses for contemporary nmr,” *Journal of Magnetic Resonance*, vol. 153, no. 2, pp. 155 – 177, 2001.
- [105] R. Freeman, “Shaped radiofrequency pulses in high resolution nmr,” *Progress in Nuclear Magnetic Resonance Spectroscopy*, vol. 32, no. 1, pp. 59 – 106, 1998.
- [106] E. M. Fortunato, M. A. Pravia, N. Boulant, G. Teklemariam, T. F. Havel, and D. G. Cory, “Design of strongly modulating pulses to implement precise effective hamiltonians for quantum information processing,” *The Journal of Chemical Physics*, vol. 116, no. 17, pp. 7599–7606, 2002.
- [107] M. A. Nielsen and I. L. Chuang, *Quantum Computation and Quantum Information*. Cambridge, England: Cambridge University Press, 2000.
- [108] K. Blum, *Density Matrix Theory and Application*. Springer, 1996.
- [109] R. A. Horn and C. R. Johnson, *Topics in Matrix Analysis*. Cambridge University Press, 1991.
- [110] T. F. Havel, “Robust procedures for converting among lindblad, kraus and matrix representations of quantum dynamical semigroups,” *Journal of Mathematical Physics*, vol. 44, pp. 534–557, 2003.
- [111] G. Lindblad, “On the generators of quantum dynamical semigroups,” *Communications in Mathematical Physics*, vol. 48, pp. 119–130, 1976.
- [112] J. Chamilliard, “On an electron spin resonance spectrometer for quantum information processing,” Master’s thesis, University of Waterloo, 2011.

- [113] Y. Zhang, “Universal control in 1e-2n spin system utilizing anisotropic hyperfine interactions,” Master’s thesis, University of Waterloo, 2010.
- [114] W. Froncisz, T. Oles, and J. S. Hyde, “Q-band loop-gap resonator,” *Review of Scientific Instruments*, vol. 57, no. 6, pp. 1095–1099, 1986.
- [115] G. Rinard and G. Eaton, “Loop-gap resonators,” in *Biomedical EPR, Part B: Methodology, Instrumentation, and Dynamics* (S. Eaton, G. Eaton, and L. Berliner, eds.), vol. 24/B of *Biological Magnetic Resonance*, pp. 19–52, Springer US, 2005.
- [116] E. Knill, “Quantum computing with realistically noisy devices,” *Nature*, vol. 434, no. 7029, pp. 39–44, 2005.
- [117] A. G. Fowler, M. Mariantoni, J. M. Martinis, and A. N. Cleland, “Surface codes: Towards practical large-scale quantum computation,” *Phys. Rev. A*, vol. 86, p. 032324, Sep 2012.
- [118] I. L. Chuang and M. A. Nielsen, “Prescription for experimental determination of the dynamics of a quantum black box,” *Journal of Modern Optics*, vol. 44, no. 11-12, pp. 2455–2467, 1997.
- [119] J. Emerson, R. Alicki, and K. Życzkowski, “Scalable noise estimation with random unitary operators,” *Journal of Optics B: Quantum and Semiclassical Optics*, vol. 7, no. 10, p. S347, 2005.
- [120] E. Magesan, J. M. Gambetta, and J. Emerson, “Scalable and robust randomized benchmarking of quantum processes,” *Phys. Rev. Lett.*, vol. 106, p. 180504, May 2011.
- [121] M. J. Biercuk, H. Uys, A. P. Vandevender, N. Shiga, W. M. Itano, and J. J. Bollinger, “High-fidelity quantum control using ion crystals in a penning trap,” *Quantum Info. Comput.*, vol. 9, no. 11, pp. 920–949, 2009.
- [122] K. R. Brown, A. C. Wilson, Y. Colombe, C. Ospelkaus, A. M. Meier, E. Knill, D. Leibfried, and D. J. Wineland, “Single-qubit-gate error below  $10^{-4}$  in a trapped ion,” *Phys. Rev. A*, vol. 84, p. 030303, 2011.
- [123] C. A. Ryan, M. Laforest, and R. Laflamme, “Randomized benchmarking of single- and multi-qubit control in liquid-state nmr quantum information processing,” *New Journal of Physics*, vol. 11, no. 1, p. 013034, 2009.

- [124] J. M. Chow, J. M. Gambetta, L. Tornberg, J. Koch, L. S. Bishop, A. A. Houck, B. R. Johnson, L. Frunzio, S. M. Girvin, and R. J. Schoelkopf, “Randomized benchmarking and process tomography for gate errors in a solid-state qubit,” *Phys. Rev. Lett.*, vol. 102, p. 090502, 2009.
- [125] R. Barends, J. Kelly, A. Megrant, A. Veitia, D. Sank, E. Jeffrey, T. C. White, J. Mutus, A. G. Fowler, B. Campbell, Y. Chen, Z. Chen, B. Chiaro, A. Dunsworth, C. Neill, P. O’Malley, P. Roushan, A. Vainsencher, J. Wenner, A. N. Korotkov, A. N. Cleland, and J. M. Martinis, “Superconducting quantum circuits at the surface code threshold for fault tolerance,” *Nature*, vol. 508, no. 7497, pp. 500–503, 2014.
- [126] S. Olmschenk, R. R Chicireanu, K. D. Nelson, and J. Porto, “Randomized benchmarking of atomic qubits in an optical lattice,” *New Journal of Physics*, vol. 12, no. 11, p. 113007, 2010.
- [127] J. T. Muhonen, A. Laucht, S. Simmons, J. P. Dehollain, R. Kalra, F. E. Hudson, S. Freer, K. M. Itoh, D. N. Jamieson, J. C. McCallum, A. S. Dzurak, and A. Morello, “Quantifying the quantum gate fidelity of single-atom spin qubits in silicon by randomized benchmarking,” *Journal of Physics: Condensed Matter*, vol. 27, no. 15, p. 154205, 2015.
- [128] S. Bravyi and A. Kitaev, “Universal quantum computation with ideal clifford gates and noisy ancillas,” *Phys. Rev. A*, vol. 71, p. 022316, Feb 2005.
- [129] C. C. López, B. Lévi, and D. G. Cory, “Error characterization in quantum information processing: A protocol for analyzing spatial correlations and its experimental implementation,” *Phys. Rev. A*, vol. 79, p. 042328, 2009.
- [130] S. Eaton and G. Eaton, “Irradiated fused-quartz standard sample for time-domain epr,” *Journal of Magnetic Resonance, Series A*, vol. 102, no. 3, pp. 354 – 356, 1993.
- [131] M. H. Levitt, *Composite Pulses*. John Wiley & Sons, Ltd, 2007.
- [132] R. Tycko, “Broadband population inversion,” *Phys. Rev. Lett.*, vol. 51, pp. 775–777, Aug 1983.
- [133] M. A. Pravia, N. Boulant, J. Emerson, A. Farid, E. M. Fortunato, T. F. Havel, R. Martinez, and D. G. Cory, “Robust control of quantum information,” *The Journal of Chemical Physics*, vol. 119, no. 19, pp. 9993–10001, 2003.

- [134] N. Boulant, J. Emerson, T. F. Havel, D. G. Cory, and S. Furuta, “Incoherent noise and quantum information processing,” *The Journal of Chemical Physics*, vol. 121, no. 7, pp. 2955–2961, 2004.
- [135] J. J. L. Morton, A. M. Tyryshkin, A. Ardavan, K. Porfyraakis, S. A. Lyon, and G. Andrew D. Briggs, “Electron spin relaxation of N@C60 in CS<sub>2</sub>,” *The Journal of Chemical Physics*, vol. 124, no. 1, 2006.
- [136] O. W. Sørensen, “A universal bound on spin dynamics,” *Journal of Magnetic Resonance (1969)*, vol. 86, no. 2, pp. 435–440, 1990.
- [137] O. W. Sørensen, “The entropy bound as a limiting case of the universal bound on spin dynamics. polarization transfer in  $i_n s_m$  spin systems,” *Journal of Magnetic Resonance (1969)*, vol. 93, no. 3, pp. 648–652, 1991.
- [138] L. J. Schulman and U. V. Vazirani, “Molecular scale heat engines and scalable quantum computation,” in *Proceedings of the Thirty-first Annual ACM Symposium on Theory of Computing*, STOC ’99, (New York, NY, USA), pp. 322–329, ACM, 1999.
- [139] Y. Elias, J. M. Fernandez, T. Mor, and Y. Weinstein, “Optimal algorithmic cooling of spins,” *Israel Journal of Chemistry*, vol. 46, no. 4, pp. 371–391, 2006.
- [140] N. A. Rodriguez-Briones and R. Laflamme, “Achievable polarization for heat-bath algorithmic cooling,” *arXiv:1412.6637v1 [quant-ph]*, 2014.
- [141] D. K. Park, N. A. Rodriguez-Briones, G. Feng, R. R. Darabad, J. Baugh, and R. Laflamme, “Heat bath algorithmic cooling with spins: review and prospects,” *arXiv:1501.00952v1 [quant-ph]*, 2015.
- [142] T. Cole, C. Heller, and H. McConnell, “Electron magnetic resonance of CH(COOH)<sub>2</sub>,” *Proceedings of the National Academy of Sciences of the United States of America*, vol. 45, no. 4, p. 525, 1959.
- [143] T. Cole and C. Heller, “Hyperfine splittings in the (HOOC) C<sup>13</sup>H (COOH) radical,” *Journal of Chemical Physics*, vol. 34, pp. 1085–1086, 1961.
- [144] A. Horsfield, J. Morton, and D. Whiffen, “Electron spin resonance of  $\gamma$ -irradiated malonic acid,” *Molecular Physics*, vol. 4, no. 4, pp. 327–332, 1961.
- [145] J. A. Goedkoop and C. H. MacGillavry, “The crystal structure of malonic acid,” *Acta Crystallographica*, vol. 10, pp. 125–127, Feb 1957.

- [146] N. Jagannathan, S. Rajan, and E. Subramanian, "Refinement of the crystal structure of malonic acid,  $C_3H_4O_4$ ," *Journal of chemical crystallography*, vol. 24, no. 1, pp. 75–78, 1994.
- [147] J. Krzystek, A. B. Kwiram, and A. L. Kwiram, "Ednmr and endor study of the beta.-. gamma. phase transition in malonic acid crystals," *The Journal of Physical Chemistry*, vol. 99, no. 1, pp. 402–409, 1995.
- [148] M. Fukai, T. Matsuo, and H. Suga, "Thermodynamic properties of phase transitions in malonic acid and its deuterated analogue," *Thermochimica acta*, vol. 183, pp. 215–243, 1991.
- [149] R. McCalley and A. L. Kwiram, "Endor studies at 4.2 k of the radicals in malonic acid single crystals," *The Journal of Physical Chemistry*, vol. 97, no. 12, pp. 2888–2903, 1993.
- [150] H. McConnell, C. Heller, T. Cole, and R. Fessenden, "Radiation damage in organic crystals. I. CH (COOH)<sub>2</sub> in Malonic Acid," *Journal of the American Chemical Society*, vol. 82, no. 4, pp. 766–775, 1960.
- [151] J. Morton, "Electron spin resonance spectra of oriented radicals," *Chemical Reviews*, vol. 64, no. 4, pp. 453–471, 1964.
- [152] E. Sagstuen, A. Lund, Y. Itagaki, and J. Maruani, "Weakly coupled proton interactions in the malonic acid radical: Single crystal endor analysis and epr simulation at microwave saturation," *The Journal of Physical Chemistry A*, vol. 104, no. 27, pp. 6362–6371, 2000.
- [153] J. Kang, S. Tokdemir, J. Shao, and W. H. Nelson, "Electronic g-factor measurement from ENDOR-induced EPR patterns: malonic acid and guanine hydrochloride dihydrate," *Journal of Magnetic Resonance*, vol. 165, no. 1, pp. 128–136, 2003.
- [154] M. Frisch, G. Trucks, H. Schlegel, G. Scuseria, M. Robb, J. Cheeseman, G. Scalmani, V. Barone, B. Mennucci, G. Petersson, H. Nakatsuji, M. Caricato, X. Li, H. Hratchian, A. Izmaylov, J. Bloino, G. Zheng, J. Sonnenberg, M. Hada, M. Ehara, K. Toyota, R. Fukuda, J. Hasegawa, M. Ishida, T. Nakajima, Y. Honda, O. Kitao, H. Nakai, T. Vreven, J. J. A. Montgomery, J. Peralta, F. Ogliaro, M. Bearpark, J. Heyd, E. Brothers, K. Kudin, V. Staroverov, R. Kobayashi, J. Normand, K. Raghavachari, A. Rendell, J. Burant, S. Iyengar, J. Tomasi, M. Cossi, N. Rega, J. Millam, M. Klene, J. Knox, J. Cross, V. Bakken, C. Adamo, J. Jaramillo, R. Gomperts, R. Stratmann, O. Yazyev, A. Austin, R. Cammi, C. Pomelli, J. Ochterski,

- R. Martin, K. Morokuma, V. Zakrzewski, G. Voth, P. Salvador, J. Dannenberg, S. Dapprich, A. Daniels, O. Farkas, J. Foresman, J. Ortiz, J. Cioslowski, , and D. Fox, “Gaussian 09, revision a.02,” 2009. Gaussian, Inc., Wallingford CT.
- [155] T. Borneman, *Techniques for Noise Suppression and Robust Control in Spin-Based Quantum Information Processors*. PhD thesis, Massachusetts Institute of Technology, 2012.
- [156] K. Tateishi, M. Negoro, A. Kagawa, and M. Kitagawa, “Dynamic nuclear polarization with photoexcited triplet electrons in a glassy matrix,” *Angewandte Chemie International Edition*, vol. 52, no. 50, pp. 13307–13310, 2013.
- [157] K. Tateishi, M. Negoro, S. Nishida, A. Kagawa, Y. Morita, and M. Kitagawa, “Room temperature hyperpolarization of nuclear spins in bulk,” *Proceedings of the National Academy of Sciences*, vol. 111, no. 21, pp. 7527–7530, 2014.